NASA Contractor Report 4178

An Unsteady Helicopter Rotor-Fuselage Interaction Analysis

Peter F. Lorber and T. Alan Egolf

CONTRACT NAS1-17469
SEPTEMBER 1988

NASA

ERRATA

NASA Contractor Report 4178

An Unsteady Helicopter Rotor
Fuselage Interaction Analysis

Peter F. Lorber and T. Alan Egolf
September 1988

The report title is incorrect. The correct title should read: An Unsteady Helicopter Rotor-Fuselage Interaction Analysis. Please replace the cover, title page, and Report Documentation Page with the attached corrected pages.

Issue Date: October 1988

NASA Contractor Report 4178

An Unsteady Helicopter Rotor-Fuselage Interaction Analysis

Peter F. Lorber and T. Alan Egolf
United Technologies Research Center
East Hartford, Connecticut

Prepared for
NASA Langley Research Center and
Army Aerostructures Directorate, USAARTA-AVSCOM
under Contract NAS1-17469

National Aeronautics
and Space Administration

**Scientific and Technical
Information Division**

1988

PREFACE

This work was supported by the Rotorcraft Aerodynamics Office of the Army Aerostructures Directorate, USAARTA-AVSCOM, and administered by the National Aeronautics and Space Administration at Langley Research Center under Contract NAS1-17469. The Army technical representative for this contract was John C. Wilson. The UTRC program manager was Anton J. Landgrebe. The extension of this analysis to include the unsteady term in the evaluation of the fuselage pressures was supported by United Technologies Research Center Corporate IR&D Funding.

SUMMARY

A computational method has been developed to treat the unsteady aerodynamic interaction between a helicopter rotor, wake, and fuselage and the interaction between the main and tail rotors. An existing lifting line-prescribed wake rotor analysis and a source panel fuselage analysis were modified to allow prediction of unsteady fuselage surface pressures and airloads. The analyses are coupled through the flow velocities induced by the rotor and wake on the fuselage and the velocities induced by the fuselage on the rotor. A prescribed displacement technique is used to position the rotor wake about the fuselage. Either a rigid blade or an aeroelastic blade analysis may be used to establish rotor operating conditions. Sensitivity studies were performed to determine the influence of the wake and fuselage geometry on the computational results. Solutions were computed for an ellipsoidal fuselage and a four-bladed rotor at several advance ratios. Results are presented that describe the induced velocities, pressures, and airloads on the fuselage and on the rotor. The ability to treat arbitrary geometries is demonstrated using a simulated helicopter fuselage. Initial computations were made to simulate an experimental rotor/fuselage interaction study performed at the Georgia Institute of Technology. The computational results are compared with fuselage surface pressure measurements at several locations. Experimental data were not available to validate the primary product of the analysis: the vibratory airloads on the entire fuselage. A main rotor-tail rotor interaction analysis is also described, together with preliminary hover and forward flight results.

TABLE OF CONTENTS

LIST OF SYMBOLS

C_D	drag coefficient, D/T
C_ℓ	rolling moment coefficient, ℓ/RT
C_L	lift coefficient, L/T
C_m	pitching moment coefficient, m/RT
C_n	yawing moment coefficient, n/RT
C_p	pressure coefficient, $(P-P_\infty)/q_\infty$
ΔC_p	total pressure rise caused by rotor, $\Delta P/q_\infty$
C_T	rotor thrust coefficient, $T/(\rho\pi R^2(\Omega R)^2)$
GC	geometric influence coefficient
h	height of vortex above surface (m)
P	pressure (Nt/m^2)
P_∞	freestream static pressure (Nt/m^2)
q_∞	freestream dynamic pressure, $1/2\ \rho U_\infty^2$, (Nt/m^2)
r	radial distance from rotor hub (m)
R	rotor radius (m)
t	time (sec)
T	rotor thrust (Nt)
u	velocity (m/sec)
U_∞	freestreeam or flight velocity (m/sec)
v	velocity (m/sec)
v_i^{mom}	momentum-induced rotor downwash velocity (m/sec)
V_x	lateral velocity component (m/sec)
V_y	vertical velocity component (m/sec)
V_z	longitudinal velocity component (m/sec)
$V\Delta t/\Delta x$	nondimensional time step
x	lateral coordinate, Fig. 3 (m)
Δx	incremental lateral coordinate (m)
y	vertical coordinate, Fig. 3 (m)
z	longitudinal coordinate, Fig. 3 (m)

α	fuselage angle of attack (deg)
β	angle of yaw (deg)
γ	source strength
Γ	circulation strength of wake filament (m^2/sec)
μ	rotor advance ratio, $U_\infty/(\Omega R)$
ρ	air density (kg/m^3)
ϕ	velocity potential (m^2/sec)
ψ	blade azimuth, 0 deg. over tail, positive counter-clockwise when viewed from above (deg)
Ω	rotor rotation speed (radians/sec)

INTRODUCTION

Aerodynamic interactions between the components of a rotorcraft can have a significant effect on rotor and fuselage vibrations, on the aerodynamics of the rotor, and on aircraft performance. The extent to which the interaction between the individual sources of fluid disturbances can influence the vibration characteristics of rotorcraft was not fully appreciated until several recent designs placed the main rotor very close to the fuselage and tail surfaces. The available analytic methods were unable to predict the coupled unsteady aerodynamics, and in particular, they were unable to predict the time dependent rotor wake impingement on the fuselage. A comprehensive analysis that includes all of the pertinent physical phenomena is still impractical. A simplified treatment of unsteady rotor, wake, and fuselage interactions using singularity methods is described here. It is recognized that this approach may not correctly model the strong interactions between the rotor wake and the viscous flow field about the fuselage. However, this initial attempt to calculate the aerodynamics of the complete rotor, wake, and fuselage system should provide valuable insight and lead to more advanced methods.

Experimental studies have identified interactions between the helicopter main rotor, fuselage, tail rotor, and fixed wing, as discussed in references 1-9. The airflow induced by the main rotor blades and their wakes is a major source of unsteady excitation for the fuselage and tail assembly (refs. 1-6). In references 1-3 it is also shown that the fuselage distorts the wake and the airflow at the rotor. The unsteady excitation of the rotor may then be transmitted through the rotor hub to the fuselage. Large pressure oscillations on the fuselage at the fundamental blade passing frequency and its harmonics can be produced by the rotor and wake, as demonstrated by references 4 and 5. Flight tests have recognized such pressure pulses as a mechanism for generating fuselage vibrations.

Many computational tools have been developed to study various aspects of these problems (refs. 10-20). The current approach is an extension of SIMVIB (ref. 10). SIMVIB is a coupled rotor/airframe analysis developed by Sikorsky Aircraft and the United Technologies Research Center (UTRC) under contract to the Structures Laboratory, U.S. Army Research and Development Laboratory (AVRADCOM). It was developed to provide a design tool for predicting helicopter vibrations, and to provide a research tool to study the effects of structural properties, aerodynamic interactions, and vibration reduction devices on rotorcraft vibration levels. The SIMVIB analysis, as shown in figure 1, consists of a base program and several external programs to provide information to the base program. Two of the external aerodynamics programs are the subject of this work: the rotor inflow program, F389SR (refs. 11 and 12), and the fuselage potential flow program, WABAT (refs. 13 and 14). These programs have been refined, extended, and coupled in order to study unsteady rotor/fuselage interactions.

An initial, quasi-steady version of this analysis was described in reference 21. Additional studies of unsteady rotor-fuselage interactions are reported in references 22-25.

In addition to the rotor fuselage study, an initial main rotor-tail rotor interaction analysis was developed using the rotor inflow program (F389SR). Details of the assumptions and procedures of this analysis are presented in Appendix A. Preliminary hover and forward flight results are also provided.

TECHNICAL APPROACH

The rotor/fuselage analysis uses separate programs to compute the aerodynamics of the rotor and wake, the aerodynamics of the fuselage, and the dynamics of the rotor. These programs are run sequentially in a global iteration process to produce a converged solution that accounts for the influence of each component on all other components. The individual programs are WABAT (refs. 13 and 14) for the fuselage aerodynamics, F389SR (refs. 11 and 12) for the rotor and wake aerodynamics, and G400 (ref. 26) for the airloads and flexible blade dynamics of the rotor. A rigid blade dynamic analysis, GRP (the Generalized Rotor Performance Method, ref. 27), may be substituted for G400 if aeroelastic results are not required. The operation of the dynamics programs will not be discussed here since their function has not been altered for the rotor/fuselage analysis. Reference 28 provides a detailed description of the programs used in the rotor/fuselage analysis and of the programs that prepare the input and process the output.

Both aerodynamic programs (WABAT and F389SR) are based on the fundamental concept of superposition of individual singularity solutions to Laplace's equation for the velocity potential. These solutions are expressed as a velocity field (v) that is the summation of geometric influence coefficient terms (GC) multiplied by the strength of the singularities (γ).

$$v = \sum_{i=1}^{N} GC_i \, \gamma_i$$

For a lifting line representation of a wing (fixed or rotary), or for a filament representation of a wake, the singularity is a segment of a line vortex. The fuselage may be represented by panels of sources, sinks, doublets, or higher order singularities. A vortex panel singularity is generally used if the fuselage or fixed wing must generate lift. The strengths of the singularities are determined by imposing appropriate boundary conditions. In general, zero normal velocity is required at all wing and fuselage surfaces. Singularity methods often require a large number of elements (panels or vortex segments) to accurately model complex fuselage or wake geometries. Calculation of the geometric influence coefficients therefore becomes the major computational expense for such methods.

The Sikorsky Wing and Body Aerodynamic Technique (WABAT) computes a quasi-steady flow field about the fuselage. A source panel method is used to obtain an inviscid steady solution without flow separation. A vortex

lattice may be added to account for the influence of fixed lifting wings. The aerodynamic effect of other components of the rotorcraft may be included by adding the appropriate induced velocities to the boundary conditions imposed at each source panel. The fuselage induced velocities computed by WABAT may be evaluated at the fuselage surface and at field points removed from the body.

The UTRC Prescribed Wake Rotor Inflow Analysis (F389SR) is the single rotor version of the UTRC Rotorcraft Wake Analysis. It calculates the rotor and wake induced flow field both at the rotor and at external field points. The rotor is represented by a lifting line, and the wake by a set of trailing vortex filaments with prescribed geometry. Several wake models are available: the classical undistorted wake, the UTRC 'Generalized Distorted Wake Model for Forward Flight' (refs. 18 and 19), and an arbitrary input wake geometry which can be based on external programs such as the UTRC 'Wake Geometry Analysis' (ref. 20).

The rotor aerodynamic solution is quasi-steady, since while the rotor position, the wake geometry, and the strength of each segment of the bound and wake vortex filaments change at each time step (at each rotor azimuthal position), unsteady aerodynamic effects (such as pitch rate and acceleration dependence) are not included in the table look-up of the rotor lift distributions (which are used to calculate the strength of the bound vortices that represent the blades). The wake model does not include the shed wake segments (parallel to the blade trailing edge) that result from the time-dependent changes in the bound circulation at any individual segment of the blade lifting lines. For typical helicopter rotation frequencies and cyclic pitch variations, the effect of these shed wake segments is assumed to be small in comparison with the effect of the wake filaments that result from the spanwise circulation (airload) gradients. Finally, use of Laplace's equation to compute an unsteady potential flow is exact only if the flow is incompressible.

Solution Procedure

The rotor/fuselage analysis may be performed either using a prescribed rigid blade motion or with the blade response determined by an external aeroelastic (G400) or rigid blade (GRP) analysis. For clarity, the prescribed motion analysis will be described first. Figure 2 shows the global iteration procedure. This procedure will be illustrated using an ellipsoidal fuselage and a four-bladed rotor. Figure 3 illustrates this configuration. Two right-handed coordinate systems are identified. The fuselage system, used by the WABAT program, has an arbitrary origin and has the z coordinate pointing downstream parallel to the fuselage axis. The rotor coordinate system, used by the F389SR program, has its origin at the center of the hub, and has the x-y plane parallel to the rotor tip path plane and the z coordinate pointing away from the rotorcraft. The x axis points downstream in the rotor system, and zero azimuth lies along the positive x axis. The fuselage coordinate system is used for presenting the results in this report.

A steady-state solution for an isolated fuselage in uniform flow is obtained first using WABAT. The geometric influence coefficients describing the influence of each fuselage source panel on every other source panel are computed and stored for later use. The fuselage is oriented at the specified pitch and yaw angles with respect to the freestream. Boundary conditions of no flow normal to each panel are imposed. The resulting matrix is solved to determine the source strengths at each panel. The velocities are evaluated at each fuselage panel, as shown by the 'tuft' arrows in figure 4. The fuselage induced velocity is also evaluated at the rotor disc inflow points used by program F389SR. The tip-path-plane position is defined by the specified rotor shaft angle, blade coning angle, and first harmonic flapping amplitudes. Figure 5 shows a contour plot of the axial velocity (the component perpendicular to the tip-path-plane) induced at the rotor disc by the isolated fuselage, and figure 6 shows the azimuthal variation of all three velocity components (axial, tangential, and radial) at one location, $r/R = 0.75$. The velocities are laterally symmetric, and the effects are concentrated over the fuselage nose and tail. A Fourier sine and cosine series in blade azimuth is computed for each velocity component at each radial station. The Fourier series is written to a disc file for transfer to F389SR. The coordinates of each fuselage panel in the rotor tip-path-plane system are also computed and stored.

The next step is to obtain a rotor blade and wake solution using F389SR. An initial wake geometry (classical, generalized, or based on input from an external source) is generated. A vortex filament trails from each boundary between the lifting line segments that represent the rotor blades, as shown in figure 7. For a typical set of nine line segments per blade, there will be ten wake filaments per blade. Several outboard filaments may be combined to represent a rolled-up tip vortex. The filaments extend over a specified number of revolutions, typically four to eight. The undisplaced classical wake geometry at one time step for the example problem at $\mu = 0.10$ is shown in figure 8. The wake from one blade is shown; wakes from all four blades are included in the actual solution. For a coupled rotor/fuselage solution, the wake must be displaced so that it does not pass through any solid bodies. The wake displacement procedure will be described in detail below; an example of the displacement of a single tip wake filament is shown in figure 9. Figure 10 shows the displacement of all of the filaments that emanate from one blade. This is the wake geometry that will be used at this time step for the remainder of the F389SR analysis. Each segment of the wake is assumed to have a circulation equal to the difference in the bound circulation of the two blade lifting line segments that are adjacent to the point of origin of the wake segment, evaluated at the time of origin of the wake segment. The effect of the wake can therefore be included in the geometric influence coefficients of the rotor. The rotor-on-rotor influence coefficients are now computed and stored at all time steps, based upon the displaced wake geometry. A matrix is then solved to determine the blade bound circulation strength at each segment

of the blade at each azimuthal position. The velocity at each blade segment accounts for the velocities induced by the motion of the blade, by all of the rotor and wake vortex segments, and by the fuselage. A contour plot of the bound circulation is shown in figure 11. This may be compared to figure 12, which presents equivalent results when the influence of the fuselage is not included. Significant changes in the circulation contours are present, especially over the fuselage nose and tail.

Program F389SR is now rerun to compute the rotor and wake induced velocities at the fuselage. The second F389SR run to determine the 'field' solution is frequently performed at a finer azimuthal increment than the initial F389SR run that determined the 'circulation' solution. An azimuthal increment of 15 deg is usually sufficient for the circulation solution, while increments of 1.75 to 7.5 deg may be required to obtain the necessary time resolution in the velocities at the fuselage. The wake geometry (as displaced about the fuselage) is computed at the required azimuthal stations, and geometric influence coefficients for the influence of each segment of the blade lifting line (and its associated wake filament segments) on each fuselage panel are generated and stored. The values of the blade bound circulations computed during the first F389SR run are now read back and interpolated to the values of azimuth used in the field solution. The three components of the rotor and wake induced velocity at each panel are evaluated. Figure 13a shows the time history of the induced velocity at fuselage panel 44 for the example problem. (Panel 44 is located on the upper surface below the rotor, as indicated by the cross-hatched area on figure 3.) The velocities are normalized by the freestream velocity and are displayed in the fuselage coordinate system (fig. 3). The strong one-per-blade passage (four-per-revolution) effect dominates the induced velocities. A Fourier sine and cosine series is determined for each velocity component at each fuselage panel, and is stored for transfer to the WABAT program.

Next, WABAT generates a time-dependent fuselage solution that accounts for the rotor and wake induced velocities. The fundamental period of the rotor-wake-fuselage system is the rotor blade passing period. This period is divided into time intervals that correspond to the blade azimuth increments used for the field solution of F389SR. A separate WABAT solution for the velocities is determined at each time step, and combined to create the overall unsteady solution. The velocity induced by the rotor and wake is added to the appropriate component of the freestream (flight) velocity and the source strengths are determined so that the zero normal velocity condition is satisfied at each panel. The previously computed geometric influence coefficients are used in the matrix solution.

The rotor induced velocities at panel 44 are shown in figure 13a. The largest induced velocities are in the vertical (y) and longitudinal (z) directions. The total velocity (including freestream and source panel contributions) is shown in figure 13b. Since panel 44 is nearly horizontal, the

source velocity has nearly cancelled out the vertical induced velocity (V_y) component to satisfy the boundary condition. The lateral induced velocity (V_x) is changed only slightly by the freestream velocity and the source velocity. The addition of the freestream velocity (and the contribution from the other source panels) has increased the streamwise velocity component (V_z) so that it oscillates between about +0.1 and +0.9.

Since the fluid velocities away from the rotor are much smaller than the speed of sound, incompressible flow provides a good approximation to the conditions at the fuselage. In incompressible potential flow, the unsteady velocities are exact solutions of Laplace's equation for the velocity potential at each instant in time. Therefore the quasi-steady and unsteady velocities are identical. (The flow about the rotor is compressible; in the rotor analysis compressibility effects are approximated by using Mach number dependent airfoil lift curves to determine the local instantaneous strength of the lifting line at each azimuthal and radial position.)

The pressures at the fuselage must be obtained from the velocities using an explicitly unsteady computation. Since all streamlines originate in the steady, constant velocity freestream, the momentum equation for unsteady, incompressible, inviscid flow is reduced to the unsteady Bernoulli equation:

$$\frac{\partial \phi}{\partial t} + \frac{|\vec{V}|^2}{2} + \frac{P}{\rho} = \text{constant}$$

The unsteady potential term ($\partial\phi/\partial t$) represents the required acceleration of the fluid elements. The pressure coefficient is therefore:

$$C_p = 1 - \frac{|\vec{V}|^2}{U_\infty^2} - \frac{2}{U_\infty^2}\frac{\partial \phi}{\partial t}$$

An earlier version of this analysis (Ref. 21) did not include the unsteady term, but added an approximate total pressure correction to account for the energy added to the fluid by the rotor. Based upon actuator disc theory, a steady increment of $\Delta C_p = 2C_T/\mu^2$ was added to the pressures at those fuselage panels that were within the wake of the rotor. As discussed in Refs. 29 and 30, an unsteady representation is necessary and sufficient to completely describe both the pressure field within a fluid machine (compressor, turbine, or helicopter rotor) and the change in stagnation enthalpy produced by the machine. Therefore no total pressure correction is now required. It is in fact demonstrated in Ref. 30 that, for a moving or rotating row of bound vortices, the time averaged total pressure changes computed using the unsteady Bernoulli equation are identical to the results of actuator disc theory. The work done on the fluid by the rotor is contained in vortical wake and in the fluid velocities induced by the moving wake and blades.

The most significant contributions to the $\partial\phi/\partial t$ term are made by the forced motion of the bound vortex segments that represent the rotor blades, and the convection of the vortex filaments that represent the wake. Reference 24 illustrates the strong effect that the moving bound vortex can have on the pressures measured during an experimental rotor-fuselage interaction study. The velocity potential at any 'field' point $\vec{x}$, induced by a moving vortex filament (or other 'source' element) of strength γ, located at position $\vec{x}'$ is given by

$$\phi(\vec{x}, \vec{x}', t) = \gamma(t) * f\left(\vec{x} - \vec{x}'(t)\right).$$

Differentiating,

$$\begin{aligned} \partial\phi/\partial t &= -\gamma\,(\partial f/\partial\vec{x}' * \partial\vec{x}'/\partial t) + (\partial\gamma/\partial t)\, f \\ &= -\partial\phi/\partial\vec{x} * \partial\vec{x}'/\partial t + (1/\gamma)(\partial\gamma/\partial t)\,\phi \\ &= -\vec{V}_{induced}(\vec{x}) * \vec{V}_{source}(\vec{x}') + \phi\,\partial(\ln\gamma)/\partial t \end{aligned}$$

The second term on the right-hand-side is zero for a constant-strength source, and is generally small in the current application (see Appendix B).

An exact analytic computation of the $\partial\phi/\partial t$ term for a two dimensional vortex moving above a flat plate either parallel to the freestream or perpendicular (out-of-plane) to the freestream is given in Appendix B. The perpendicular motion models the interaction between the fuselage and the bound vorticity of the rotor blades and the parallel motion models the convection of the wake past the fuselage. For geometries and velocities that are representative of a helicopter application, it is shown in Appendix B that, during a close passage of the rotor blade above the fuselage, the contribution of the $\partial\phi/\partial t$ term to the unsteady pressure coefficient may be an order of magnitude greater than the contribution of the $|\vec{V}|^2$ term. In addition, for a two-dimensional vortex that is convected by the freestream parallel to the flat plate, the $\partial\phi/\partial t$ and $|\vec{V}|^2$ terms tend to cancel out. This simple model problem clearly illustrates the necessity for including unsteady effects in the pressure computation.

In the present analysis, the contribution to $\partial\phi/\partial t$ from the bound vorticity is evaluated by forming the vector dot product of the relative velocity of each radial vortex segment with the velocity induced at each fuselage panel by that segment. The relative velocity is a result of the blade rotation, and includes the effects of tip-path-plane lateral and longitudinal tilt. The contribution to $\partial\phi/\partial t$ from the change in strength of each bound vortex segment with time (azimuth) is typically quite small (see Appendix B) and is neglected, in order to improve computational efficiency.

The contribution to $\partial\phi/\partial t$ from the rotor wake is approximated by assuming that all portions of the wake are convected at a constant speed equal to the vector sum of the freestream velocity and the downwash velocity of the wake (V_i^{mom}), as computed in the rotor inflow program (F389SR). For an undistorted classical wake, this computation would be exact, but for a generalized or free wake it is only approximate. This approach does however significantly reduce computational costs. At each fuselage panel, $\partial\phi/\partial t$ is evaluated by taking the dot product of the velocity induced by the wake with the wake convection velocity.

The contribution to $\partial\phi/\partial t$ from the time rate of change of the strength of the fuselage source panels is assumed to be small and is neglected in this analysis. Appendix B contains a sample computation of the unsteady pressures induced by a point source of varying strength.

More significant omissions from the analysis are an accurate model of the strong interaction between the vortex filaments and the fuselage, any treatment of the wake mixing that occurs away from the rotor, and any treatment of fuselage separation effects or of the wake of the fuselage. These effects are beyond the scope of this discrete singularity/potential flow model.

The computed pressure coefficient at panel 44 is shown in figure 14a. The pressure force on the panel is determined by multiplying the pressure coefficient by the panel area and finding the force components in each direction. Figure 14b shows the force components on panel 44. The components are nondimensionalized by dividing by the freestream dynamic pressure and fuselage reference area. Because the pressure force is perpendicular to the panel, the vertical force component (Fy) has the largest magnitude on this panel. Note that these results do not account for viscous drag or flow separation. The pressure force components at each panel are integrated to determine the overall fuselage airloads and moments.

The fuselage induced velocities at the rotor disc are recomputed using the revised source panel strengths and stored for use during the next iteration of the F389SR program. This iteration is very similar to the inital F389SR run, with the exception that the stored geometric influence coefficients are reused. The use of the stored rotor-on-body influence coefficients assumes that any changes in the relative position of the rotor and fuselage are small enough to be neglected. (The relative position will change only if a blade response program is used - see page 14.) The storage of the influence coeffcients significantly reduces the computational time required for the later F389SR runs. A reduction of 95% is typical. The disadvantage of this technique is that large temporary storage files are required for the influence coefficients. Between 10 and 40 MBytes of storage is typical. The advantage of storing the WABAT influence coefficients is also significant, especially since these coefficients must be reused at each time step and at each step of the global iteration.

Convergence of the global iteration procecedure is determined from the rotor and wake induced velocities at the fuselage. The maximum change in the mean velocity at any panel and in the Fourier amplitude of any harmonic at any panel are determined after each field solution of F389SR. If the maximum change is less than 0.0005 times the freestream velocity, the solution is deemed to be converged. Otherwise the global WABAT/F389SR iteration is repeated. Between two and six global iterations are typical. The final run of the WABAT program after the rotor induced velocities converge determines the final velocities and pressures on the fuselage and creates a series of plotting files that may be used to display the results of the analysis.

Prescribed Wake Displacement

The displacement of the rotor wake around the fuselage should approximate reality. A sophisticated singularity method would use a free wake influenced both by the remainder of the wake and by the fuselage. This type of calculation would be computationally intensive and very costly to run on most computers. The alternative is to prescribe the displacement of the wake. The work reported in reference 15 used displaced wake models as a first level approach to predict the time-averaged upper surface pressure distributions. However, the simplified wake model used lacked many of the physical features present in the geometry of an unsteady wake. In particular, the wake circulation distribution was based upon approximate time-averaged rotor airloads and circulations, and did not include discrete inboard vortex sheets and tip vortices. The displaced wake used in the current analysis retains the time-dependent circulations and discrete geometries of the original F389SR techinque (ref. 11), but is displaced around the fuselage by means of a set of simple analytic rules.

All filaments that the initial prescribed wake model (either classical, generalized, or external) would have placed inside of or adjacent to the fuselage are moved away from the fuselage. The displacement takes place in a plane normal to the flight velocity, and forces the filaments out to a specified distance above the fuselage surface, as shown in figure 9. The repositioned wake segments are usually subdivided into 10 smaller segments to increase the resolution near the fuselage and to avoid long straight segments that could intersect the fuselage. The displacement procedure assumes that the interaction with the fuselage does not accelerate or decelerate the downstream convection of the wake along the surface, and that the wake geometry above and below the fuselage is unaffected by the interaction with the fuselage. There are several parameters that may be specified to prescribe the

displacement. 1) The displacement distance may vary. 2) Each filament may be repositioned either above or below the fuselage. 3) The definition of the vortex core may be changed to control the strength of the interaction. Either a zero velocity core or a Rankine core (linear increase in velocity with distance) may be used. 4) The radius of the vortex core used to determine the velocities at the fuselage (in the 'field solution') may be different from the value used in determining the blade circulations. Increasing the vortex core size simulates diffusion of the wake and the effects of the viscous interaction near the fuselage surface.

The numerous options in the wake model are included because of the absence of data on what actually occurs during the interaction with the fuselage. The object was to establish analytic rules that produce wake geometries that 'look reasonable' and are not overly sensitive to small changes in the interaction parameters. The effect of changes in two of the parameters will be described in the discussion of the computational results: the distance that the wake is offset from the surface, and the location where the wake shifts from passing over the fuselage to passing underneath it. In the absence of wake interaction data from an experiment or from a sophisticated computation (one that includes free wake and viscous interaction effects), the wake displacement rules can best be described as an 'educated guess' about the actual physics involved.

The wake may be displaced about fuselages with arbitrary geometries. An interactive preprocessing program (ref. 28) is used to generate an ordered 'wake displacement body' from the input set of fuselage panels. The wake displacement body defines the fuselage using a series of cross section planes at 8 to 25 stations along the longitudinal axis. Fuselage radii are specified at equal angular increments (typically 10 to 20 deg) at each cross section. This ordered file allows an efficient search to be made to accurately determine whether each wake filament would pass inside or outside of the fuselage. The pre-processor needs to be run only when a new fuselage geometry is introduced.

Effect of Fuselage Panel and Wake Filament Spacing

Certain combinations of fuselage panel size and solution time step were found to create a numerical resonance. The problem was first noticed when solving for the airloads on an ellipsoidal fuselage that had a uniform downstream panel spacing. By varying the ratio of the panel size to the spacing between the wake vortices, the wake/fuselage system can be brought into a numerical resonance where each tip wake filament passes over the center of a panel simultaneously. Since the induced velocity at each panel is evaluated only at a control point located at the geometric centroid of the panel, the

panels are strongly excited when the vortex filaments are directly above the centroids and weakly excited when the vortex filaments are between panel centroids. This creates a very strong fictitious unsteady response. Figure 15 shows a top view of a resonant geometry where the tip vortex filaments shed by sucessive blades have a streamwise spacing exactly equal to three times the panel size. The calculated aerodynamic lift on the fuselage is dominated by a fictitious three-per-blade passage force, as shown in figure 16. This frequency is a direct result of each tip filament passing over three panels before the wake geometry repeats itself. The real unsteady airloads are expected to have a much stronger response at the blade passing frequency. (Note that the calculations in this section used quasi-steady aerodynamics to evaluate the fuselage pressures. This emphasizes the wake resonance effects because the strong moving bound vortex effects are neglected.)

A simplified model problem (fig. 17) was used to study the vortex/panel interaction. The model consists of a single two-dimensional vortex filament that passes a specified distance above a flat plate. The flat plate is divided into a set of discrete source panels of equal size. The time-dependent force on the flat plate can be determined using various values of the panel size, height of the vortex above the surface, and solution time step. One case is illustrated in figure 17a: the flat plate extends from $x = -2.0$ to $x = +2.0$, and is divided into 20 source panels of width $\Delta x = 0.2$. The vortex passes over the plate at a height of 0.2 units. The analytic solution for the time history of the (quasi-steady) force on the plate, obtained by integrating the force on each panel, is shown as the solid line in figure 17a. As the vortex approaches the leading edge of the plate, the magnitude of the force increases from zero to a maximum, and then maintains that maximum until the vortex passes over the trailing edge of the plate. Numerical solutions were also obtained. The dotted line represents the solution using the standard method of evaluating the induced velocity at the midpoint of each panel and assuming that this is the correct velocity for the entire panel. In figure 17a this solution lies on top of the analytic result. This will be true whenever the vortex is at least one panel space above the flat plate.

If the source panel size is increased to $\Delta x = 1.0$ a numerical resonance occurs, as shown by the 'midpoint' results in figure 17b. The panel size to vortex height ratio of 5.0 used here is typical of what occurs when a tip vortex drapes over the fuselage. As the vortex passes over the control point at the center of each panel, a strong force of more than twice the analytic value is observed. This fictitious force may be reduced by evaluating the vortex-induced velocity at three points spaced over each panel, and then trapezoidally integrating the results to obtain an average velocity at the panel. The dash-dotted line represents the solution obtained using this '3-point' technique. The force overshoot is significantly reduced, and the frequency of the oscillation is doubled, since the size of each panel has been effectively cut in half.

Additional solutions to the model problem were obtained using other values of the characteristic parameters. The ratio of vortex height to the streamwise panel size was found to be the most important parameter. In general, the effective streamwise panel size should be less than or equal to the vortex height in order to minimize the resonance. Changing the solution time step changes how well the numerical solution is resolved, but does not change the essential character of the resonance. A very coarse time step ($V\Delta t/\Delta x > 1$) will mask the resonance, but is likely to corrupt the lower frequency components of the solution, as shown in figure 17c.

Based upon the results of the model problem, a five point per panel induced velocity integration scheme was added to the rotor-fuselage analysis. The distance between each vortex segment in the wake and each panel is computed before the induced velocity at the panel is evaluated. If the distance is greater than a specified value, the vortex segment is said to be 'far' from the panel, and the induced velocity is evaluated only at the panel centroid. This approach is illustrated in figure 18a. If the distance is less than the specified value, the vortex segment is said to be 'near' to the panel, and the five point scheme is used: The velocity induced by the segment is evaluated at the panel midpoint and at four supplemental points. As shown in figure 18b, the supplemental points are located at the upstream and downstream ends of the panel and midway between the end points and the centroid. The supplemental points are chosen in the streamwise direction because the wake filaments close to the fuselage normally convect downstream along the fuselage panels. The average velocity at the panel is evaluated using a discrete integral of the velocity at the five points, effectively cutting the streamwise panel spacing by a factor of four. The full size panel is used for all further computations, such as determining the panel source strength and the surface pressure.

The panel-vortex distance that will activate the five point averaging must be larger than the streamwise panel spacing to ensure that all 'near' vortex/panel interactions are properly identified. For the fuselage and rotor geometries used in this report, a value of 15% of the rotor radius was used to separate 'near' and 'far' vortex/panel interactions. Since most of the 'near' interactions occur with the wake filaments that have been displaced just above the fuselage, the streamwise panel spacing should be no greater than five times the wake offset distance for five point averaging to successfully reduce the numerical resonances.

For the conditions used to date, between 1 and 2% of the total number of wake segment/fuselage panel interactions require the five-point averaging. For example, a case having 428 fuselage panels and an azimuthal increment of 3.75 deg required the computation of 158 million vortex segment/fuselage panel interactions, of which only 1.9 million required five point averaging. Therefore, even though the computational cost of a 'near' interaction is at least

five times that of a 'far' interaction, the incremental cost for the entire solution is less than 5% of the total cost. The benefit of including this technique is substantial, as shown in figure 19. Airloads computed using the midpoint technique (from fig. 16) are compared with those computed using the five point technique. Fourier analysis of the solutions indicates that the fictitious third harmonic has been reduced by a factor of five. Although reduced, the numerical resonance has not been completely eliminated, since it is a fundamental byproduct of the discretization of the wake and fuselage.

Coupling with a Blade Response Analysis

The rotor fuselage analysis may be coupled with a blade response program to provide the proper blade control angles and flapping response for the desired flight condition. The coupling also allows the blade response to include the effects of fuselage interference. The structure of the coupling is the same when using either the aeroelastic (G400) or rigid blade (GRP) program. As shown in figure 20, the blade response program exchanges information directly with the rotor inflow program, F389SR, and only indirectly with the fuselage program, WABAT. Rotor, wake, and fuselage induced inflow velocities are computed by F389SR and transferred to GRP or G400 as a harmonic series in azimuth at each radial station. The blade response program computes and transfers to F389SR the rotor geometry, wake transport velocity, shaft angle, collective, cyclic, twist, lag, coning, and flapping. If the aeroelastic analysis, G400, is used, the non-aerodynamic velocities induced by the motion of the blade are also computed and transferred to F389SR. Rigid blade motion velocities are computed independently (and consistently) by GRP and F389SR.

The sequence of program calls is shown in figure 21. The comparable sequence without a blade response analysis was shown in figure 2. The initial steady state isolated fuselage solution is obtained first. The fuselage induced velocities are computed at the estimated position of the rotor. The blade response program is run for an isolated rotor with uniform inflow. The appropriate files for restarting the program are saved, and the rotor position is transferred to F389SR. The blade circulations and the rotor, wake, and fuselage induced inflow velocities are computed by F389SR. The blade response is now recomputed to account for this variable inflow. A second inflow/blade response iteration is performed to partially converge this portion of the solution. A second steady state, isolated fuselage solution is obtained next, and the fuselage induced velocities are computed at the revised relative position of the rotor and fuselage. Program F389SR computes the geometric influence coefficients for the influence of the rotor and wake on the fuselage, making the assumption that any further changes in the relative

rotor/fuselage position will not be significant. At this point in the solution all of the geometric influence coefficients and other data needed to restart the individual programs have been computed and stored.

A sequence of program calls is now repeated until a globally converged solution is obtained (convergence again being determined using the rotor and wake induced velocities at the fuselage): An unsteady fuselage solution that includes rotor and wake influence is found first. Next, two iterations of the rotor inflow and blade response programs determine the rotor circulation and blade motion. Finally, the induced velocities at the fuselage are computed. Following convergence, a final call to the fuselage program determines the velocities and forces on the fuselage.

COMPUTATIONAL RESULTS

A selection of the numerical results of this analysis will be presented to demonstrate the typical characteristics of the solutions, to illustrate the effect of changing various parameters in the geometry, flight conditions, and numerical model, and to provide a comparison with some existing experimental data. The results are presented primarily to illustrate the operation of the analysis, and, except for the comparison with experimental data, are not intended to accurately represent any actual rotorcraft. More conditions must be simulated to determine whether the trends described here are independent of the numerical modelling or of the physical geometry.

Ellipsoidal Fuselage at Several Advance Ratios

Use of an ellipsoidal fuselage avoids geometric complexity and simplifies the interactions with the wake. The basic geometry of the fuselage and rotor was shown in figure 3. The four bladed main rotor has a radius of 7.6 m (25 ft), has an aspect ratio of 14.7, is unswept, and has a twist that decreases linearly by 6 deg over the radius. The airfoil data are based upon steady flow over a NACA 0012 section. The rotational tip speed is held fixed at 215 m/sec (700 ft/sec). The fuselage major (longitudinal) axis is 1.7 rotor radii, and the minor (lateral) axis is 0.379 radii. The rotor hub is located 0.216 radii above the fuselage major axis (.028 radii above the fuselage surface), and 0.758 radii aft of the fuselage nose. The rotor shaft was tilted 5 deg forward of the fuselage axis. The fuselage coordinate system has its origin at the nose of the ellipsoid.

A total of 428 panels are used to represent the complete fuselage. A downstream panel spacing of 0.0785 times the rotor radius is used, providing 22 longitudinal stations. There are 9 inflow control points located along the rotor radius, so that the wake is initially composed of 10 discrete vortex filaments. The four outboard filaments are assumed to roll up into a concentrated tip vortex after 15 deg of azimuth. For the circulation solution, the tip vortex is assumed to have a linear core with a radius equal to 0.006 rotor radii. A core radius of 0.012 rotor radii is used for the filaments that represent the inboard vortex sheet. Larger core radii are used for the computation of the wake induced velocities at the fuselage: 0.010 for the tip vortex, and 0.20 for the inboard filaments. The large inboard core radius simulates interaction with the diffuse inboard vortex sheet and avoids sharp filament-panel interaction effects. Wake filaments from six revolutions of the rotor are used in the computation. A classical wake model is used for clarity. An azimuthal increment of 15 deg was used for the blade circulation solution, while 7.5 deg was used for the induced velocity and fuselage pressure solution.

The standard parameters used to model the interaction of the wake and the fuselage include a displacement distance of the wake above the fuselage of 10% of the local body radius, a wake circulation that is unchanged by stretching about the fuselage, and a wake that shifts from being displaced above the fuselage to below the fuselage at an angle of -75 deg, as measured from the fuselage major axis. (See page 21 for a description of these wake parameters and of the effect of varying them.) The rigid blade response program was used to determine the blade control and flapping angles for trimmed flight. A rotor thrust of 80,000 Nt (18,000 lbs) was assumed, resulting in a thrust coefficient, C_T, approximately equal to 0.0078.

Results at $\mu = 0.10$.-The results at a rotor advance ratio of 0.10 (a flight speed of 21.3 m/sec or 41.5 kts) will presented first. At this advance ratio there is a significant interaction between the wake and the fuselage. Some intermediate results for this case have been shown earlier (figs. 5, 6, and 11-14). More detailed results for the final converged solution will now be described, both to illustrate the typical characteristics of the solution and to demonstrate the the ways in which the program output may be displayed.

Three global iterations were required to obtain a converged solution. Approximately 8 hours of CPU time were used on a Digital Equipment Corporation Micro-VAX II super-minicomputer. The most computationally expensive task was the calculation of the rotor on fuselage influence coefficients, which required 75% of the total time. Temporary storage of 30MB was needed for the influence coefficient files. The final control angles computed by the coupled variable inflow/rigid blade analysis were a collective pitch of 8.7 deg at the 75% of radius location, a first cosine harmonic cyclic pitch of -2.8 deg, and a first sine harmonic of 1.9 deg. The blade coning angle was 4.5 deg, and the fuselage angle of attack was 4.6 deg.

The final wake and fuselage geometry is shown in figure 22. The top view (fig. 22a) illustrates the position of the rotor and the tip vortices at a blade azimuth of 0 deg. At this advance ratio the tip filaments are convected past the fuselage in a regular pattern having a spacing equal to twice the fuselage panel size. The side view (fig. 22b) illustrates how the tip filaments are displaced upwards as they pass over the front of the fuselage, and then are shifted to pass below the fuselage as they reach the aft third of the fuselage. The surface velocity vectors are very short at those panels close to an upwards-displaced tip filament because the vortex-induced velocity nearly cancels out the flight velocity. The velocity vectors at the rear of the fuselage show an increase in velocity caused by the downward-displaced tip filaments. The rear view (fig. 22c) shows the displacement of the tip filaments and the downwash velocity induced by the rotor and wake.

The fuselage surface pressure coefficient is computed from the surface velocities and corrected to account for the unsteady motion of the rotor blades and wake vortices. Figure 23 shows the mean (time averaged) pressures along bodylines that run from the fuselage nose to the tail. Results are presented for bodylines along the fuselage top and bottom, and along the advancing and retreating blade sides. The solution for an isolated fuselage at $\alpha = 0$ is also shown. The isolated fuselage pressure coefficient is relatively constant at $C_p = -0.2$ over most of the fuselage, rising to $C_p = +1.0$ at the nose and tail stagnation points. The interaction with the rotor influences the fuselage pressures in several ways: 1) the tip-vortices reduce the surface velocities over the nose of the fuselage, increasing the surface pressure coefficient, and increase the surface velocities over the tail of the fuselage, decreasing the pressure coefficient (especially on the bottom of the fuselage), 2) the increased surface velocities induced by the entire wake decrease the overall pressure coefficient, while the unsteady $(\partial\phi/\partial t)$ effect from the moving wake increases the pressure coefficient (by $C_p \simeq +0.4$), and 3) the moving bound vortices of the blade locally increase the pressure coefficient along the top the fuselage, particularly below the regions of maximum blade loading (near $r/R \simeq 0.9$, or $z/R \simeq 0$, 1.6).

Figure 24 shows instantaneous pressures along the top of the fuselage at four values of azimuth, $\psi = 0$, 15, 30, and 60 deg. At $\psi = 0$ the rotor blades are directly over the surface, and the unsteady influence of the moving bound vortices greatly increases the local pressures, to $C_p = +2.3$ over the nose, and to $C_p = +1.5$ near $z/R = 1.4$. This effect is quite localized in time and space, therefore only a small pressure increase is observed at $\psi = 15$ deg. At the higher azimuthal positions the surface pressure distributions clearly show a periodic variation that correlates with the tip vortices that are convected directly over the forward fuselage (Fig. 22). The pattern moves down the fuselage as the rotor azimuth increases. This spatial oscillation differs from the temporal oscillation shown in figure 16, and is not a result of numerical resonance.

The fuselage airloads are determined by integration of the surface pressures. The lift, drag, and side force for this case are shown in figure 25a. The forces have a primary frequency of one/blade passage, but include significant higher harmonic content. The peak-to-peak airload amplitudes (as a percentage of the rotor thrust) are approximately 3.5% for lift, 2% for side force, and 0.6% for drag. For straight-and-level flight the rotor thrust approximates the vehicle weight. Thus the unsteady force on the fuselage divided by rotor thrust represents (in the absence of damping and inertia) the fuselage vibration levels (in g's) that are induced by aerodynamic forces. The minimum lift (maximum download) occurs at $\psi = 0$, 90, 180, and 270, corresponding to the passage of the blades over the fuselage. This implies that the moving bound vortices make a major contribution to the unsteady airloads. Figure 25b shows the aerodynamic moments on the fuselage (referenced to the rotor hub location). The moments are normalized by dividing by the rotor thrust and by the rotor radius. Again, the primary frequency is one/blade passage. Note that the computed forces and moments do

not include the tangential (viscous or skin-friction) forces on each panel, or the effect of rotor wake mixing and fuselage boundary layer separation, which may significantly change the surface pressures on the rear and bottom of the fuselage. Both of these effects will contribute to the mean download on the fuselage, which will not be adequately predicted by the current analysis.

The fuselage induced velocities at the rotor disc (in the tip-path-plane) in the final converged solution show significant quantitative differences from the velocities induced by the isolated fuselage. At the 75% of radius location, the final results (fig. 26) are qualitatively similar to the isolated fuselage results (fig. 6), but show an increased radial velocity and a decreased axial (inflow) velocity component. The contour plot of the converged solution (fig. 27) has a maximum positive (upflow) velocity of 3.8 m/sec (12.5 fps) near the nose of the fuselage, twice as large as the maximum of +2.0 m/sec (+6.5 fps) computed using an isolated fuselage (fig. 5). Other quantitative changes include reducing the maximum negative axial (downflow) velocity from -1.2 m/sec (-4.0 fps) for the isolated fuselage to -0.8 m/s (-2.5 fps) for the converged solution. The momentum inflow velocity for this case is -7.9 m/sec (-26 fps).

The blade element angle of attack is computed by adding the fuselage induced velocities to the velocities induced by the rotor and wake and by the blade motion, and dividing by the rotational velocity. There are relatively small changes between the angle of attack calculated in the converged solution (fig. 28a), calculated for the isolated rotor (fig. 28b), and calculated using the influence of a steady-state, isolated fuselage (fig. 28c). The largest change is an increase in the angle of attack on the retreating blade near the fuselage tail. The maximum angle of attack on the inboard section of the blade is 11.6 deg for the isolated rotor, 13.0 deg with steady fuselage effects, and 15.8 deg in the converged solution. Although the exact values are dependent on the wake model and other parameters, the trend toward higher angles of attack may change the predicted rotor stall and vibration characteristics.

The blade bound circulation (which is equivalent to the thrust distribution) also shows only a small change between the isolated rotor (fig. 12), steady fuselage influence (fig. 11), and converged (fig. 29) results. This may be partially the result of the rotor trim procedure adjusting the rotor control angles in each case to achieve the desired rotor thrust. It does indicate that the coupling back from the fuselage to the rotor is relatively weak, a fact that is reflected in the relatively rapid convergence of the global solution.

Results at Other Advance Ratios.-The rotor/fuselage analysis was also run at advance ratios of μ = 0.05, 0.15, 0.20, 0.25, 0.35, and 0.45 to examine the effect of variations in the flight speed. The same fuselage, rotor, type of

wake model, and thrust level were used in each case. The rigid blade response analysis (GRP) was used to determine the appropriate rotor control angles and pitch attitude for trimmed flight at each speed.

The interaction between the wake and the fuselage changes significantly with advance ratio. Increasing advance ratio reduces the vertical wake transport velocity, decreases the wake skew angle, and increases the longitudinal spacing between the wake filaments. These changes are apparent in the retreating side views of the rotor, fuselage, and tip vortex filaments shown in figure 30. At $\mu = 0.05$ (fig. 30a) the fuselage is completely enveloped in the wake. The tip vortices pass in front of the nose and behind the tail. The overall downwash is apparent from the fuselage surface velocity vectors. At $\mu = 0.10$ (fig. 22b) the tip filaments pass over the front of the fuselage. The fuselage velocities ahead of the wake are relatively undisturbed, while those over the rear of the fuselage show the irregularities caused by the tip vortices and the overall downwash. At $\mu = 0.15$ (fig. 30b), $\mu = 0.20$ (fig. 30c), and $\mu = 0.25$ (fig. 30d), the wake only intersects the top and rear of the fuselage. The weaker relative downwash causes the surface velocities to be more nearly aligned with the freestream velocity. Note that the fuselage angle of attack decreases steadily from +5.1 deg at $\mu = 0.05$ to +2.0 deg at $\mu = 0.25$ as the rotor tilts to develop the required propulsive force. Continued rotation of the vehicle brings the wake back into contact with the fuselage at the higher advance ratios of $\mu = 0.35$ (fig. 30e) and $\mu = 0.45$ (fig. 30f). At $\mu = 0.45$ the fuselage angle of attack is -7.4 deg, which, together with the increased wake interaction, causes an overall downwash on the surface.

The instantaneous surface pressures along the top of the fuselage are shown in figure 31 at advance ratios of $\mu = 0.05$, 0.15, 0.25, and 0.35. The equivalent results at $\mu = 0.10$ were shown in figure 24. Bodylines at $\psi = 0$, 15, 30, and 60 deg are presented. At $\mu = 0.05$ (fig. 31a) there is a smooth variation in pressure from the fuselage nose to the tail, since there are no close interactions with the tip vortices (fig. 30a). At this low advance ratio the pressure coefficient increments caused by the moving bound vortices that represent the blades are quite large, reaching $C_p = +10.5$. The other major effect is the large negative pressure coefficients ($C_p = -6$) induced on the aft fuselage by the wake vorticity. At advance ratios of $\mu = 0.15$ and above (figs 31b, c and d), the pressure distributions are all qualitatively similar to each other, since the tip vortices pass over the top of the fuselage in each case. In each case the effects of the overall wake, the tip vortices, and the moving bound circulation are superimposed on the isolated rotor pressure distribution (fig. 23). As advance ratio increases, the relative strength of the rotor and wake contribution to the pressure coefficient decreases, and the surface pressure distributions more closely resemble the isolated fuselage solution. The spatially periodic pattern spreads out at higher advance ratios, since it is driven by the tip vortex structure (fig. 30). The number of pressure peaks along the fuselage surface decreases from 7 at $\mu = 0.15$ to 3 at $\mu = 0.35$.

The basic characteristics of the unsteady airloads are not changed significantly by changing advance ratio. The unsteady lift, drag and side force variations with blade azimuth for advance ratios of μ = 0.05, 0.15, 0.20, 0.25, 0.35, and 0.45 are shown in figure 32a-f, respectively. The equivalent results for μ = 0.10 were shown in figure 25a. Figure 33 shows the lift for all seven advance ratios on the same axes. The lift force generally remains in phase with the motion of the blades, and the peak-to-peak amplitude remains between 3.2 to 4.3% of the rotor thrust at lower advance ratios, $\mu \leq 0.20$. The unsteady lift amplitude increases at higher advance ratios, reaching 6.3% of the thrust at μ = 0.45. It must be noted that the rotor performance for this particular configuration is not good at this advance ratio, requiring a significant pitch-down of the aircraft, and an increased wake-fuselage interaction. The increase in unsteady airloads may therefore not be representative of a more realistic rotor system. A further distinction between this configuration and a conventional helicopter is the proximity of the ellipsoid nose and tail to the rotor blades at ψ = 0 deg. This will magnify the effect of the moving bound vortex interaction, and may generate higher unsteady airloads than would be present for an actual helicopter, which generally has a larger separation between the blades and the fuselage.

The variation in the rotor/fuselage interaction with advance ratio also affects the solution for the rotor. The strength of the velocities induced by the fuselage at the rotor disc increases proportionally with the flight speed, as shown in figure 34. This figure shows the induced velocities at r/R = 0.75 at the seven advance ratios. In addition to the change in the magnitude of the induced axial velocity with flight speed, there is a change in the shape of the azimuthal distribution. This change is a result of the coupled interaction of the rotor and fuselage flows. Note that the fuselage-induced velocities are not the only way in which the fuselage changes the flow about the rotor: the displacement of the wake will also change the wake-induced velocities at the rotor.

Effect of Changing Wake Displacement Parameters

The results presented so far have used 'standard' values of the two primary wake displacement parameters: a wake offset distance of 10% of the local body radius and a wake that splits at a fuselage cross-section angle of -75 deg. The sensitivity of the results to changes in these parameters will now be examined. Results at several advance ratios were obtained using the ellipsoidal fuselage and four-bladed main rotor.

Wake Displacement Radius.-The effect of varying the distance that the wake is offset from the fuselage surface was studied by computing the unsteady fuselage airloads at $\mu = 0.15$ using four different wake displacement values: 0.02, 0.10, 0.30, and 0.90 times the local body radius. This advance ratio was selected because it represents a relatively high degree of wake - fuselage interaction. Figure 35a shows a side view of the ellipsoid, rotor, and wake, with a displacement of 0.02r, while figure 35b shows a side view with a displacement of 0.30r. The equivalent results with the standard displacement of 0.10r were shown in figure 30b. A fifth computation was made with the strength of the vortices that are displaced about the fuselage set to zero (the Γ=0 case). The fuselage aerodynamic lift forces for the five cases are shown in figure 35c. The phase and unsteady peak-to-peak amplitude are not significantly affected, while the mean lift force varies by up to 1% of the rotor thrust. The peak positive unsteady lift is greatest using a displacement distance of 0.10r, apparently because the fuselage is within the tip vortex cores at a displacement of 0.02r, and the tip vortices have been pushed relatively far from the fuselage at a displacement of 0.30r. Both of these effects reduce the wake-fuselage interaction. At a displacement of 0.90r and for $\Gamma = 0$, the peak positive lift is further reduced, probably because of the greatly reduced (or eliminated) effect of the vortices. Since there does not seem to be any strong dependence on small changes in the displacement distance, the standard value of 0.10r will continue to be used until experimental or other evidence indicates another value to be more appropriate.

Wake Split Angle.- The wake split angle defines where each wake filament shifts from passing over the fuselage to passing underneath it. The angle is defined between the horizontal and a line connecting the center of the local fuselage cross-section to the point where the filament would have intersected the fuselage surface if it had not been displaced. Figure 36 shows side views of the ellipsoid, rotor, and wake, at an advance ratio of $\mu = 0.10$, with split angles of 0, -45, and -90 deg. This advance ratio was chosen because the wake passes at a shallow angle across the entire fuselage, allowing the largest variation in split angle. At higher advance ratios ($\mu > 0.20$) the wake will always pass over the top of the fuselage. A side view with the standard split angle of -75 deg was shown in figure 22b. At a split angle of 0 deg (fig. 36a) the majority of the wake passes below the fuselage, while at -90 deg (fig 36b) all of the wake remains above the fuselage. Figure 37 shows the computed fuselage lift using split angles of -90 deg, -75 deg, -45 deg, 0 deg, and +90 deg. The results using split angles of -90, -75, and -45 deg have similar unsteady lift amplitudes, phases, and mean values, while the results using split angles of 0 and +90 deg have mean downloads that are increased by about 2% of the rotor thrust. A wake split angle of -75 deg was selected as the standard value since it appears to be physically reasonable, and gives results that do not have a great sensitivity to small variations in the split angle.

Results using the UTRC Generalized Wake Model

A generalized forward flight wake module (ref. 18) may be used to approximate the effects of tip vortex distortion. In this model the computed classical wake tip filaments are distorted using prescribed shape and envelope functions. The wake distortion is dependent on the wake age, blade azimuth position, advance ratio, and thrust coefficient. This approach provides a cost effective approximation to the results obtained using free wake techniques. If required, the tip filament geometry obtained from the generalized wake functions is further displaced about the fuselage using the techniques described above. Figure 38 shows the ellipsoidal fuselage and the distorted tip filament from a single blade at an advance ratio of $\mu = 0.10$. The filaments representing the inboard sheet are not changed by the wake generalization, and are displaced only when in the presence of the fuselage.

A coupled rotor/fuselage computation was performed at advance ratios of $\mu = 0.05$, 0.15, and 0.35. The fuselage attitude and rotor control angles were determined using the rigid blade analysis. The only major change from the results using the classical wake model was an increase in the collective and cyclic pitch at $\mu = .05$. The fuselage attitude and the rotor control angles at the other advance ratios changed less than 0.1 deg. Figure 39 shows a side view of the wake geometry in each case. In general the tip vortices are displaced well above the position of the classical wake, so that they pass over the front of the fuselage at $\mu = 0.05$ (fig. 39a), and completely above the fuselage at $\mu = 0.15$ (fig. 39b) and at $\mu = 0.35$ (fig. 39c). At $\mu = 0.05$ the wake interaction creates a region of flow reversal near the upper front of the fuselage and a very high downwash at the rear of the fuselage. At higher advance ratios there are no large variations in surface flow direction. This contrasts with the classical wake results, where the tip vortices contact the fuselage again at advance ratios of $\mu = 0.35$ and 0.45 (figs. 30 e-f).

Figure 40 shows the surface pressures along the top of the fuselage at blade azimuths of 0, 15, 30, and 60 deg. The results are qualitatively similar to the classical wake results (figs. 31 a, b, and d), but there are several significant differences. At $\mu = 0.05$, there is a stronger interaction between the fuselage and the generalized wake, producing lower fuselage pressures between $z/R = 0.3$ and 0.7, and higher pressures between $z/R = 1.0$ and 1.4 (fig 40a). The strong influence of the moving bound vortices is present with either wake geometry model. At $\mu = 0.15$ (fig. 40b) and $\mu = 0.35$ (fig. 40c) the spatial periodicity caused by the tip vortex pattern is still present, but is weakened because the vortices are further away from the fuselage in the generalized wake model. The fuselage airloads (fig. 41) are also somewhat different when the generalized wake model is used. At $\mu = 0.05$ (fig. 41a) the peak-to-peak amplitude of the unsteady lift is about 4.5% of the rotor thrust, an increase over the the value of 3.5% obtained using the classical wake model (fig. 32a). The mean lift on the fuselage increases from -1.2% of the rotor thrust using the classical wake model to +3.7% using the generalized wake model. The phase and the general character of the unsteady waveform are not significantly changed. At $\mu = 0.15$ (fig. 41b) and $\mu = 0.35$

(fig. 41c) the wake-fuselage interaction is much less important; therefore the unsteady airload amplitudes, phases, and waveforms are quite similar to the classical wake results (figs. 32 b and e). There is also a small increase in the computed mean download when the generalized wake model is used. These results demonstrate that, for this configuration, the geometry of the wake model is of primary importance in determining the fuselage airloads only at lower advance ratio, when there is a strong wake-fuselage interaction. At higher advance ratio the wake-fuselage interaction is weaker, and it is the moving bound vortices that have the greatest influence. Under these conditions, the fuselage airloads are not highly dependent on the wake model.

Results for a Helicopter Fuselage

An ellipsoidal fuselage has been used in the studies described above. The analysis was also applied to a shape more representative of an actual helicopter fuselage (a Sikorsky S-76). A side view of the 432 panel representation of the fuselage is shown in figure 42. Also shown is the four-bladed main rotor and the wake at $\mu = 0.05$. The generalized wake model has been used to distort the tip vortex filaments. The rotor is the same as that used for the ellipsoidal fuselage studies, and does not represent the S-76 rotor. Flight control settings and dynamic parameters are also not representative of the S-76.

Figure 43 shows instantaneous surface pressures along the top of the fuselage at advance ratios of $\mu = 0.05$, 0.15, and 0.35. The mean pressure on the isolated helicopter fuselage at $\alpha = 0$ is also shown. The canopy, engine cowling, and tail boom cause the isolated fuselage pressures to be more complex than for the ellipsoid, however the additional pressures induced by the rotor and wake are qualitatively similar to those observed using the ellipsoid (fig. 40). At $\mu = 0.05$ there is still a large wake-fuselage interaction that begins above the canopy (fig. 42). This interaction, in combination with the moving bound vortex effect, induces very large variations from the isolated fuselage pressures (fig. 43a). The surface pressure coefficient varies from $C_p = -12$ on the forward fuselage to $C_p = +6$ on the aft fuselage. At $\mu = 0.15$ (fig. 43b) and at $\mu = 0.35$ (fig. 43c) the wake interaction is much weaker (note the change in scale from fig. 43a), and since the rotor blades are relatively far from the fuselage, the pressures are much closer to the isolated fuselage values than was true for the ellipsoid (fig. 40). There are still identifiable contributions from the wake and the moving bound vortices, but they are relatively small at the higher advance ratios.

The unsteady airloads are also reduced when the helicopter fuselage is used (fig. 44). At $\mu = 0.05$ (fig. 44a) the peak-to-peak lift amplitude is reduced to about 2.2% of the rotor thrust, but the harmonic content of the waveform is increased. The mean lift is not greatly changed. The primary reason for the changes appears to be the absence of the strong blade-fuselage interaction, which generated a very strong pressure pulse on the ellipsoid at each blade passage (fig. 41). The unsteady peak-to-peak lift amplitude is

reduced further at the higher advance ratios, to 1.3% of the rotor thrust at $\mu = 0.15$ (fig. 44b) and to 1.5% of the rotor thrust at $\mu = 0.35$ (fig. 44c). The mean lift and the phase of the unsteady components are similar to the values for the ellipsoid.

The different fuselage geometry also alters the velocities at the rotor. Figure 45 shows the three velocity components at $r/R = 0.75$ for the helicopter and ellipsoidal fuselages. The peak positive axial velocity of 1.3 m/sec (4.3 fps) over the front of the ellipsoid is reduced to 0.9 m/sec (3.1 fps) over the nose of the helicopter, and the peak negative velocity of -1.4 m/sec (-4.6 fps) over the rear of the ellipsoid is reduced to -0.5 m/sec (-1.6 fps) over the tail of the helicopter.

Finally, an application to sideward flight is shown in figure 46 to demonstrate the versatility of the analysis. The analysis may be run and the wake displaced over a fuselage at arbitrary pitch and yaw angles. The wake geometry at a fuselage yaw angle of 90 deg is shown in figure 46a. The computed fuselage surface velocities for this case are shown in figure 46b. Note that in sideward flight, as in all other flight conditions, the potential flow methods used do not account for the effects of flow separation.

Comparison with Experimental Data

One of the major premises of this analysis is that the displacement of the wake around the fuselage can be prescribed using simple geometric rules. Another is that a discrete singularity/potential flow approach can be used to simulate rotor/wake/fuselage interactions. Extensive experimental data is needed to define the wake displacement characteristics, to validate the model, and to suggest improvements. A complete set of local unsteady fuselage pressures, unsteady airloads on the fuselage and rotor, and wake visualization results are required. Unfortunately such extensive data are not available. Recent tests at the Georgia Institute of Technology have measured mean and unsteady pressures on a cylindrical body in the wake of a two-bladed rotor. Data were obtained at several advance ratios and relative rotor/fuselage positions. Details of the model configuration and test conditions are given in references 24 and 31-33. No body or rotor balance measurements or extensive flow visualization results were presented. An initial application of the rotor/fuselage analysis to this geometry has been made. A top view of the cylinder, rotor, and computed wake geometry is shown in figure 47a. The analysis was run at an advance ratio of $\mu = 0.10$, with the rotor hub located 0.3 rotor radii above the cylinder axis (0.14 radii above the surface), and 1.0 radii downstream of the nose of the cylinder. These conditions correspond to those of Tables 2 and 11 of reference 32. The rotor was untwisted and had a fixed pitch of 10 deg. As shown in the side view (fig. 47b), the generalized wake model was used to distort the tip vortex filaments. The four blacked-out panels shown in figure 47 represent unsteady pressure measurement stations used during the experiment.

Mean surface pressure distributions along the top of the fuselage will be compared first. The experimental measurements are compared in figure 48 with the computational results for an isolated fuselage and for the mean of the unsteady rotor-fuselage analysis. The influence of the rotor and wake on the fuselage aerodynamics for this configuration is obvious from this figure, as the surface pressure coefficients are increased above the isolated fuselage values by $\Delta C_p = 1.8$ in the region of maximum rotor and wake influence. There are qualitative similarities between the results of the rotor-fuselage analysis and the experiment, but there are also significant differences, particularly on the forward fuselage, where there is a strong interaction with both the rotor blades and the wake. Several factors may contribute to the differences:

1) The analytical generalized wake geometry does not correctly predict the actual location of the wake. Reference 24 indicates that tip vortices will intersect the fuselage at $z/R = 0.35$ and 0.55 at $\psi = 0$, while the model predicts that the intersections will occur at $z/R = 0.28$ and 0.67. Such differences will change the wake-fuselage interaction, and may cause a major change in the fuselage pressures on the forward fuselage. No information was available in Ref. 24 on the position of the inboard vortex sheet, which may also be incorrectly predicted in the analysis.

2) The viscous interaction between the wake and the fuselage may not be correctly modelled, especially at the relatively low Reynolds numbers present during this experiment. The results in Ref. 33 indicate that the wake filaments break upon contact with the fuselage, and do not reconnect below the fuselage (as is assumed by the analysis). This will also change the predicted surface pressures. Unsteady rotor-fuselage computations were made using several combinations of the tip vortex core size and wake displacement distance. A core size of 0.02 rotor radii (9 mm) was used for the presented results, based upon the experimental measurements (Ref. 33). A wake displacement distance of 0.05 body radii (13.4 mm) was found to give slightly better agreement than values of 0.10 and 0.15 body radii.

3) The wake vortices are likely to mix and lose their discrete identities once they have left the vicinity of the rotor. The lack of a mixing model in the analysis may account for the negative pressure coefficients that are predicted for $2.3 < z/R < 2.9$, rather than the smooth approach to $C_p = 0$ that was experimentally measured. Such a smooth drop is consistent with a well-mixed flow. Unsteady airfoil measurements (Ref. 34) have shown that high flow unsteadiness (such as occurs here) accelerates wake mixing. This problem is unlikely to be resolved using wake models that have discrete filaments.

It must also be noted that the proximity of the rotor blade tip to the nose of the fuselage in this experiment (fig. 47) is not typical of current helicopter designs, and will produce a much stronger rotor-wake-fuselage interaction. The effect of blade thickness (moving sources and sinks) may be significant in this experiment, where the blade passes within a few chord-lengths of the surface. Thickness effects are not included in the present lifting line blade model. Therefore failure to correctly predict this strong

interaction does not necessarily imply failure to predict the weaker interaction found on an actual aircraft (fig. 42). Alternatively, a model that is able to correctly predict the strong interaction from first principles (without relying on experimental wake geometry or on total pressure measurements) will generate a high degree of confidence in its ability to work for less demanding configurations.

Figure 49 shows the computed instantaneous pressure bodylines along the top, the bottom, and the advancing and retreating blade sides of the cylinder, at azimuthal angles of 0, 15, 60, and 120 deg. No experimental data in this form were available for comparison. The pressures on the top surface (fig. 49a) show a very strong blade-fuselage interaction at $\psi = 0$ for $z/R < 0.5$. A peak pressure coefficient of $C_p = +14.2$ is reached near $z/R = 0.1$. The effect of this interaction is highly concentrated in space and in time, so that any small error in the relative position of the blade and the fuselage would create a sizable error in the predicted pressures. At azimuth angles where the blades are further from the fuselage, the interaction with the tip vortices is dominant for $0 < z/R < 1$ and for $2.4 < z/R < 2.9$. The spatially periodic pattern in the pressures move aft along the fuselage and shifts from the top to the bottom surface (fig. 47). A particularly strong interaction is computed to occur on the bottom of the fuselage at $z/R = 0.9$ and $\psi = 0$ (fig. 49c). This particular interaction is probably not realistic, since it assumes that the tip vortices will reform with undiminished strength after passing over the fuselage.

Unsteady pressure data were reported in Ref. 32 at four longitudinal stations along the fuselage. The locations along the top bodyline were indicated in figure 47. Figure 50 compares the measured and computed pressures at these four locations. Away from the region of strong tip vortex-fuselage interaction ($z/R = 0.6$, fig. 50a), there is fair qualitative agreement, in terms of mean level, unsteady amplitude, phase, and waveform. The strong interaction on the forward fuselage is clearly overpredicted. Note that $z/R = 0.6$ is downstream of the region of maximum blade-fuselage interaction (fig. 49a). At $z/R = 0.6$ the wake-fuselage interaction appears to be the primary influence. It is possible that altering the models used for the generalized wake geometry or for the interaction of the wake with the fuselage (such as by changing the vortex core size or the effect on vortex strength of stretching a filament around the fuselage) will improve the correlation. This initial correlation did not determine optimum values for the parameters in the wake model: the only variation studied was in the distance that the wake was displaced away from the fuselage (which did not produce any major changes in the results). The standard values were used for all other parameters. No experimental information (beyond the geometry of the rotor and fuselage and the estimated tip vortex core size) was used in the calculation.

CONCLUSIONS AND RECOMMENDATIONS

A computational analysis of unsteady helicopter rotor, wake, and fuselage interactions has been developed. Singularity methods (lifting line rotor, prescribed vortex filament wakes, and a source panel fuselage) are used to determine an unsteady, inviscid potential flow solution. The fuselage surface pressures are determined by evaluating the unsteady, incompressible Bernoulli equation, accounting for the effect of the moving bound vortices of the rotor and the unsteady effect of the convection of the wake. The aerodynamic analysis may be coupled with either a rigid blade or aeroelastic rotor response program. The solution will predict the unsteady velocities, pressures, and airloads on the fuselage, the position of t e rotor and wake, and the induced velocities and airloads on the rotor. A graphics package was created to display these results, to show the position of the fuselage, rotor, and wake at any azimuthal position, and to display the magnitude and direction of the velocities on the fuselage surface. The analysis was demonstrated using an ellipsoidal fuselage and a four bladed rotor. The influence of the two main parameters used to prescribe the interaction between the wake and the fuselage (the distance that the wake is offset from the fuselage surface and the angle at which the wake shifts from passing over the fuselage to passing under the fuselage) was found to be relatively small for this test configuration.

Solutions were first determined using the ellipsoid with a classical wake model at advance ratios between $\mu = 0.05$ and $\mu = 0.45$. The unsteady fuselage pressures are primarily determined by the interactions with the moving bound vortices that represent the rotor blades and with the tip vortex filaments. The interactions are most significant at low advance ratio, where the induced pressures are large in comparison with the freestream dynamic pressure. The absolute magnitude of the blade-fuselage interaction is primarily determined by the relative geometry of the rotor and fuselage and by rotor thrust, and is therefore relatively independent of advance ratio. The wake geometry was highly dependent on advance ratio: at higher advance ratios the wake passes completely over the fuselage, weakening the interaction. The unsteady fuselage airloads obtained by integration of the surface pressures have a fundamental frequency equal to the blade passing frequency, but include some higher harmonic content. For this configuration the phase and waveform do not change significantly with advance ratio. The peak-to-peak amplitude of the unsteady fuselage lift is about 4% of the rotor thrust for $\mu \leq 0.20$, and rises to 6% of the rotor thrust at $\mu = 0.45$.

Inclusion of the UTRC generalized wake model to distort the tip vortex filaments and approximate the actual wake geometries altered the wake-fuselage interaction and therefore the unsteady fuselage airloads. This effect is most noticeable at $\mu = 0.5$, where the tip vortices are brought into direct contact with the fuselage by the generalized wake model, increasing the unsteady lift amplitude from 3.5% to 4.5% of the rotor thrust. The effects are much smaller at higher advance ratio.

The analysis was also demonstrated using a simulated helicopter fuselage. Compared with the ellipsoid, the lower nose and tailboom of the helicopter increases the distance between the rotor and fuselage and therefore weakens the interaction with the blades and the wake. The unsteady lift amplitude is reduced to between 1.3% and 2.2% (depending on advance ratio) of the rotor thrust. The reduced importance of the more sinusoidal blade-fuselage interaction increases the harmonic content in the airload waveforms. The overall phase and the mean values are not significantly changed.

A limited comparison was made between the computational results and fuselage pressures measured in an experiment at the Georgia Institute of Technology. The computation was made using the standard prescription for the wake geometry and for the interaction between the wake and the fuselage; no adjustments were made to match experimental wake positions. Fair qualitative agreement was obtained for the mean pressures along the top of the fuselage. Point comparisons of the unsteady pressures were also qualitatively successful away from the region of strong wake-blade-fuselage interaction near the nose. The differences may result from incorrect prediction of where the tip vortices approach the surface, and from the neglect of the wake mixing that occurs in the far wake and during the interaction between the wake and the fuselage.

Methods using discrete singularities to represent the rotor and wake have been found to provide acceptable predictions of the conditions at the rotor. The situation is different when the interaction with the fuselage is considered. The unsteady viscous interaction of wake filaments with other wake filaments and with the fuselage makes a discrete prescribed wake approach valid only up to the point of contact with the fuselage. Beyond this point the wake structure is not properly modelled by these methods. A solution that allows distributed vorticity may be required. Several improvements can however be made within the existing potential flow/discrete singularity framework:

1) The prescription of the wake geometry prior to contact with the fuselage and of the effect on the wake of a close interaction should be improved. A more accurate representation of this interaction is essential to prediction of the local fuselage pressures. Flow visualizations of wake-fuselage interactions may help establish the analytic rules. Alternatively, a free wake approach could be used to define the wake geometry before, during, and after the interaction.

2) The solution for the fuselage could be improved by replacing the source panels with vortex panels and adding a vortex sheet representation of the separation and wake of the fuselage itself.

3) The vortex filament representation of the inboard rotor wake could be replaced by a vortex box representation (ref. 35). This would account for the time-dependent changes in bound circulation at each lifting line segment, fully satisfy the irrotationality condition in forward flight, and clarify the geometry of the interaction of the inboard vortex sheet and the fuselage

Quantitatively accurate prediction of local pressures at all fuselage locations requires computation of the strong interactions between the wake vortices and the three-dimensional, viscous, unsteady, and frequently separated flow field about a geometrically complex fuselage. Since calculation of neither steady attached viscous flows over complex three dimensional geometries nor two-dimensional unsteady separated flows have yet been mastered, solution of this much more complex problem from first principles does not seem imminent. Therefore, simpler methods, such as that described in this report, will continue to be the only available source of computational information on rotor-fuselage interactions. Important qualitative results on the effect of vehicle geometry and flight condition on the steady and unsteady fuselage and rotor loads may be obtained using these methods. The limitations of the potential flow/singularity approach must, however, be understood in order for these results to be properly interpreted. Further, their accuracy cannot be established until a comprehensive correlation with experiment has been performed.

REFERENCES

1. Landgrebe, A. J., Moffitt, R. C., and Clark, D. R.: Aerodynamic Technology for Advanced Rotorcraft, Journal of the American Helicopter Society, Vol. 22, Nos. 2 and 3, April-July 1977 - Parts I and II.

2. Landgrebe, A. J.: Overview of Helicopter Wake and Airloads Technology, Proceedings of the American Helicopter Society/Nanjing Aeronautical Institute Intl. Seminar - The Theoretical Basis of Helicopter Tech., Nanjing China, Nov. 1985, also Proceedings of the 12th European Rotorcraft Forum, Paper No. 18, Garmisch-Partenkirchen, FRG, Sept. 1986.

3. Smith, R. V.: Some Effects of Wake Distortion Due to a Fuselage Flow Field on Rotor Thrust Limits, ARO Workshop on Rotor Wake Technology, Raleigh, North Carolina, April 17-18, 1976.

4. Sheridan, P. F. and Smith, R. P.: Interactional Aerodynamics - A New Challenge to Helicopter Technology, Preprint No. 79-59, Presented at the 35th Annual National Forum of the American Helicopter Society, Washington, DC, May 1979.

5. Wilson, J. C. and Mineck, R. E.: Wind-Tunnel Investigation of Helicopter-Rotor Wake Effects on Three Helicopter Fuselage Models, NASA TM X-3185, 1975.

6. Freeman, C. E. and Yeager, W. T., Jr.: Analytical and Experimental Investigation of V-Type Empennage Contribution to Directional Control in Hover and Forward Flight, Preprint No. 79-56, Presented at the 35th Annual National Forum of the American Helicopter Society, Washington, DC, May 1979.

7. Freeman, C. E.: Development and Validation of a Combined Rotor-Fuselage Induced Flow-Field Computational Method, NASA Technical Paper 1656 (also AVARDCOM TR 80-B-3), June 1980.

8. Huber, H., and Polz, G.: Studies on Blade-to-Blade and Rotor-Fuselage-Tail Interferences, AGARD-CPP-334, Paper No. 9, May 1982.

9. Betzina, M. D., Smith, C. A., and Shinoda, P.: Rotorbody Aerodynamic Interactions, Vertica, Vol. 9, No. 1, pp. 65-82, 1985.

10. Sopher, R., Studwell, R. E., Cassarino, S., and Kottapalli, S. B. R.: Coupled Rotor/Airframe Vibration Analysis, NASA CR-3582, Nov. 1982.

11. Egolf, T. A. and Landgrebe, A. J.: A Prescribed Wake Rotor Inflow and Flow Field Prediction Analysis, NASA CR-165894, June 1982.

12. Landgrebe, A. J. and Egolf, T. A.: Prediction of Helicopter Induced Velocities Using the Rotorcraft Wake Analysis, Proceedings of the 32nd Annual National Forum of the American Helicopter Society, May 1976.

13. Sheehy, T. H.: A Simplified Approach to Generalized Helicopter Configuration Modeling and the Prediction of Fuselage Surface Pressures. Paper presented at the National Symposium on Helicopter Aerodynamic Efficiency, American Helicopter Society - Northeast Region, March 1975.

14. Sheehy, T. W.: A Method for Predicting Helicopter Hub Drag, USAAMRDL-TR-75-45, 1975.

15. Clark, D. R. and Maskew, B.: Calculation of Rotor/Airframe Interference for Realistic Configurations, Eighth European Rotorcraft and Powered Lift Aircraft Forum, Paper No. 2.6, Aug-Sept. 1982.

16. Young, C.: Development of the Vortex Ring Wake Model and Its Influence on the Prediction of Rotor Loads, AGARD-CPP-334, Paper No. 11, May 1982.

17. Studwell, R. E.: User's Manual for the Automated Paneling Technique (APT) and the Wing Body Aerodynamic Technique (WABAT) Programs, NASA CR-165895, June 1982.

18. Egolf, T. A. and Landgrebe, A. J.: Helicopter Rotor Wake Geometry and Its Influence in Forward Flight, Volume I - Generalized Wake Geometry and Wake Effect on Rotor Airloads and Performance, NASA CR-3726, June 1983.

19. Egolf, T. A., and Landgrebe, A. J.: Generalized Wake Geometry of a Helicopter Rotor in Forward Flight and Effect of Wake Deformation on Airloads, Proceedings of the 40th Annual Forum of the American Helicopter Society, May 1984, pp. 359-376.

20. Landgrebe, A. J.: An Analytical Method for Predicting Rotor Wake Geometry, AIAA Paper No. 69-196, Feb. 1969.

21. Egolf, T. A. and Lorber, P. F.: An Unsteady Rotor/Fuselage Interaction Method, Proceedings of the American Helicopter Society National Specialist's Meeting on Aerodynamics and Aeroacoustics, February 1987.

22. Clark, D. R., and Maskew, B.: Calculation of Unsteady Rotor Blade Loads and Blade/Fuselage Interference, Proceedings of the Second International Conference on Rotorcraft Basic Research, University of Maryland, Feb. 1988.

23. Berry, J. D.: Prediction of Time-Dependent Fuselage Pressures in the Wake of a Helicopter Rotor, Proceedings of the Second International Conference on Rotorcraft Basic Research, University of Maryland, Feb. 1988.

24. Brand, A. G., Liou, S. G., Komerath, N. M., and McMahon, H. M.: Rotor-Airframe Aerodynamic Interaction Phenomena, Proceedings of the Second International Conference on Rotorcraft Basic Research, University of Maryland, Feb. 1988.

25. Rand, O.: The Influence of Interactional Aerodynamics in Rotor/Fuselage Coupled Response, Proceedings of the Second International Conference on Rotorcraft Basic Research, University of Maryland, Feb. 1988.

26. Bielawa, R. L.: Aeroelastic Analysis for Helicopter Rotors with Blade Appended Pendular Absorbers - Mathematical Derivations and Program User's Manual, NASA CR-165896, June 1982.

27. Loiselle, J. W.: Generalized Helicopter Rotor Performance Predictions, Master's Thesis, Naval Postgraduate School, Monterey, CA, Sept. 1977.

28. Lorber, P. F.: Program User's Manual for an Unsteady Helicopter Rotor-Fuselage Aerodynamic Analysis. NASA CR-181701, 1988.

29. Dean, R.C.: On the Necessity of Unsteady Flow in Fluid Machines: Transactions of the ASME, Journal of Basic Engineering, March 1959, pp. 24-28.

30. Preston, J.H.: The Non-Steady Irrotational Flow of an Inviscid, Incompressible Fluid, with Special Reference to Changes in Total Pressure through Flow Machines, The Aeronautical Quarterly, Nov. 1961, pp. 343-360.

31. Komerath, N. M., McMahon, H. M., and Hubbartt, J. E.: Aerodynamic Interactions Between a Rotor and Airframe in Forward Flight, AIAA Paper No. 85-1606, July 1985.

32. Brand, A. G., Komerath, N. M., and McMahon, H. M.: Wind Tunnel Data From a Rotor Wake/Airframe Interaction Study, Georgia Institute of Technology School of Aerospace Engineering Technical Report CERWAT-1-86, July 1986.

33. Brand, A. G., Komerath, N. M., and McMahon, H. M.: Results from Laser Sheet Visualization of a Periodic Rotor Wake, AIAA Paper No. 88-0192, January 1988.

34. Covert, E. E., Lorber, P. F., and Vaczy, C. M.: Measurements of the Near Wake of an Airfoil in Unsteady Flow, AIAA Paper No. 83-0127, Jan. 1983.

35. Egolf, T.A., and Sparks, S.P.: A Full Potential Rotor Analysis with Wake Influence Using an Inner-Outer Domain Technique, Journal of the American Helicopter Society, Vol. 32, No. 3, pp. 15-24, 1987

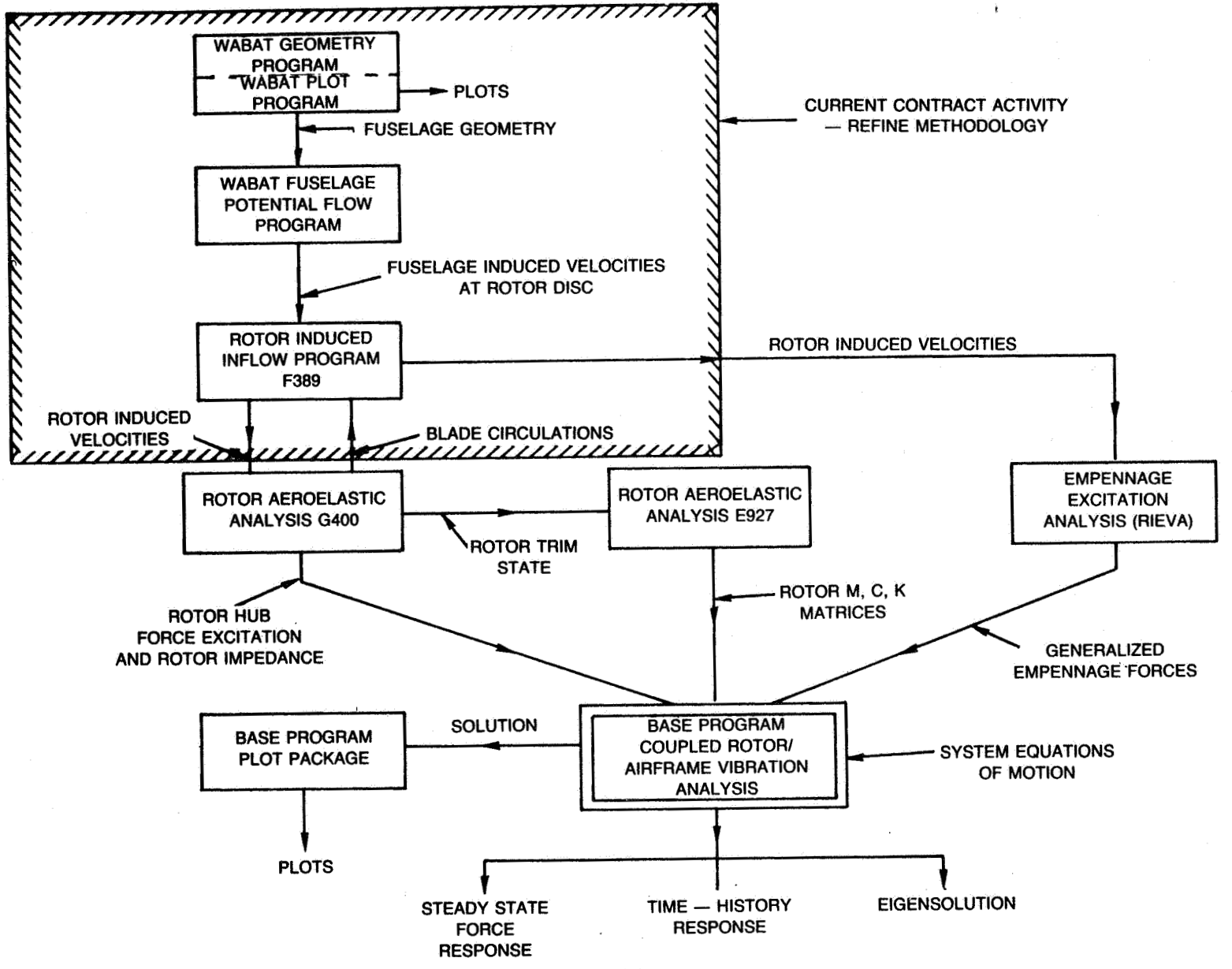

Figure 1. SIMVIB analysis.

87—11—47—1

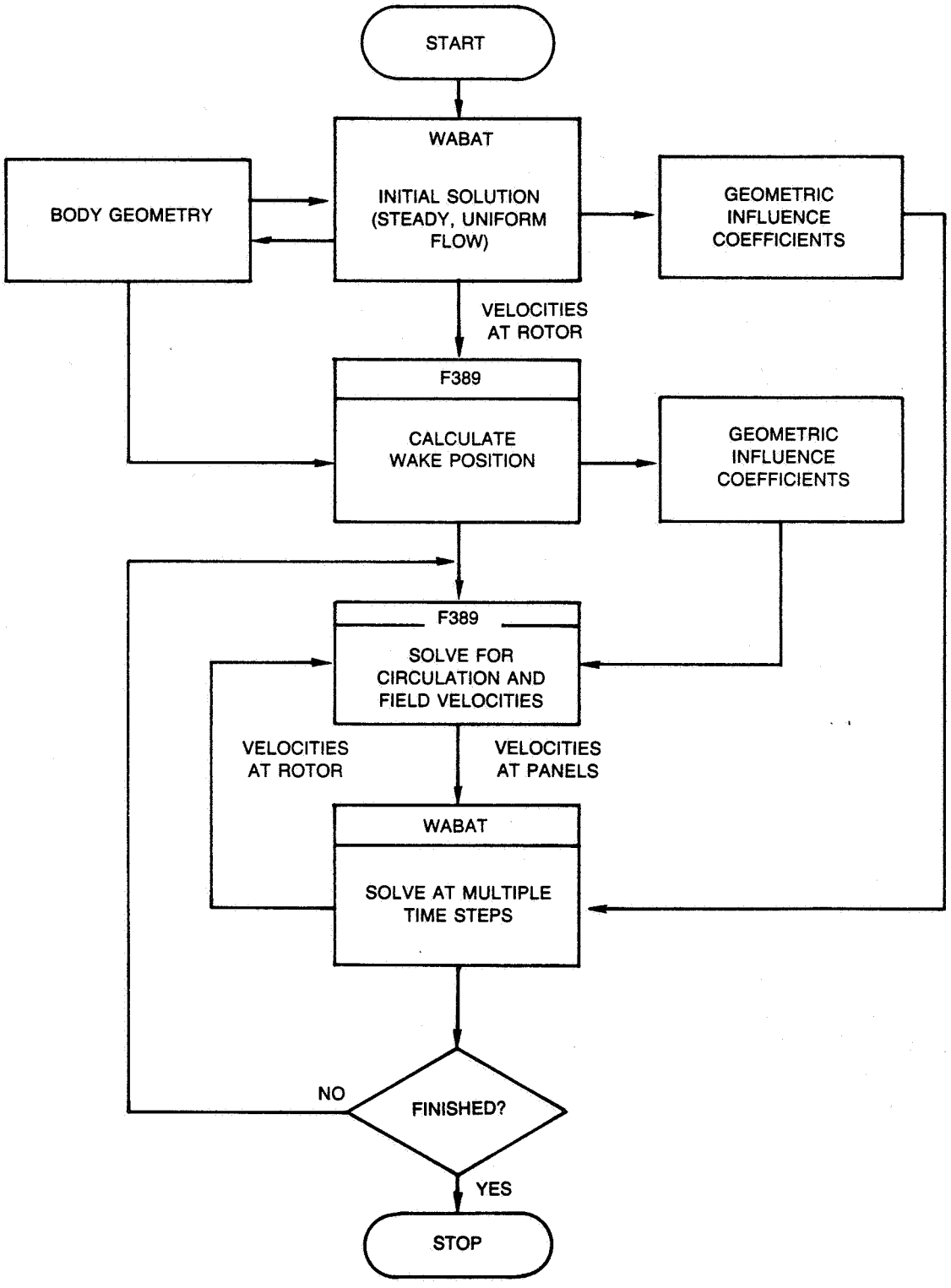

Figure 2. Program calling sequence for rotor/fuselage analysis.

87—11—47—2

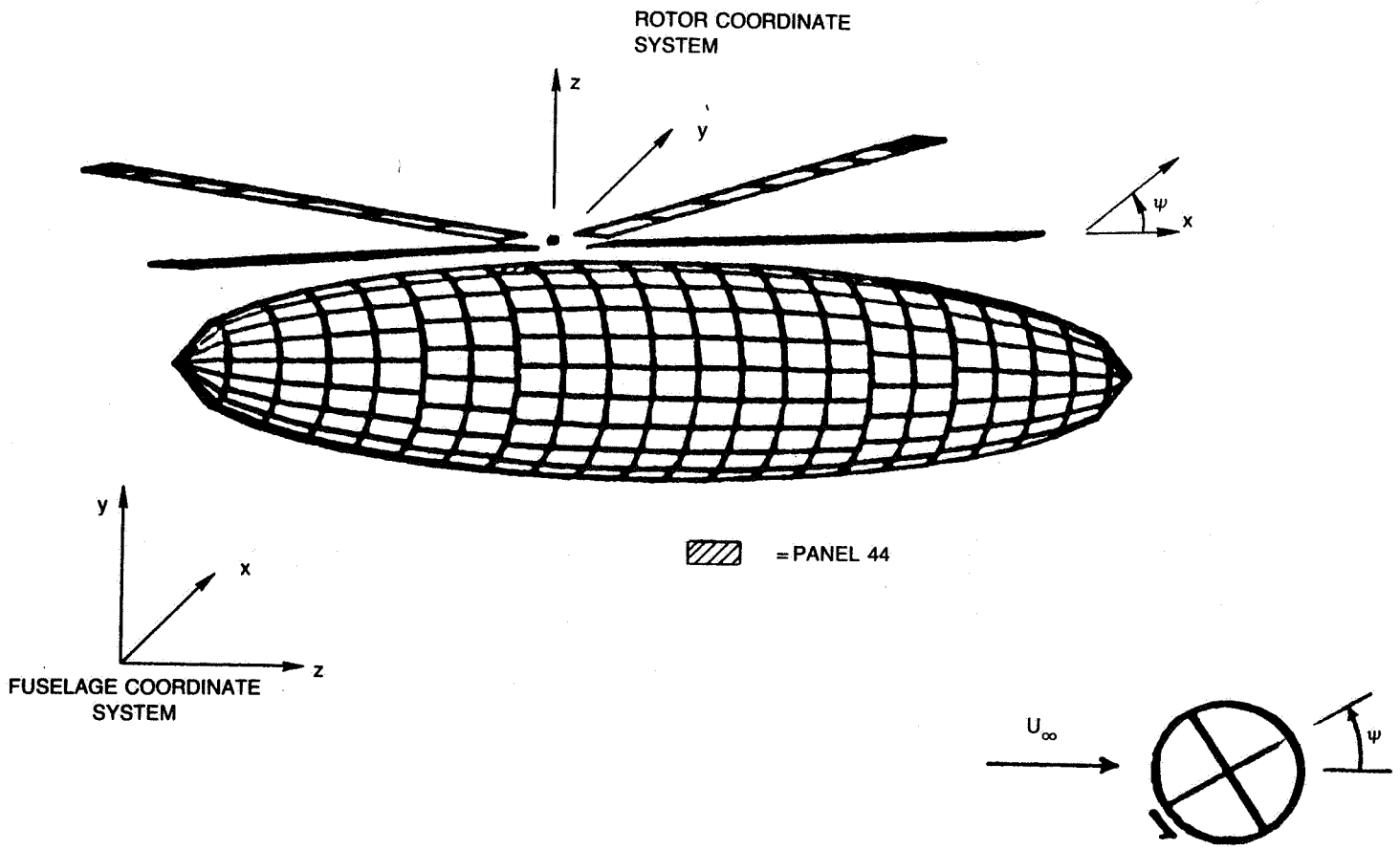

Figure 3. Rotor and fuselage geometry and coordinate systems.

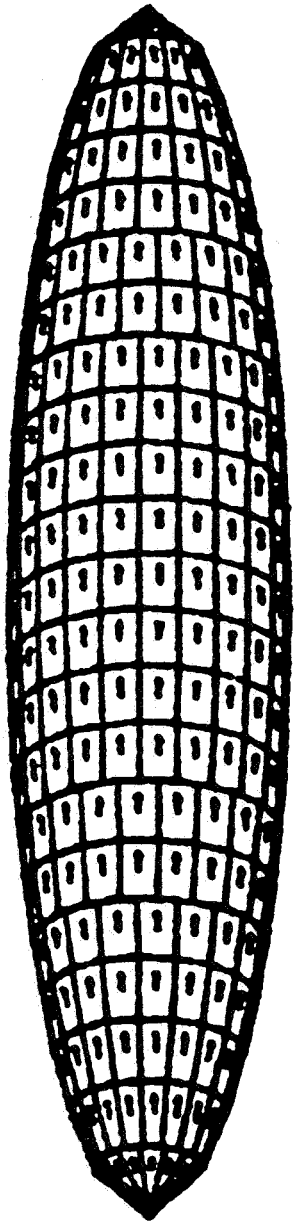

Figure 4. Surface velocity vectors for isolated fuselage.

87—11—47—4

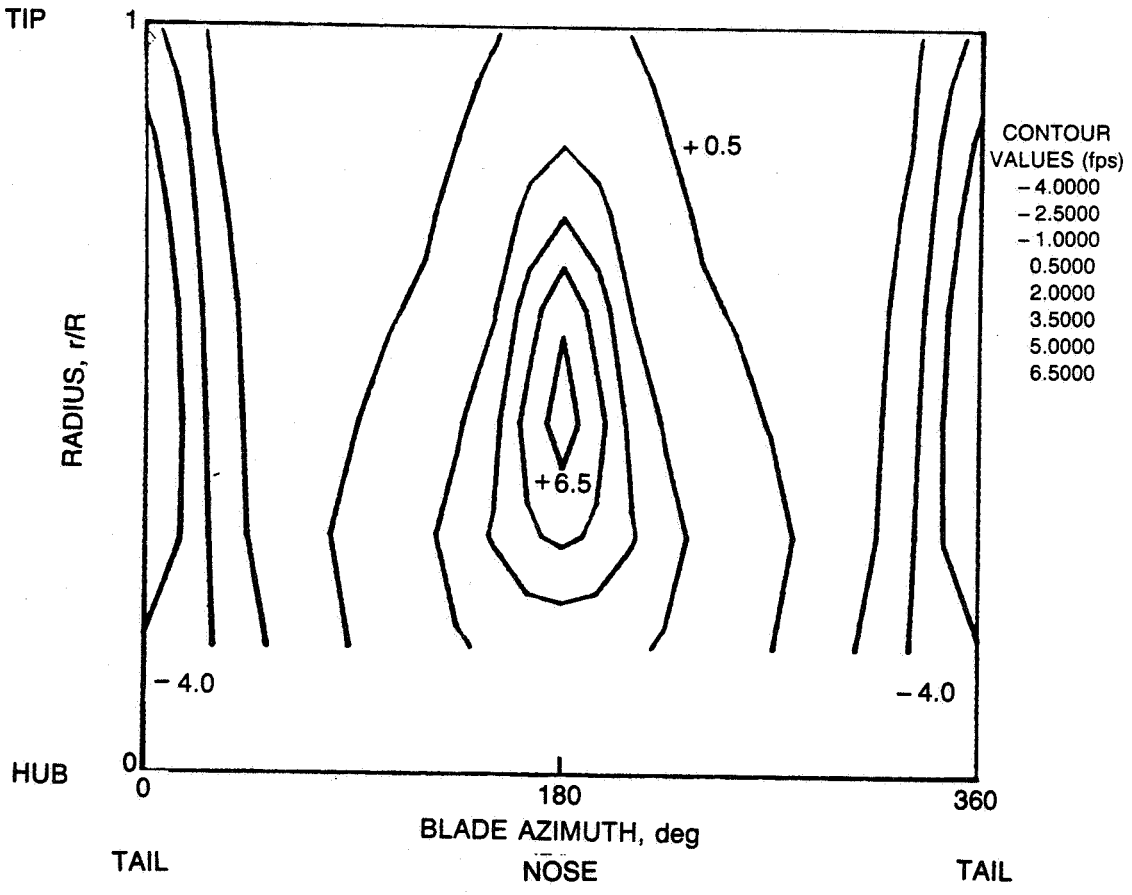

Figure 5. Fuselage-induced axial velocity at rotor — isolated fuselage.

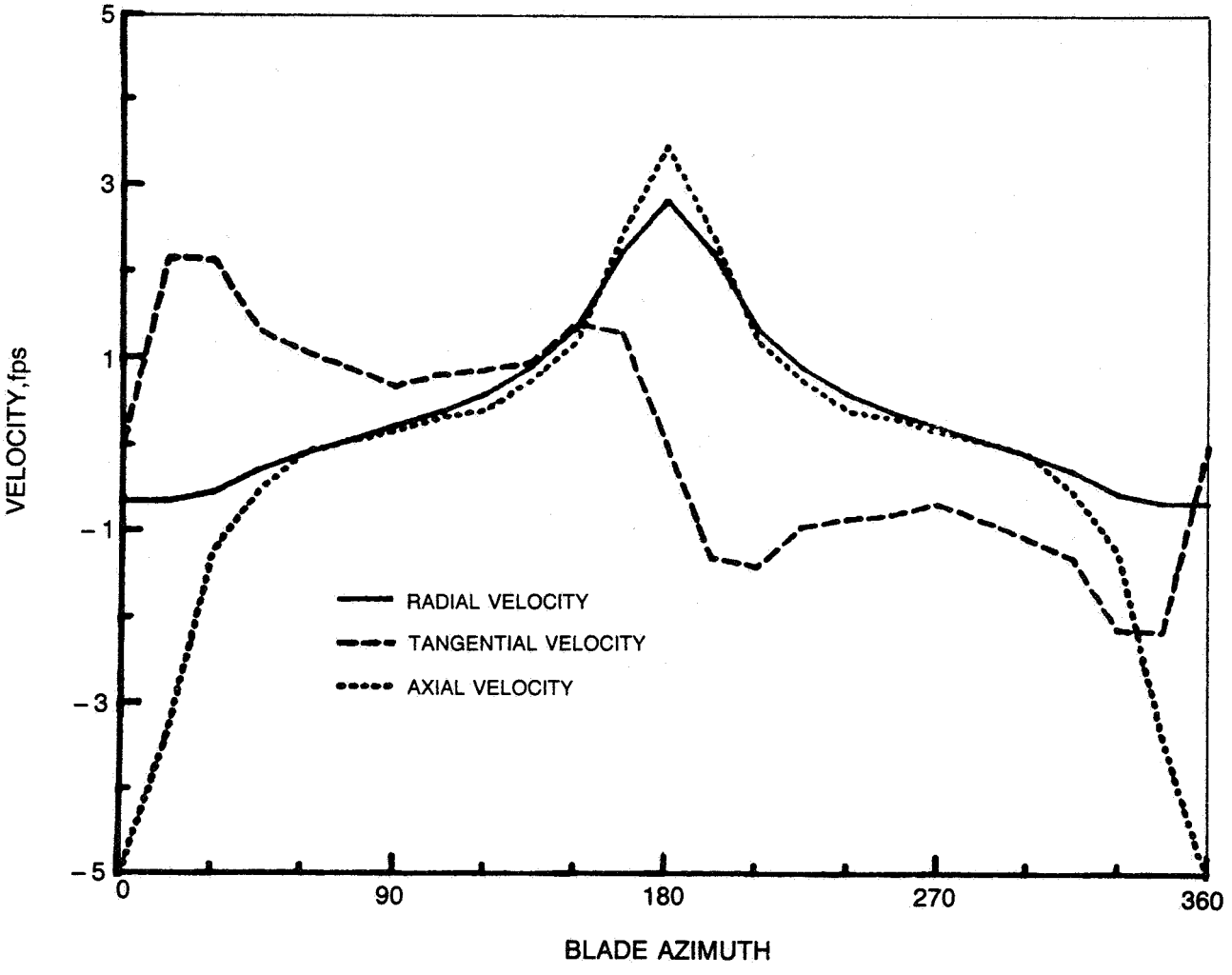

Figure 6. Fuselage-induced velocity at the rotor, r/R = 0.75, $\mu = 0.10$, isolated fuselage.

87—11—47—6

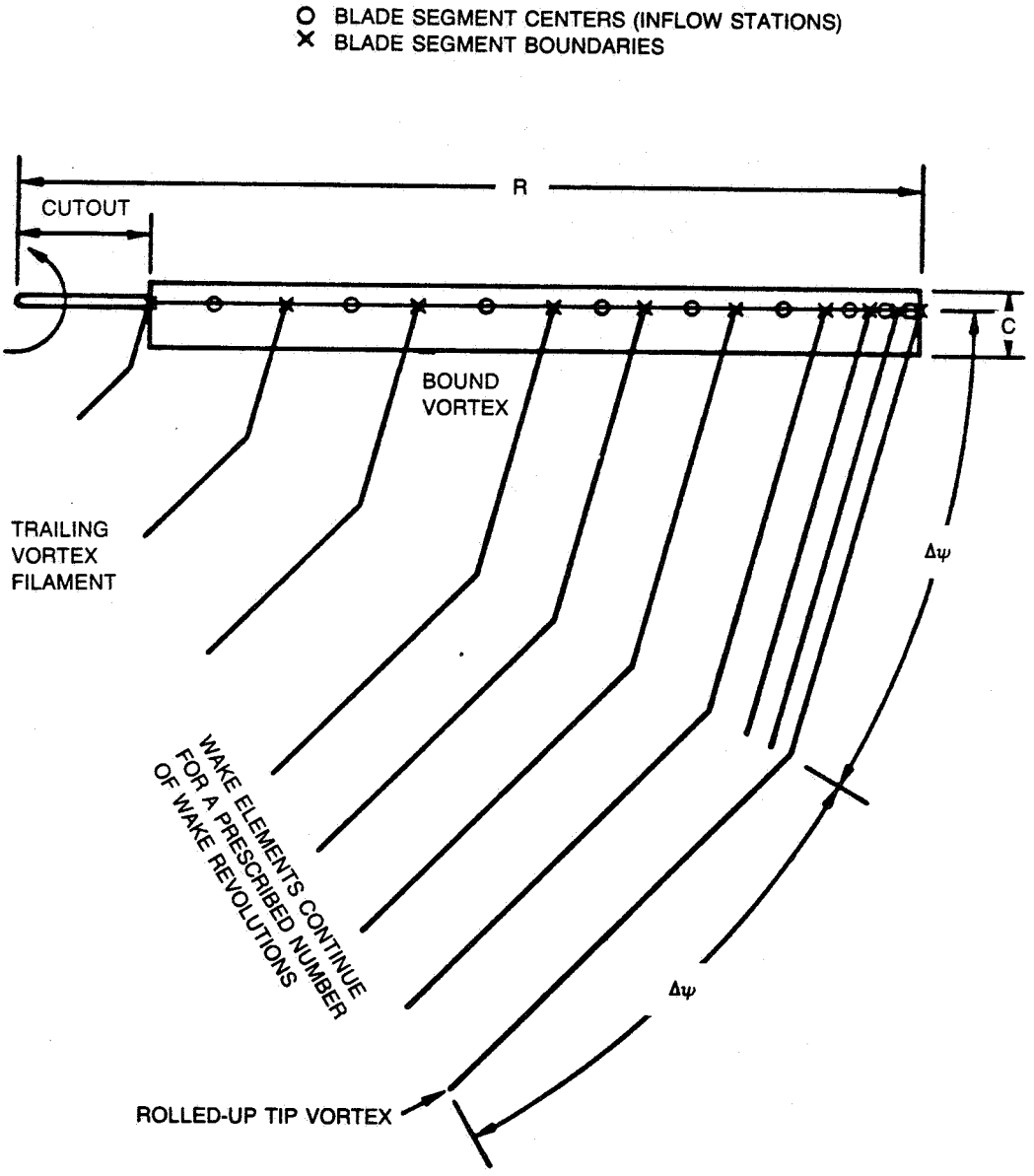

Figure 7. Representation of blade and wake by bound and trailing vortex segments

87—11—47—7

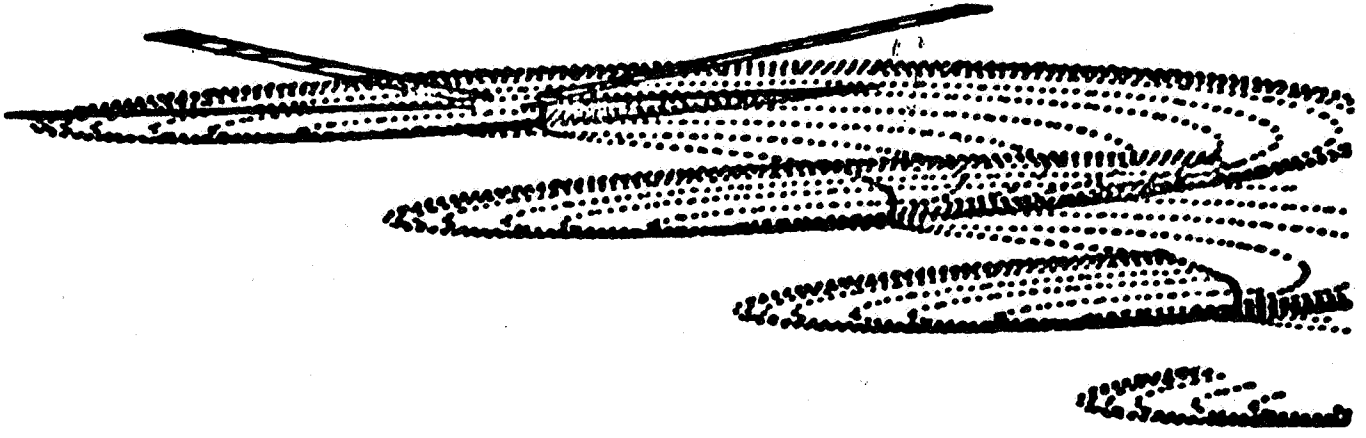

Figure 8. Classical wake geometry at $\mu = 0.10$.

87—11—47—8

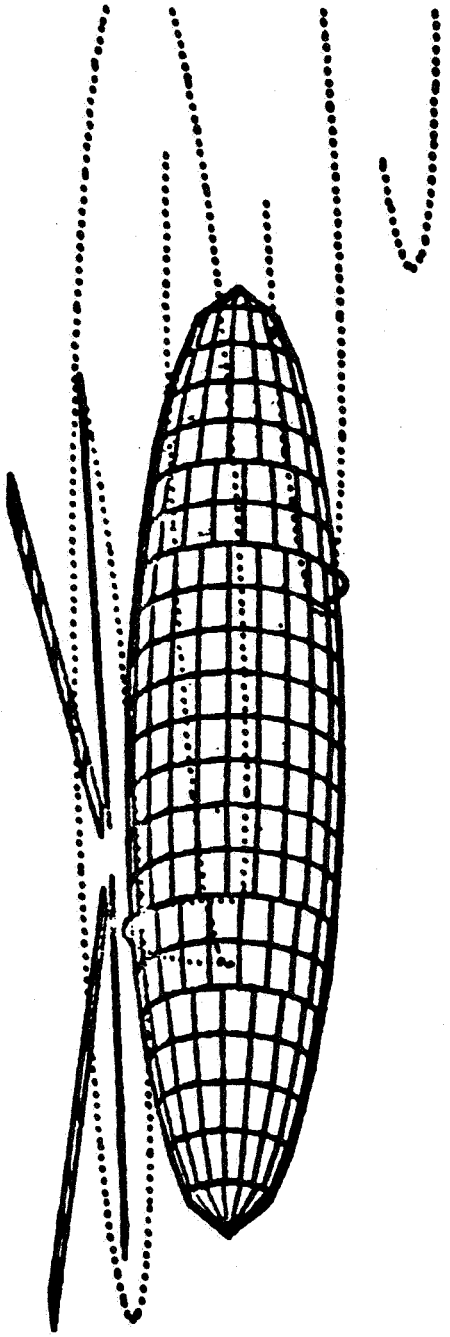

Figure 9. Single tip filament displaced about fuselage.

87-11-47-9

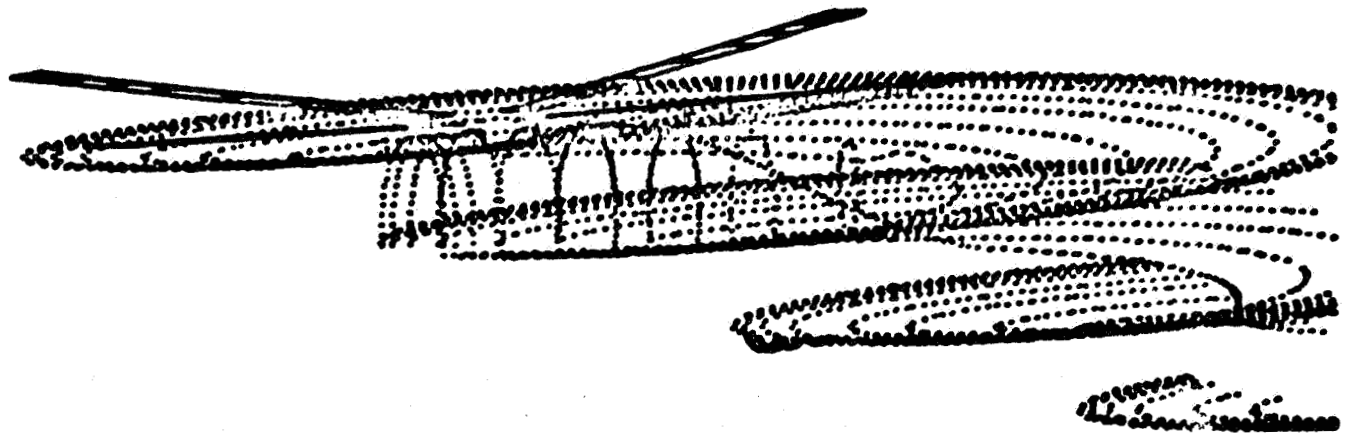

Figure 10. Displaced filaments from one blade.

87—11—47—10

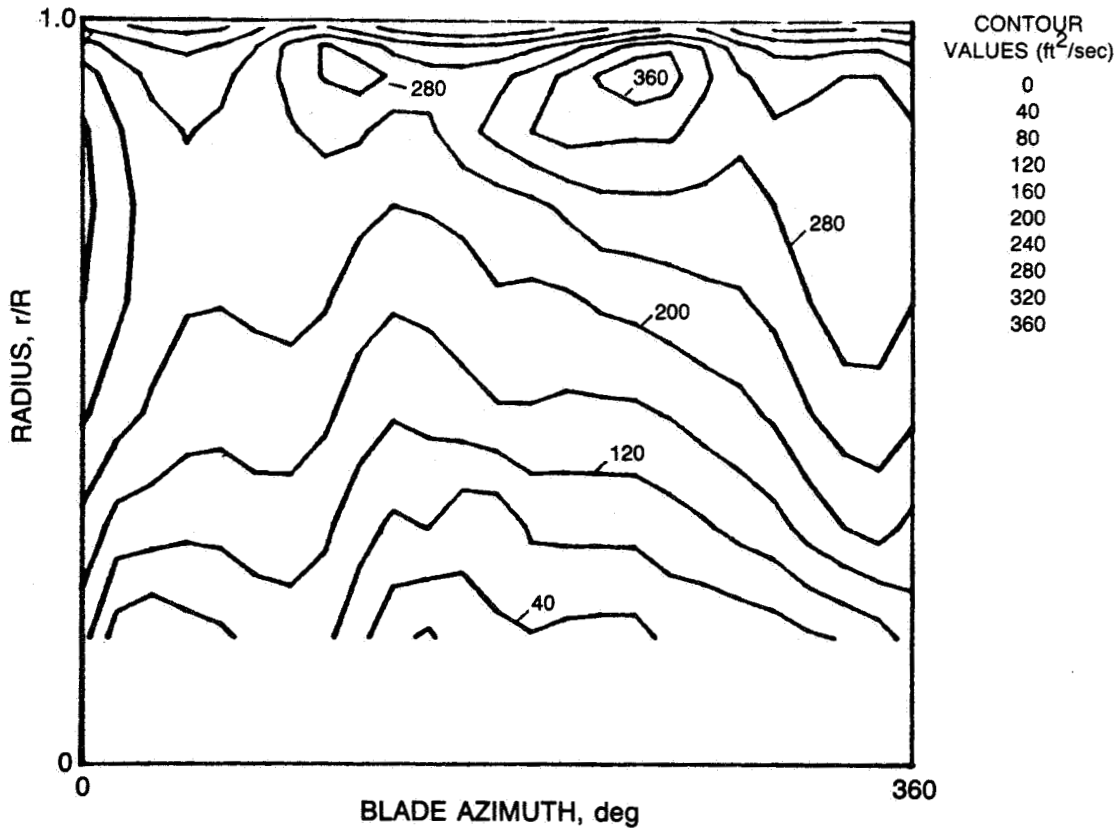

Figure 11. Rotor bound circulation, isolated fuselage influence.

87-11-47-11

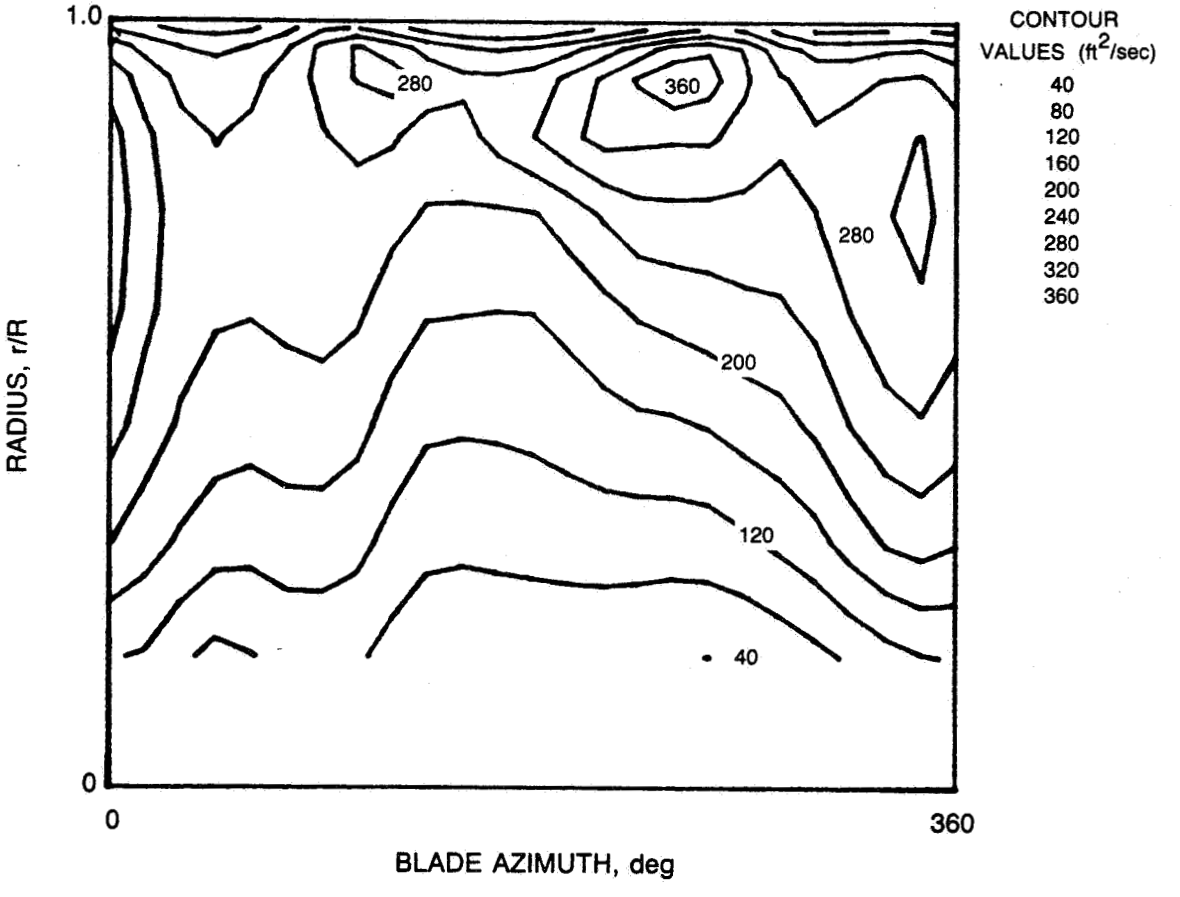

Figure 12. Rotor bound circulation, isolated rotor only.

87-11-47-12

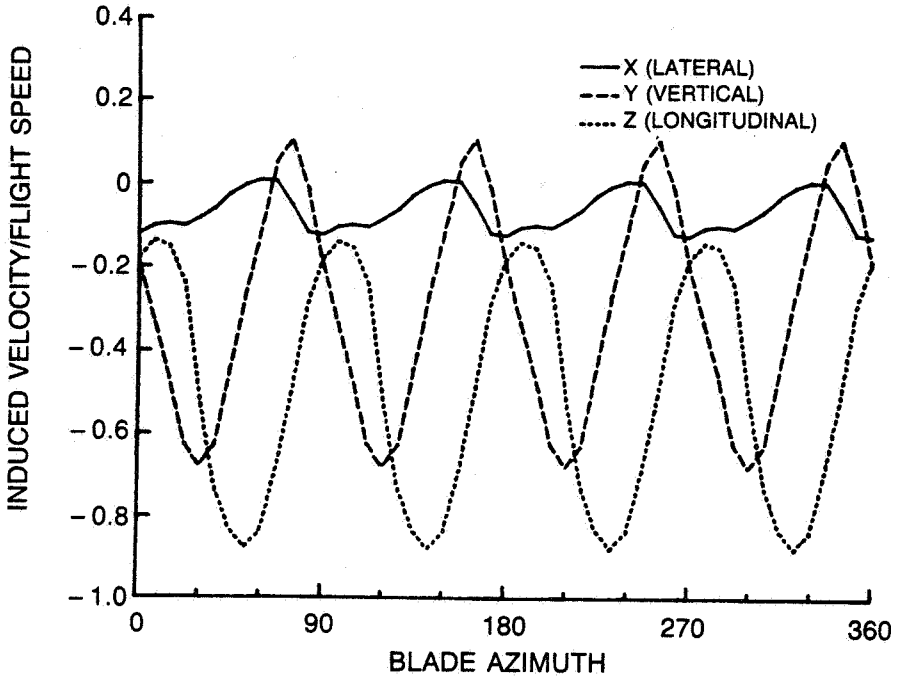

a) ROTOR-INDUCED VELOCITY

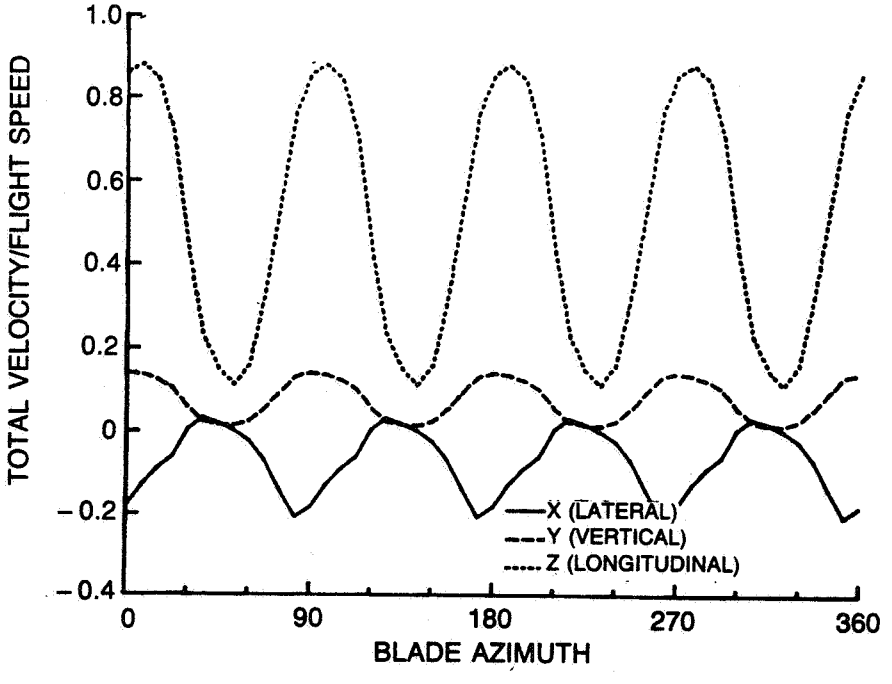

b) TOTAL VELOCITY

Figure 13. Velocity at fuselage panel 44.

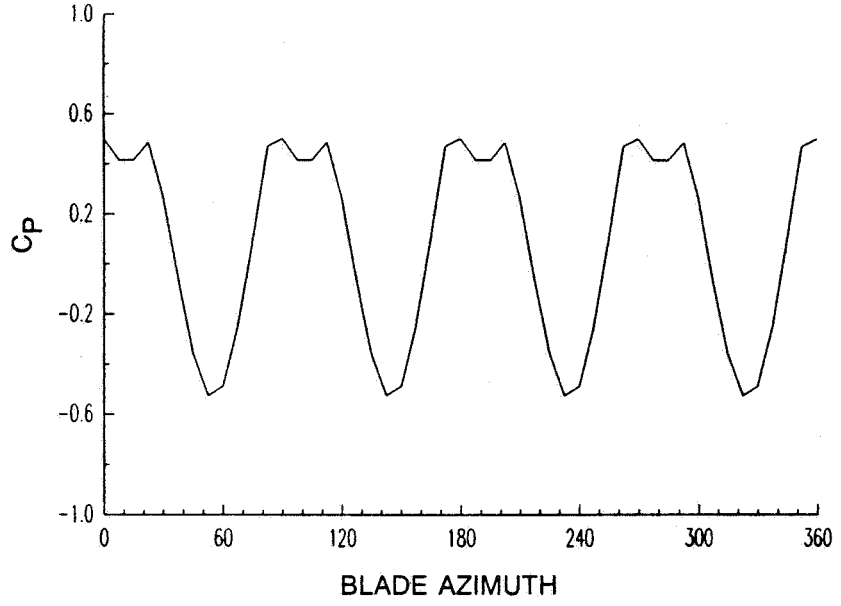

a) PRESSURE

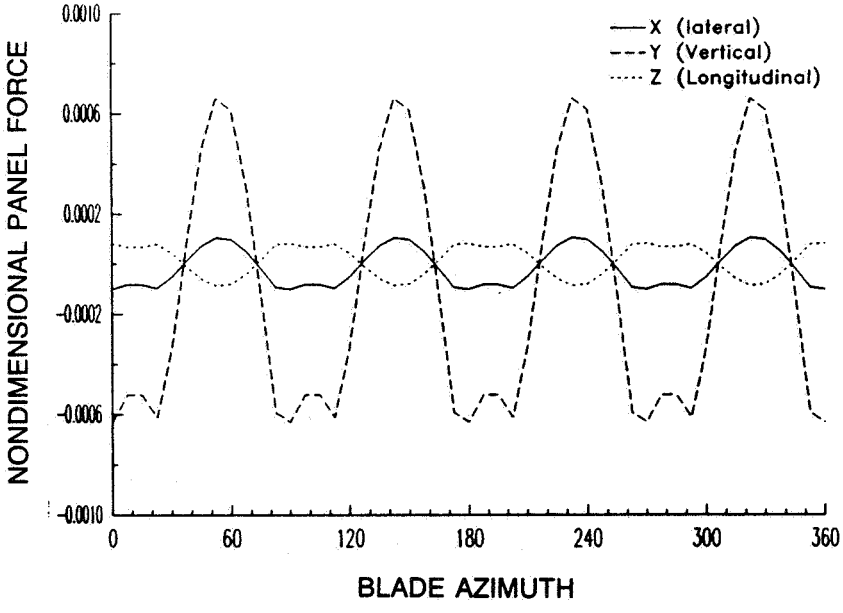

b) FORCE

Figure 14. Force and pressure at fuselage panel 44.

87-11-47-14

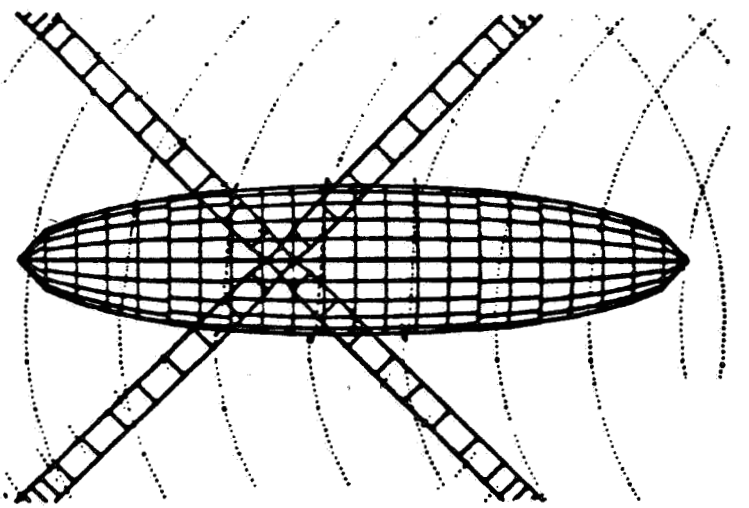

Figure 15. Top view of fuselage with tip filament spacing equal to three times panel size.

87-11-47-15

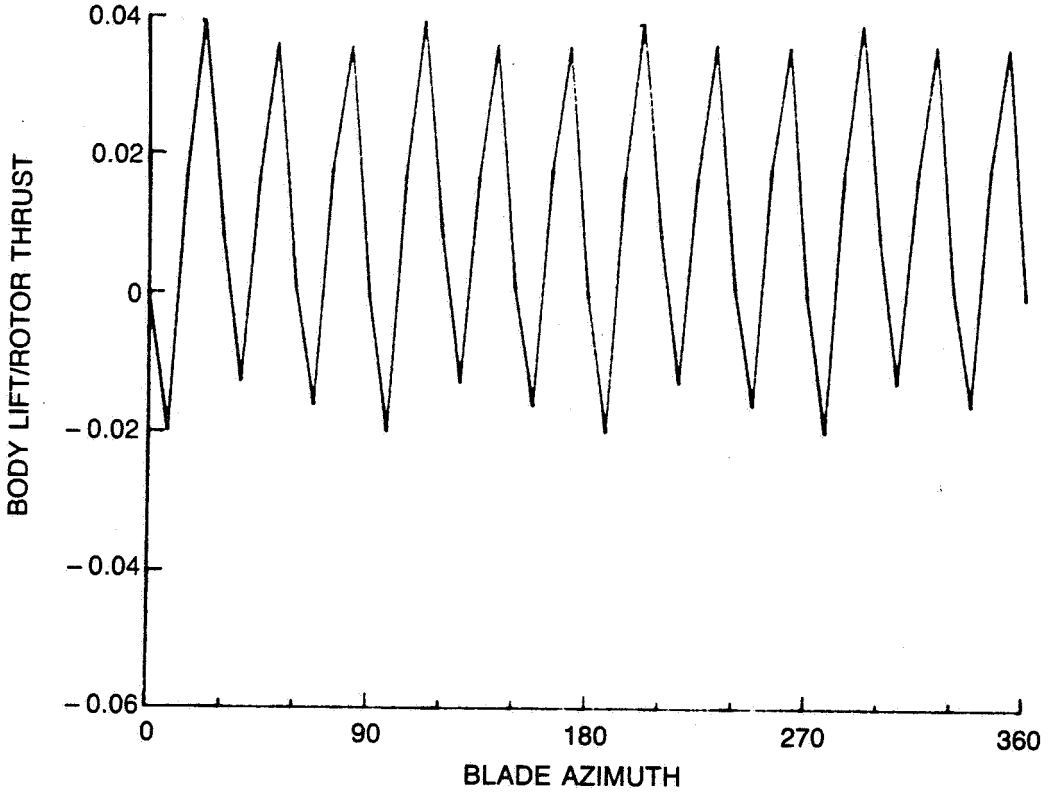

Figure 16. Quasi-steady fuselage lift without 5-point averaging, showing severe numerical resonance at $\mu = 0.15$, $C_T = 0.008$.

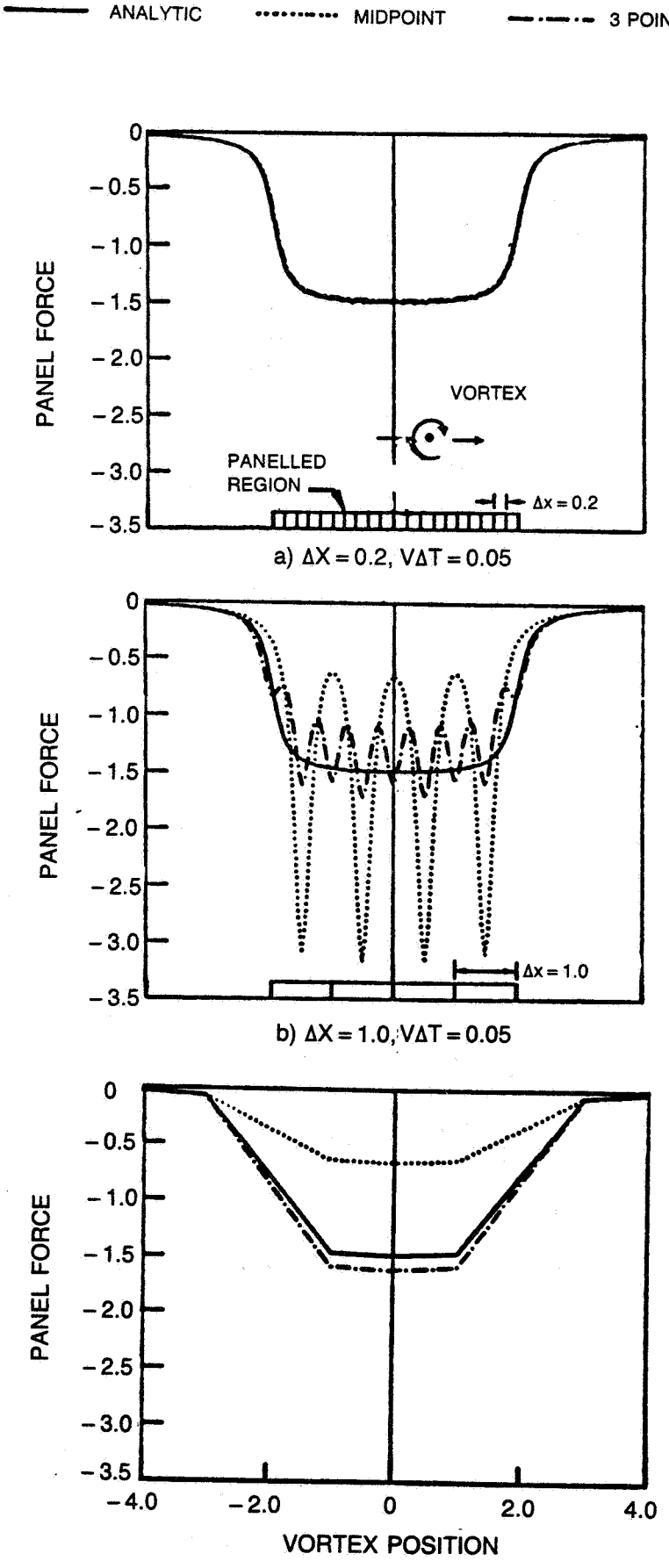

Figure 17. Vortex/flat plate model problem.

87-11-47-17

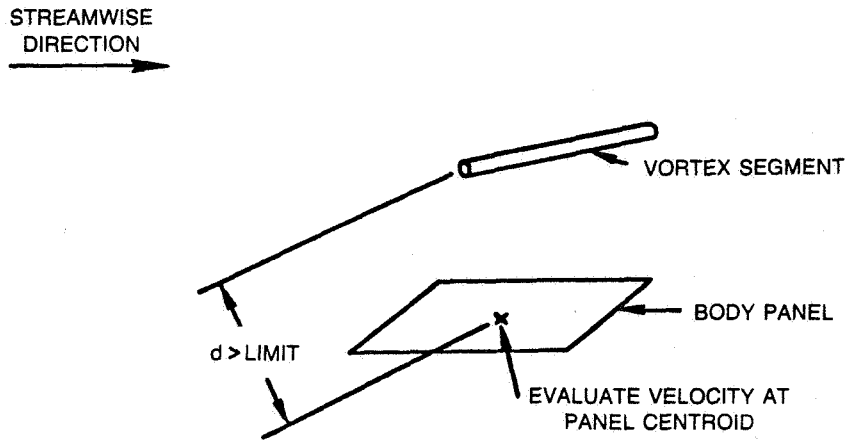

a) VORTEX SEGMENT FAR FROM BODY PANEL

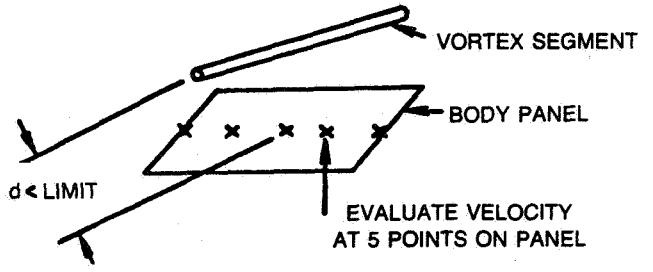

b) VORTEX SEGMENT CLOSE TO BODY PANEL

Figure 18. Vortex-panel velocity evaluation.

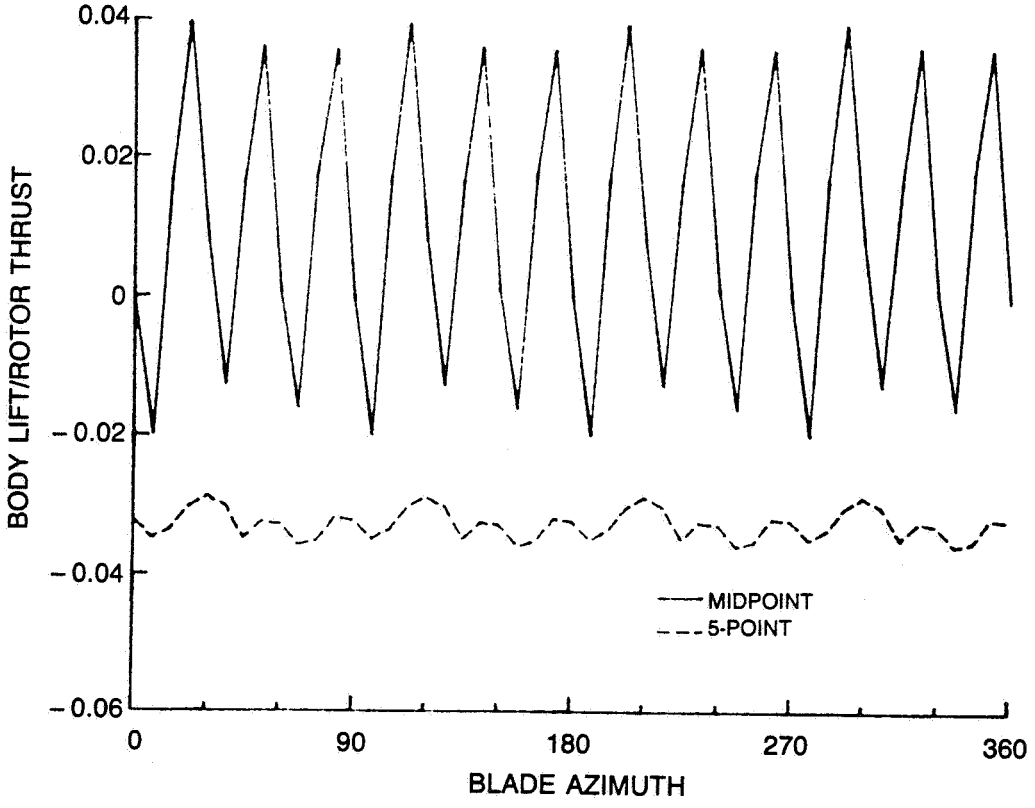

Figure 19. Quasi-steady fuselage lift with and without 5-point model, $\mu = 0.15$, $C_T = 0.008$.

87-11-47-19

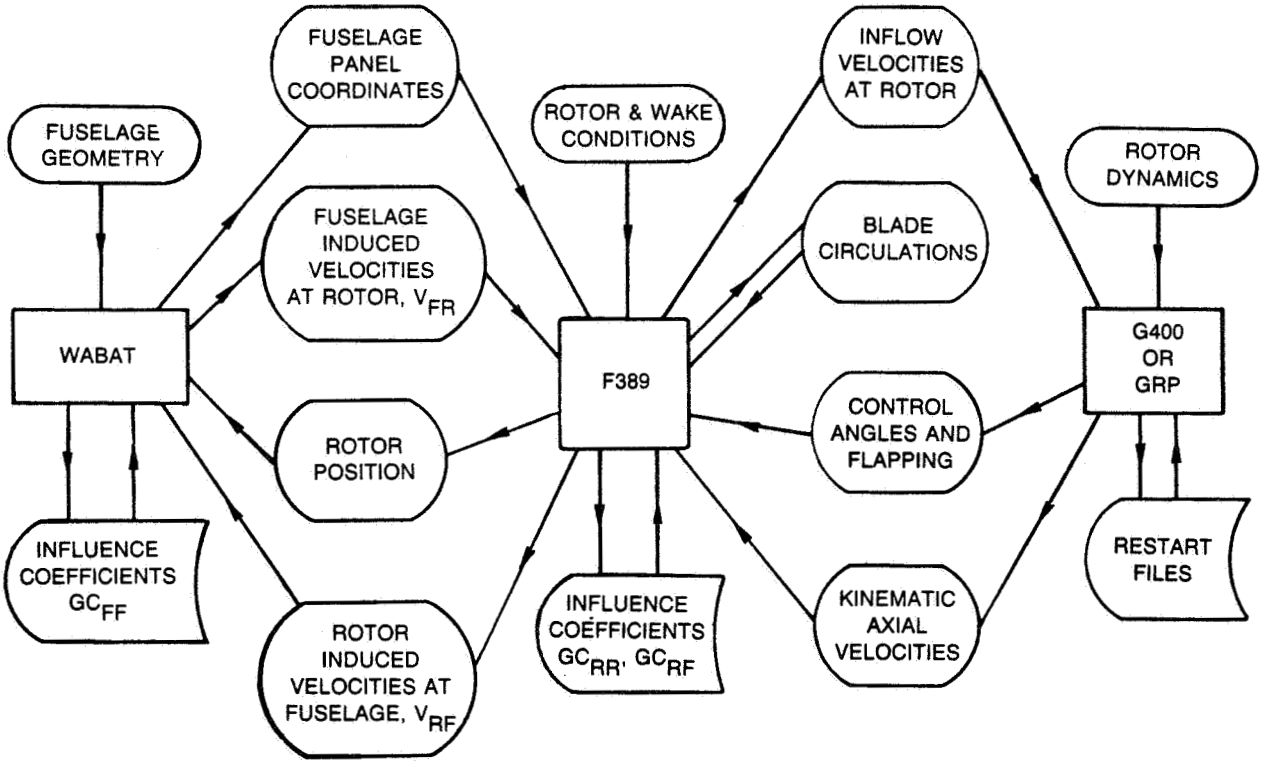

Figure 20. Coupling with blade response program.

87-11-47-20

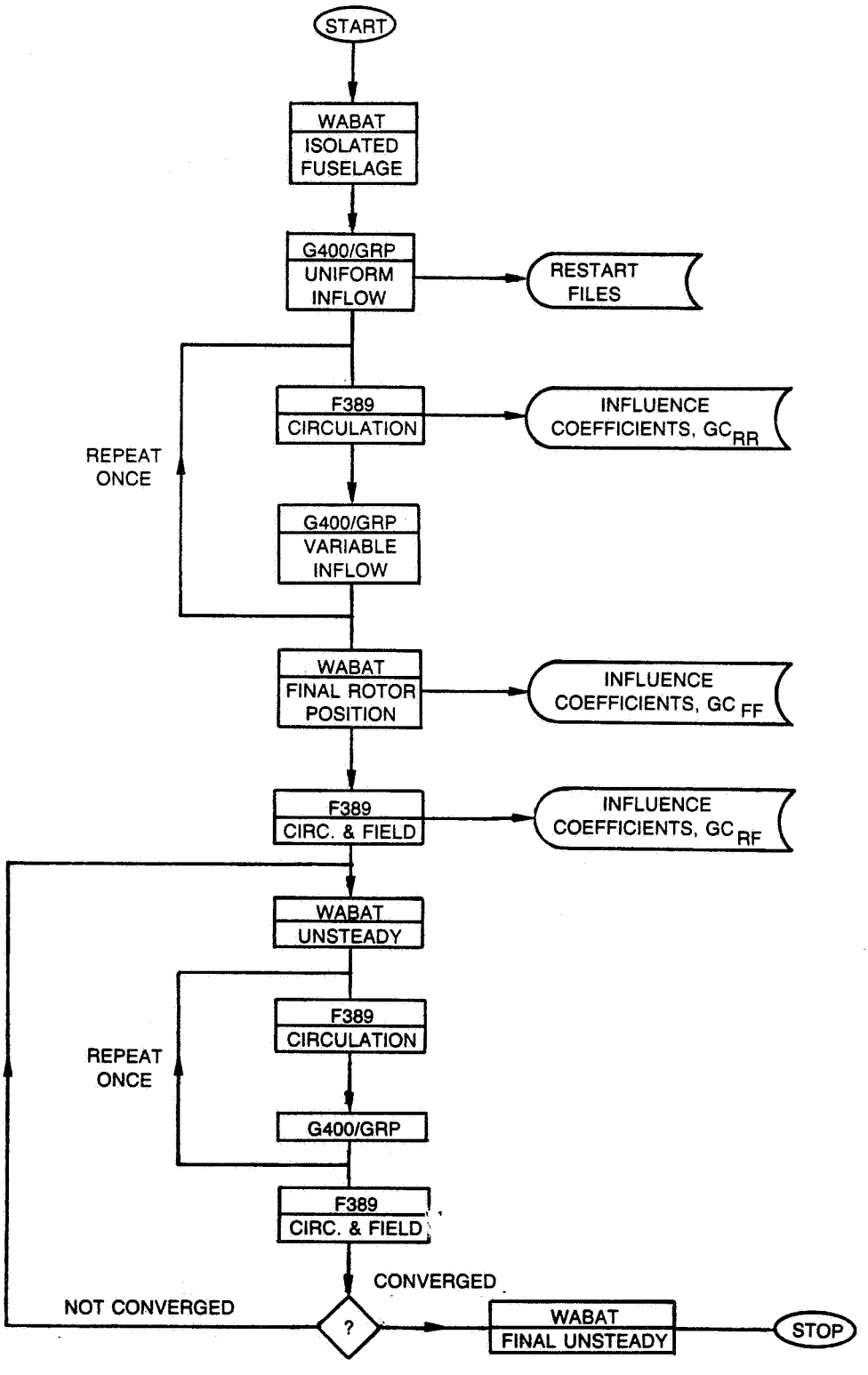

Figure 21. Calling sequence with blade response program.

87-11-47-21

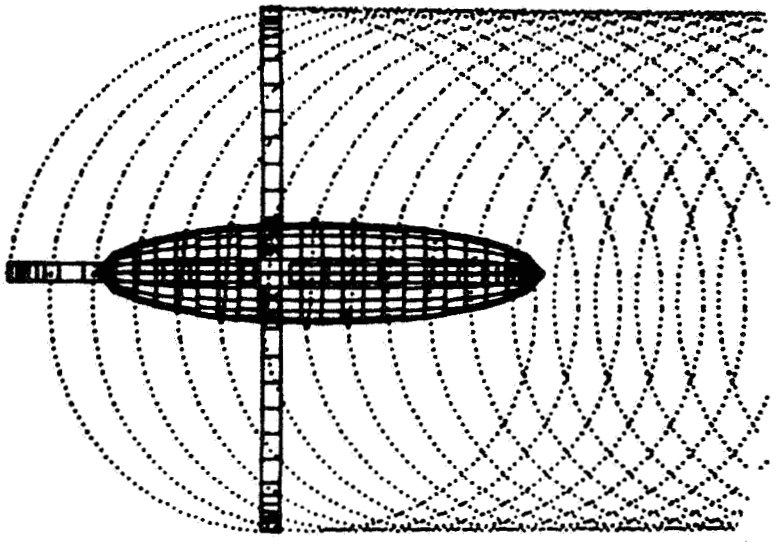

a) TOP VIEW

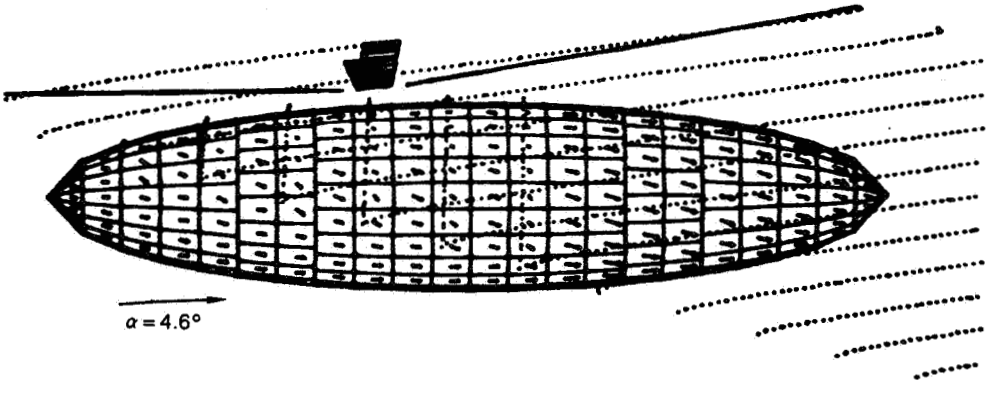

b) SIDE VIEW

Figure 22. Fuselage, rotor and wake geometry at $\mu = 0.10$ and $\psi = 0$.

87-11-47-22

c) REAR VIEW

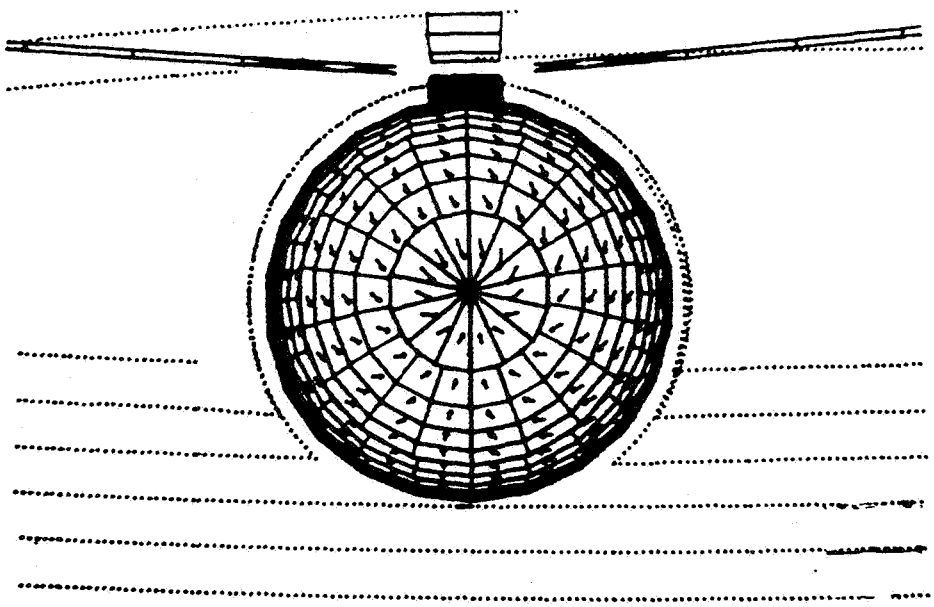

Figure 22. Fuselage, rotor and wake geometry at $\mu = 0.10$ and $\psi = 0$. (concluded)

87-11-47-48

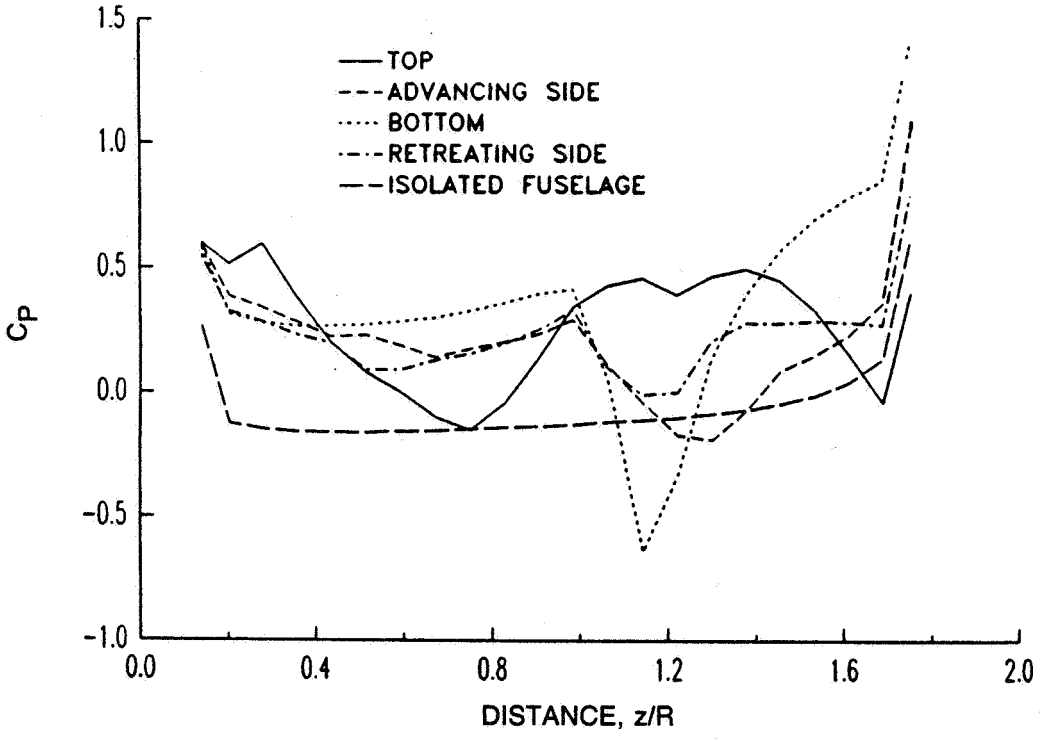

Figure 23. Mean pressure along fuselage, $\mu = 0.10$.

87-11-47-23

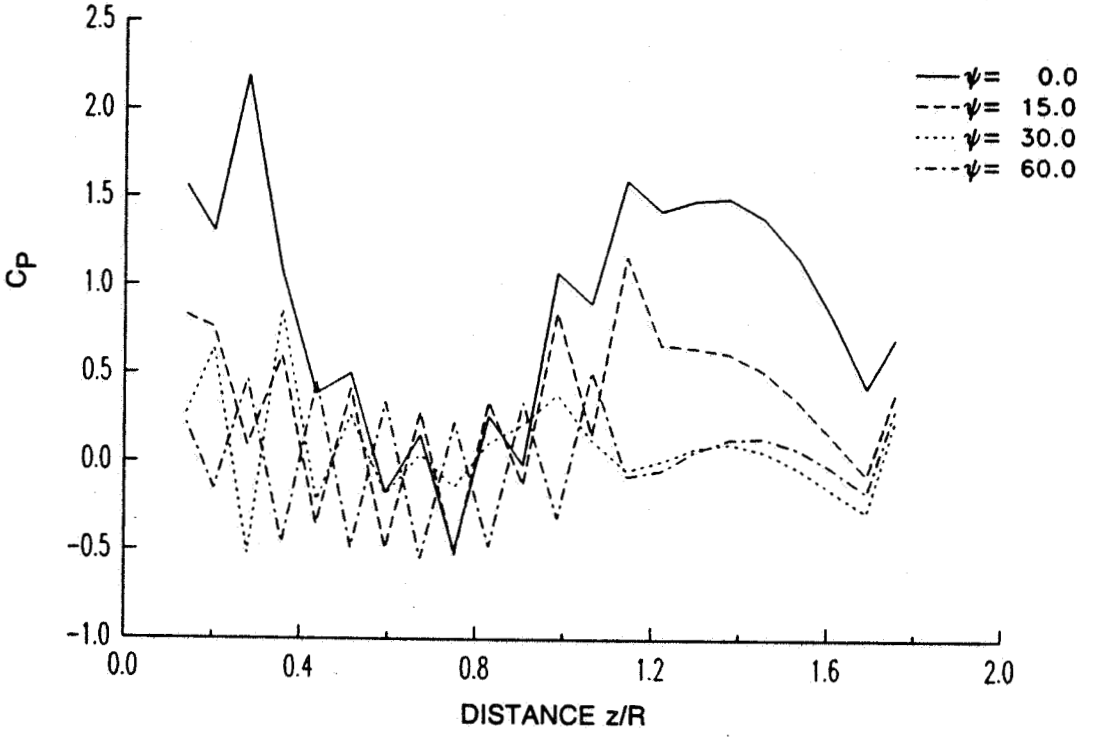

Figure 24. Pressure along top of fuselage, $\mu = 0.10$.

87-11-47-24

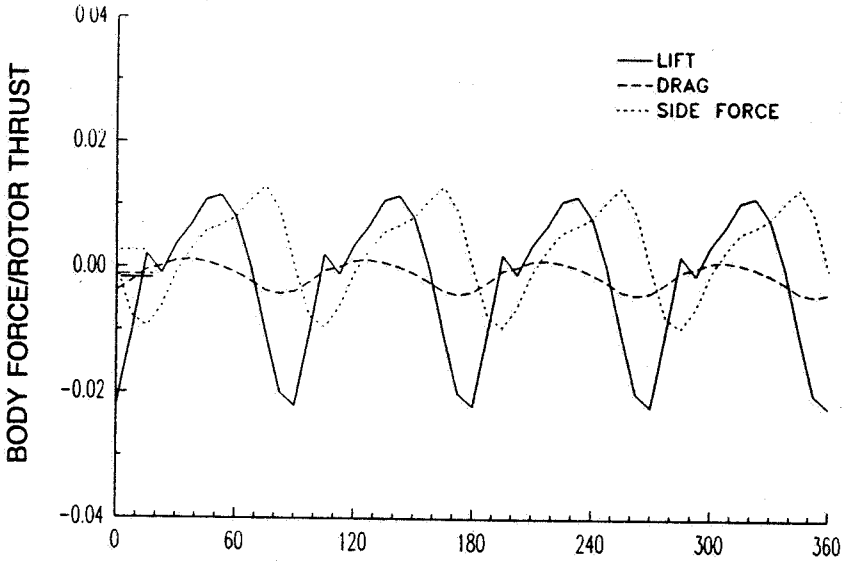

a) AIRLOADS

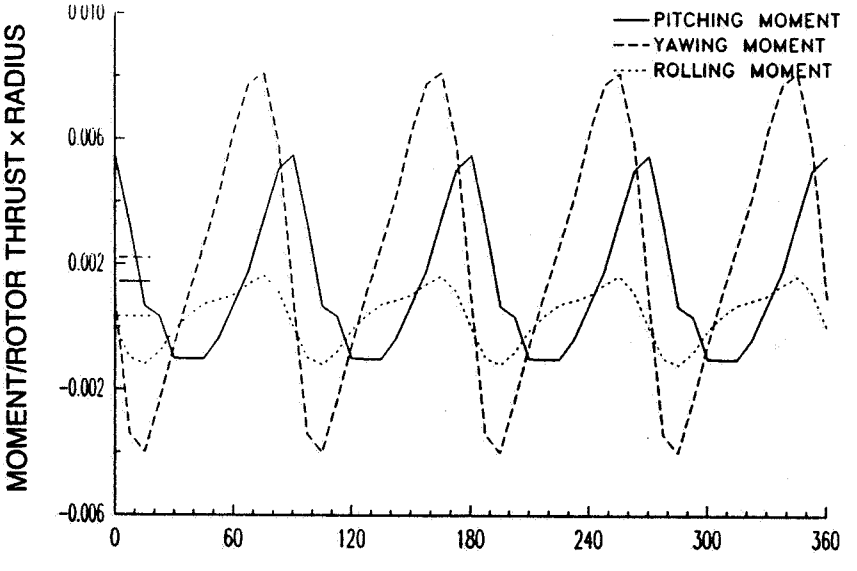

b) MOMENTS

Figure 25. Aerodynamic forces and moments on the fuselage at $\mu = 0.10$, $C_T = 0.0078$.

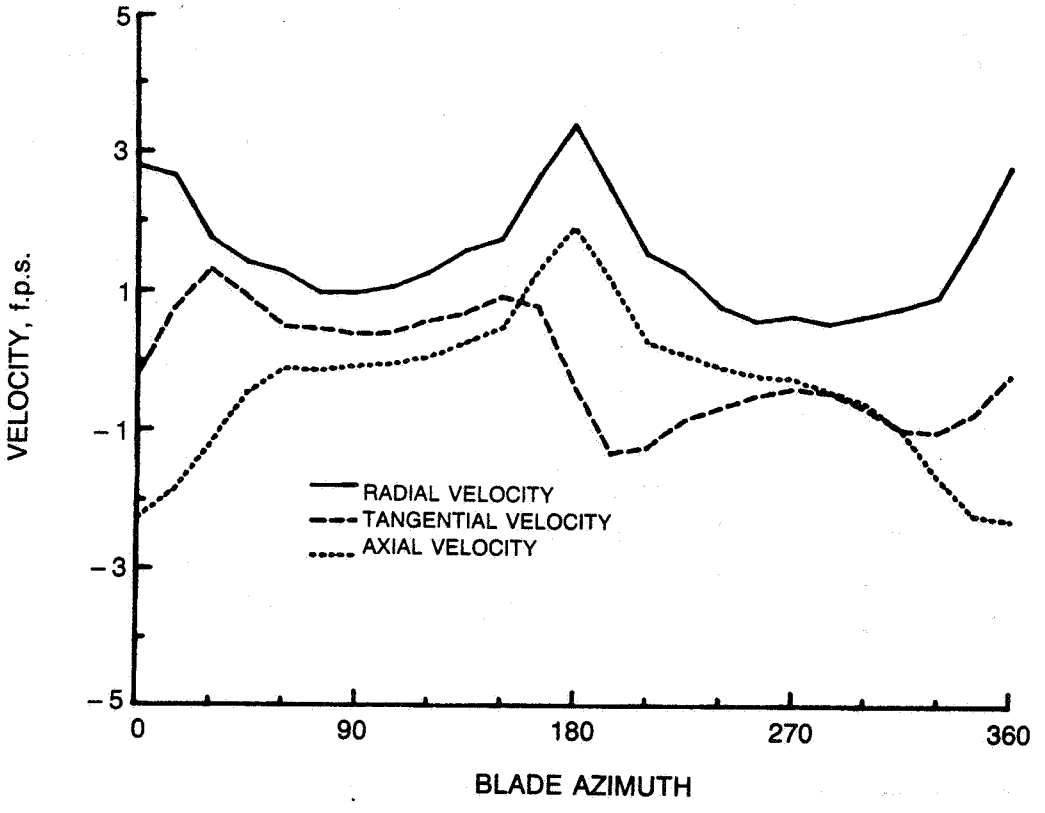

Figure 26. Fuselage-induced velocities at rotor, r/R = 0.75, $\mu = 0.10$, converged solution.

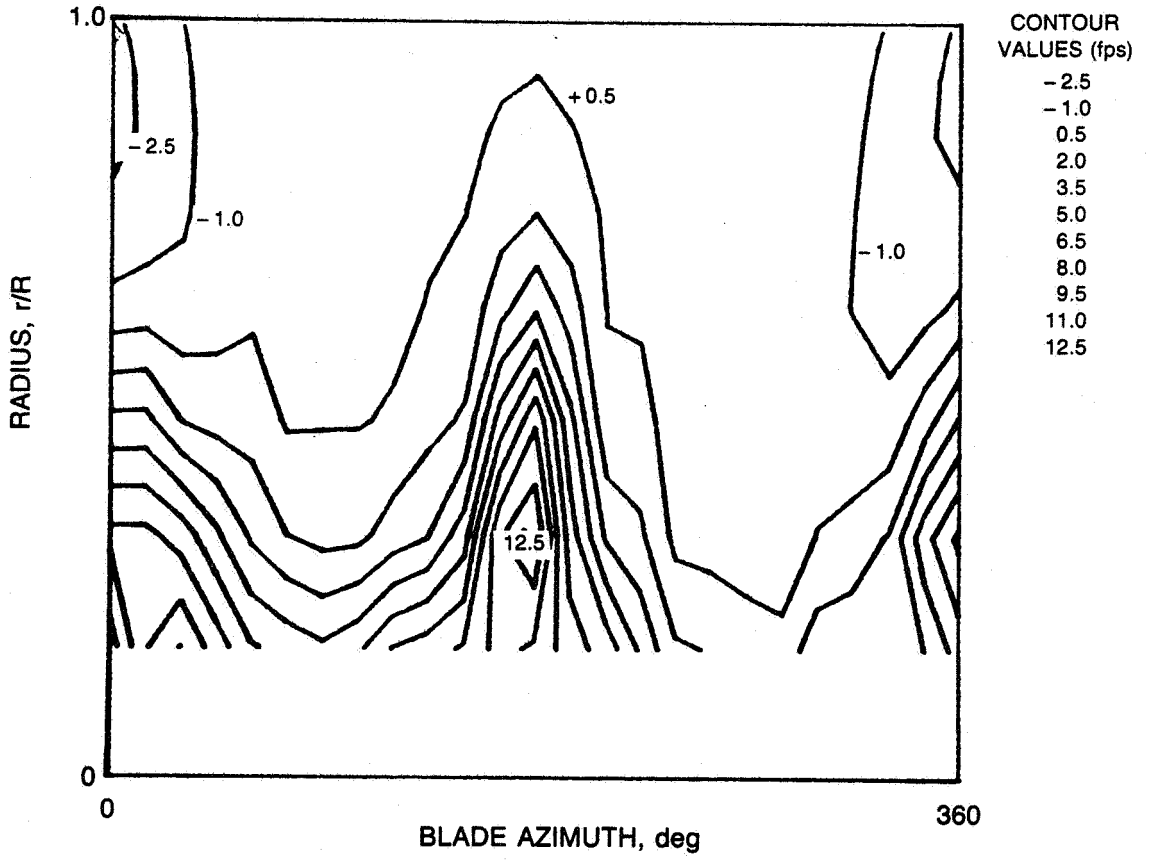

Figure 27. Fuselage-induced axial velocity at rotor-converged solution at $\mu = 0.10$

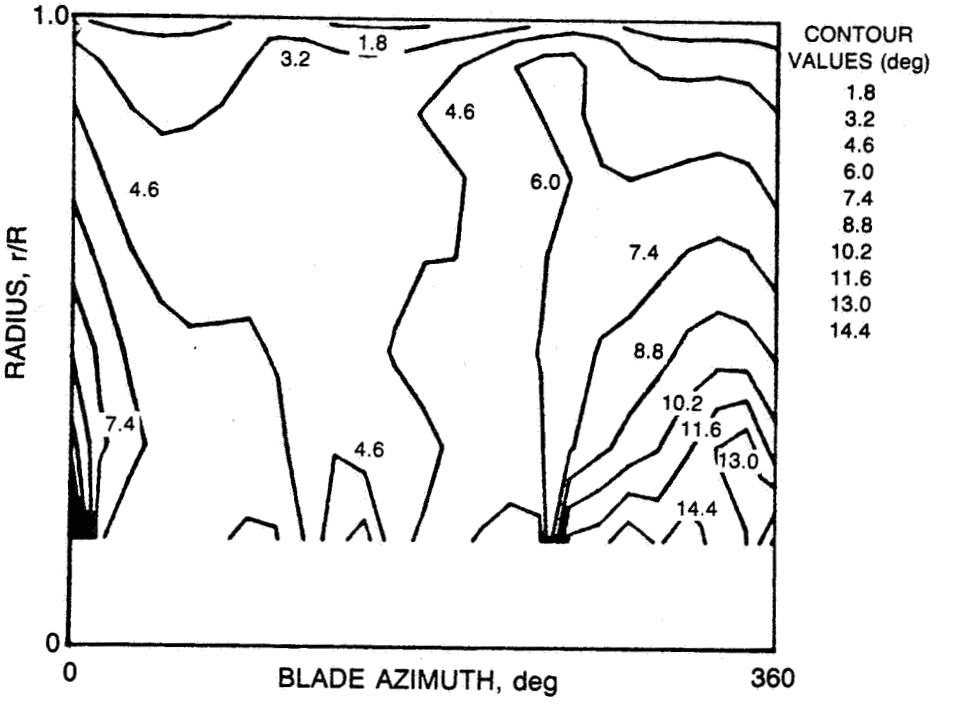

a) CONVERGED SOLUTION

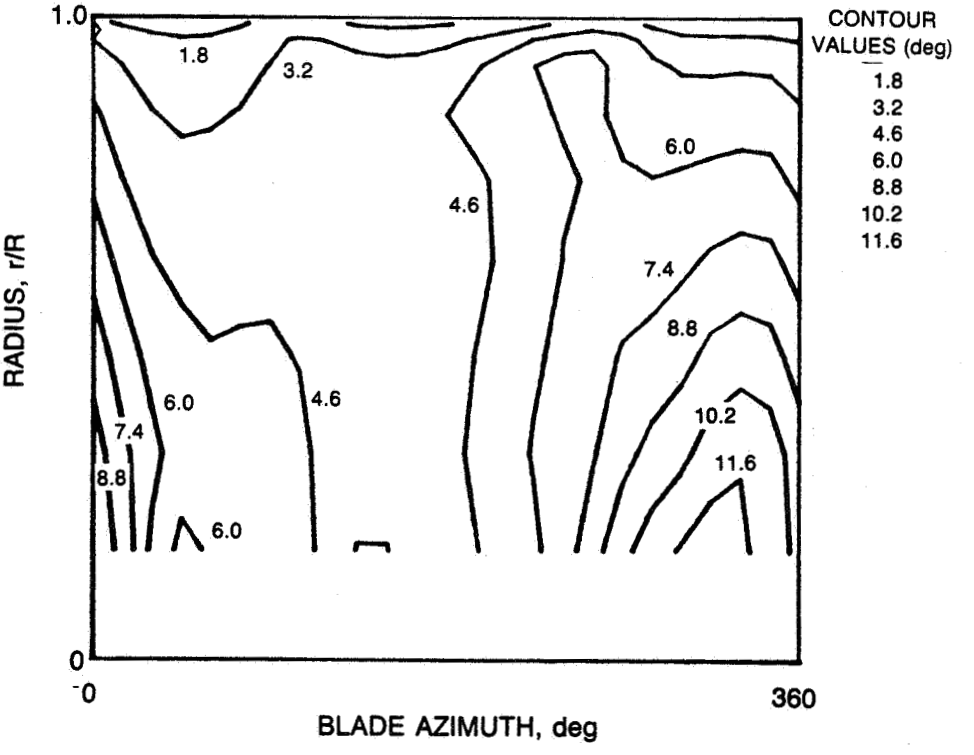

b) ISOLATED ROTOR

Figure 28. Blade angle of attack at $\mu = 0.10$

87-11-47-28

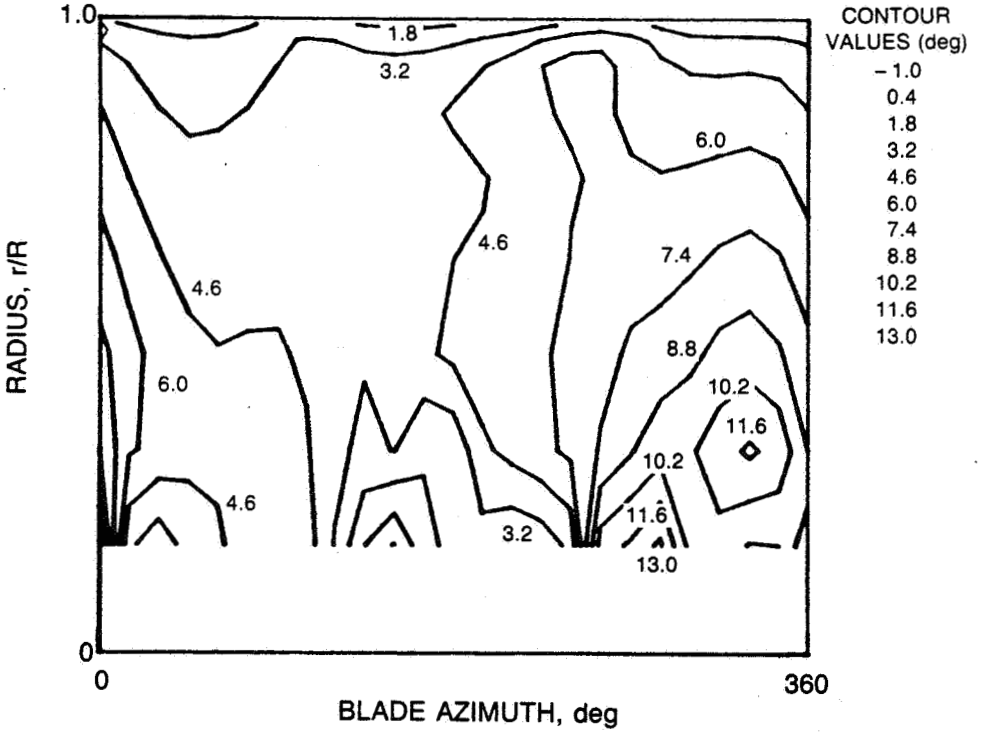

c) ROTOR WITH INFLUENCE OF ISOLATED FUSELAGE

Figure 28. Blade angle of attack at $\mu = 0.10$. (concluded)

87-11-47-29

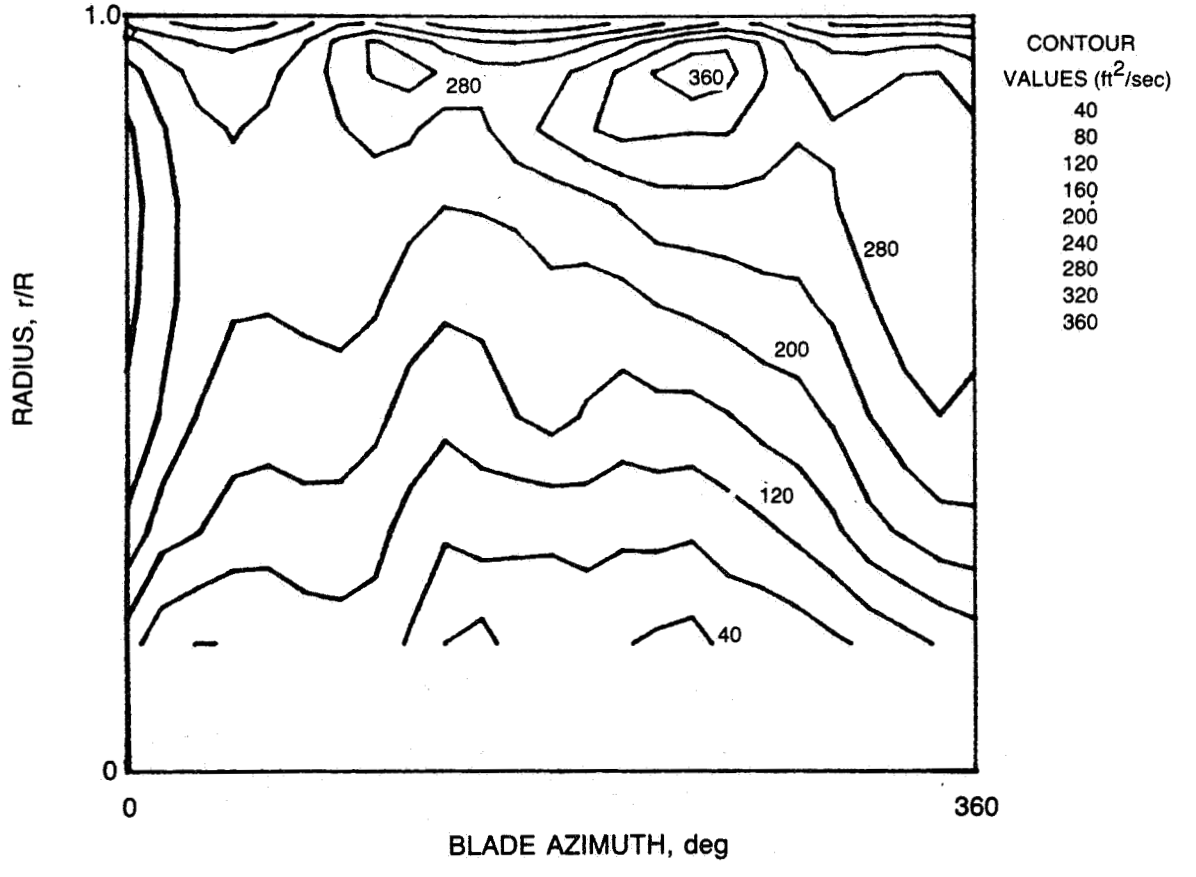

Figure 29. Blade bound circulation — converged solution at $\mu = 0.10$.

87-11-47-30

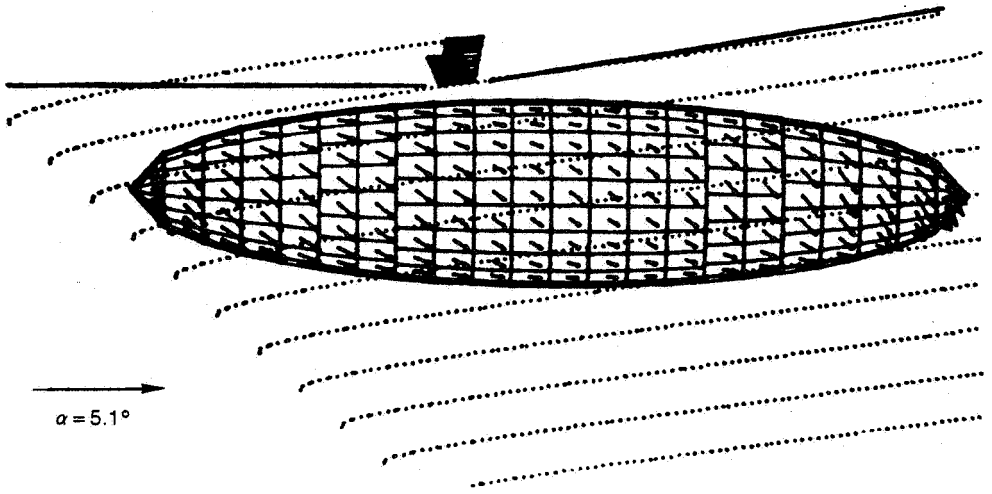

a) $\mu = 0.05$

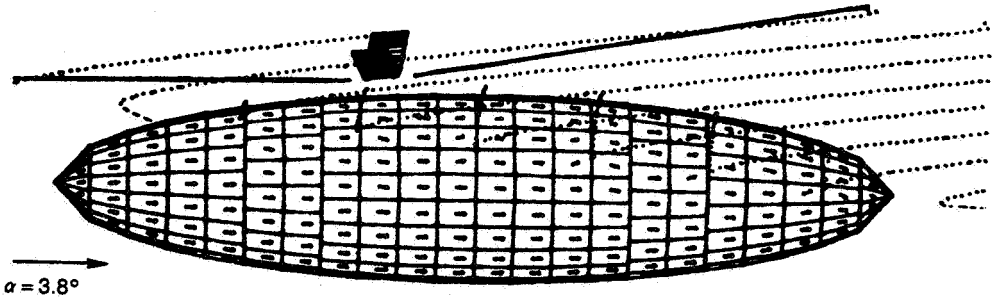

b) $\mu = 0.15$

Figure 30. Retreating side view of rotor, fuselage and wake.

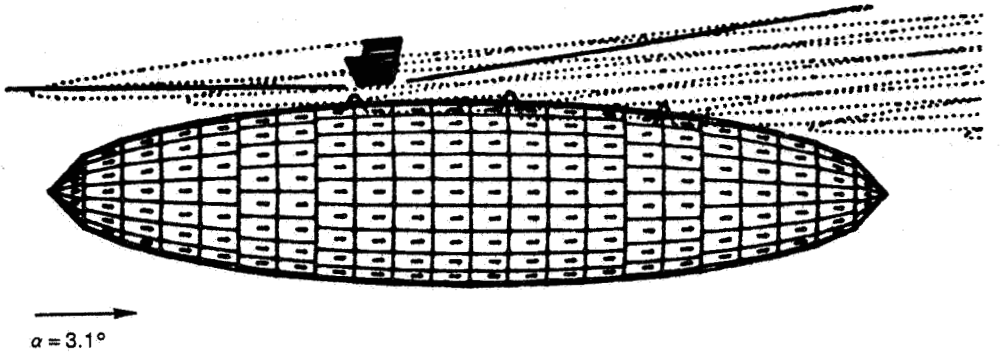

c) $\mu = 0.20$

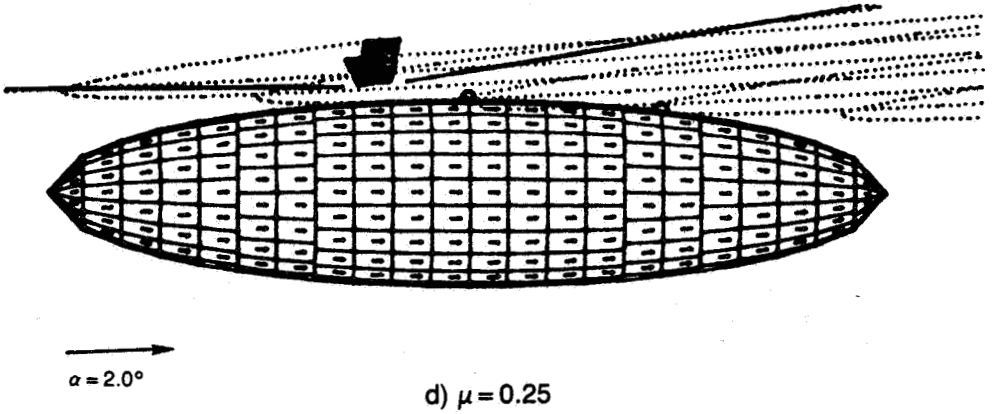

d) $\mu = 0.25$

Figure 30. Retreating side view of rotor, fuselage and wake. (continued)

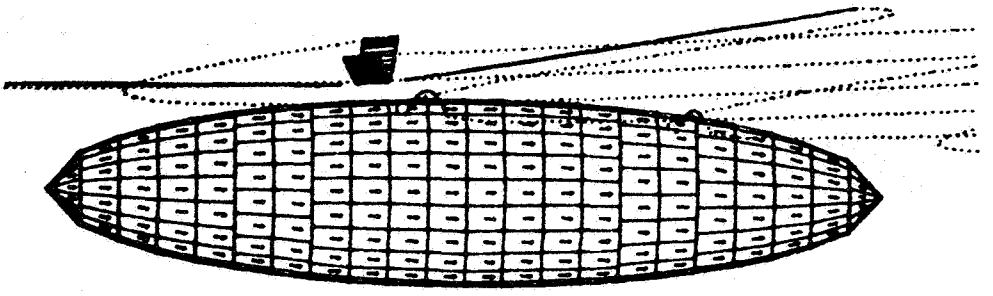

$\alpha = -1.1°$

e) $\mu = 0.35$

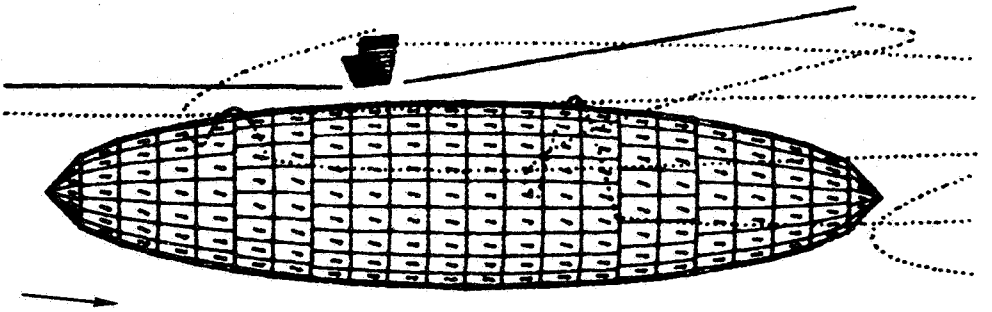

$\alpha = -7.4°$

f) $\mu = 0.45$

Figure 30. Retreating side view of rotor, fuselage and wake. (concluded)

87-11-47-33

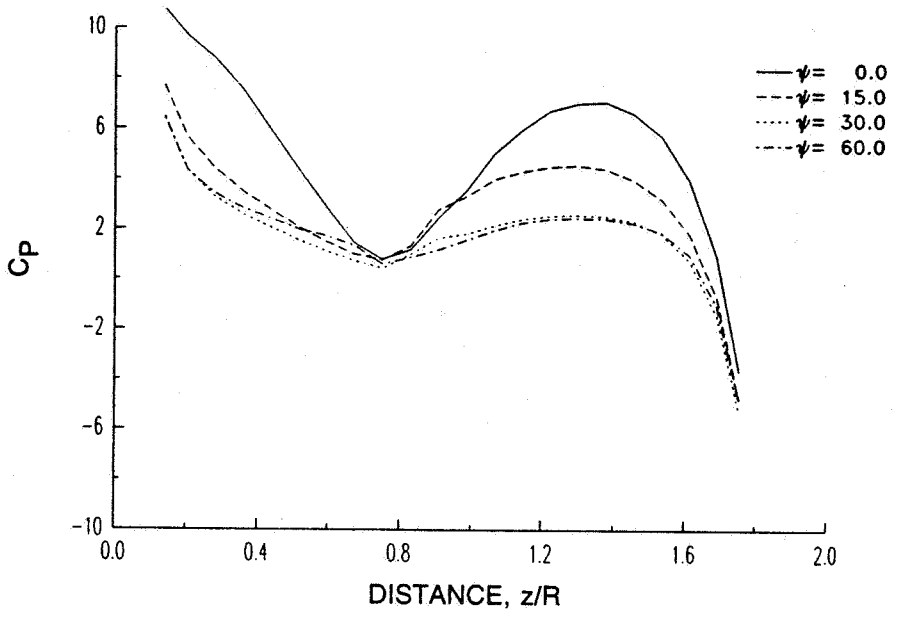

a) $\mu = 0.05$

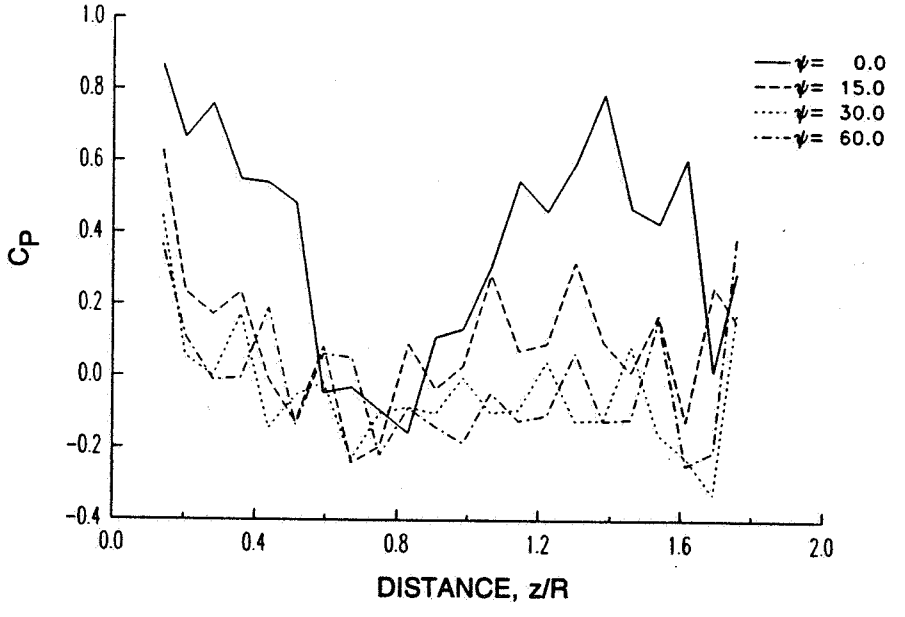

b) $\mu = 0.150$

Figure 31. Pressures along the top of the fuselage.

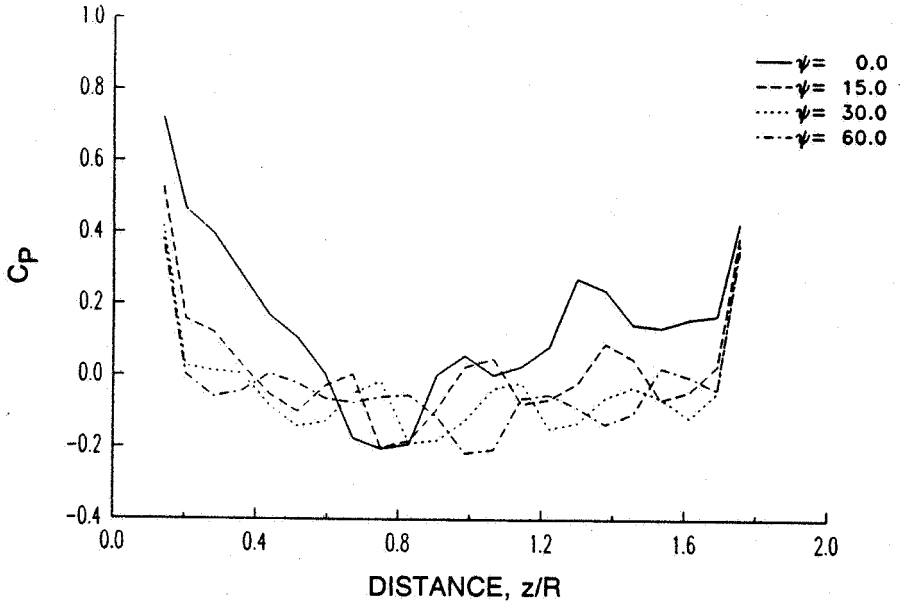

c) $\mu = 0.250$

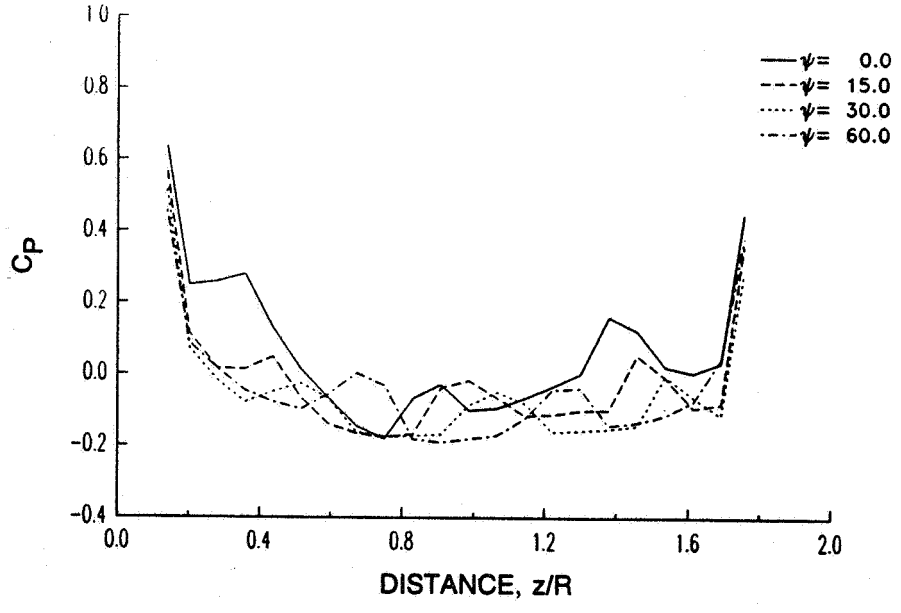

d) $\mu = 0.350$

Figure 31. Pressures along the top of the fuselage. (concluded)

87-11-47-35

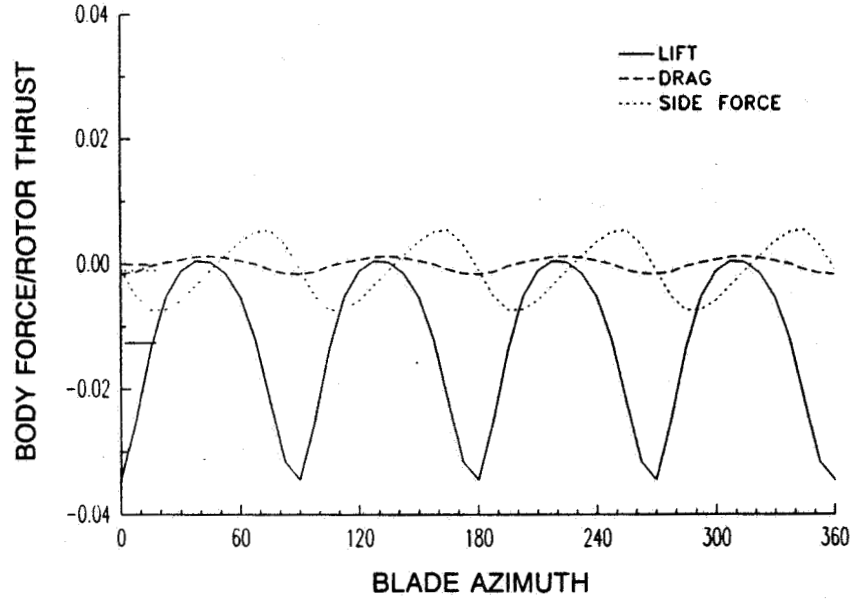

a) $\mu = 0.05$, $C_T = 0.0079$

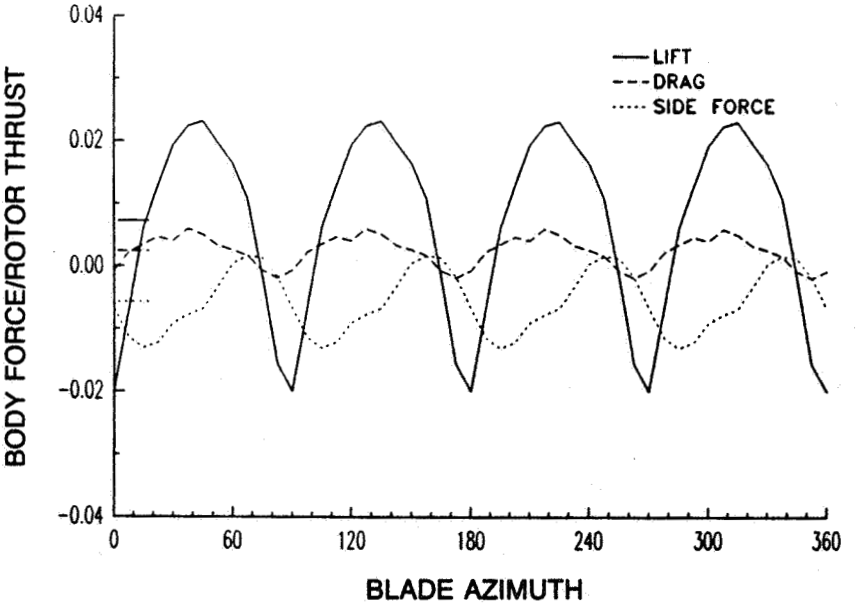

b) $\mu = 0.15$, $C_T = 0.0079$

Figure 32. Fuselage airloads at several advance ratios.

87-11-47-36

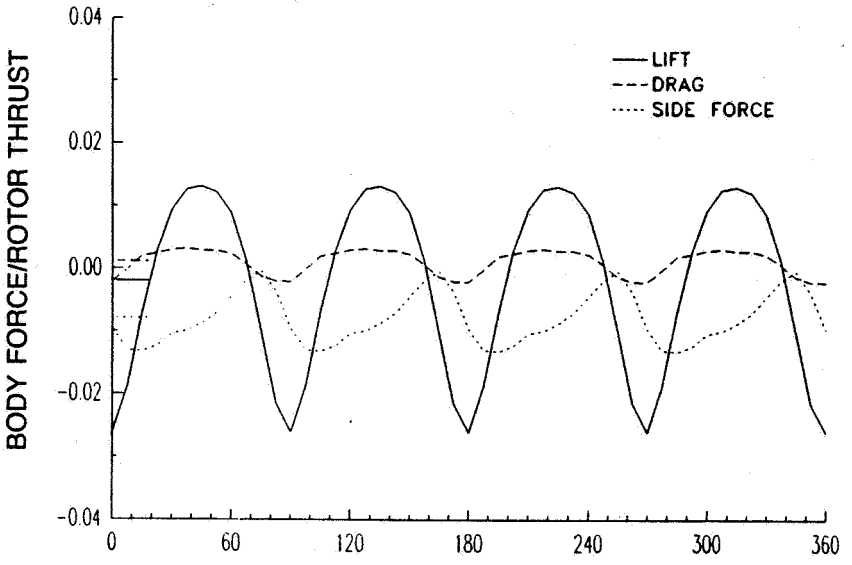

c) $\mu = 0.20$, $C_T = 0.0079$

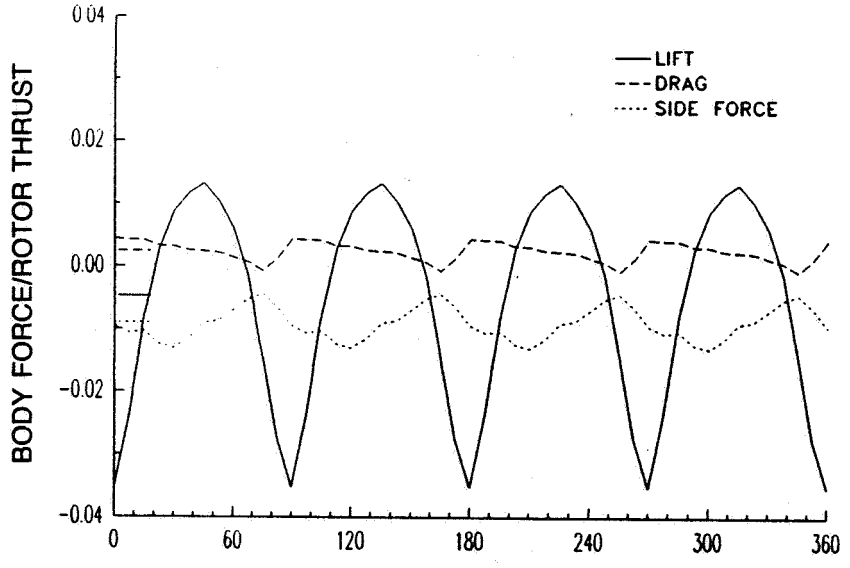

d) $\mu = 0.25$, $C_T = 0.0078$

Figure 32. Fuselage airloads at several advance ratios. (continued)

87-11-47-37

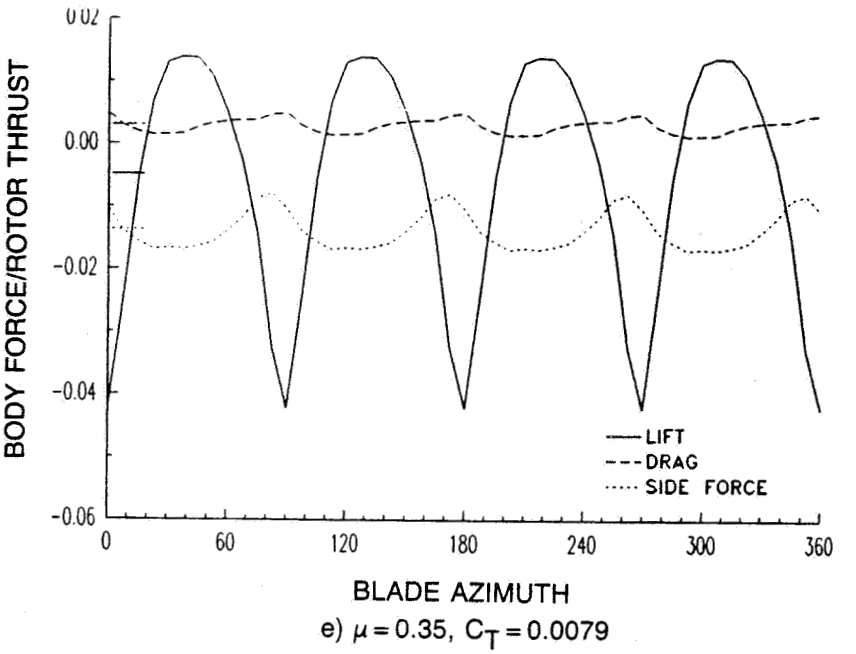

e) $\mu = 0.35$, $C_T = 0.0079$

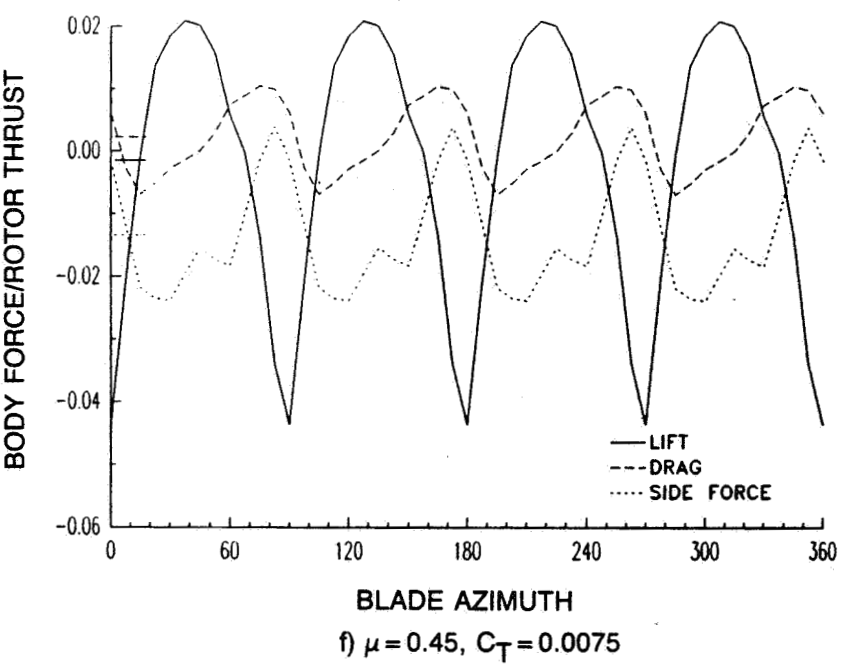

f) $\mu = 0.45$, $C_T = 0.0075$

Figure 32. Fuselage airloads at several advance ratios. (concluded)

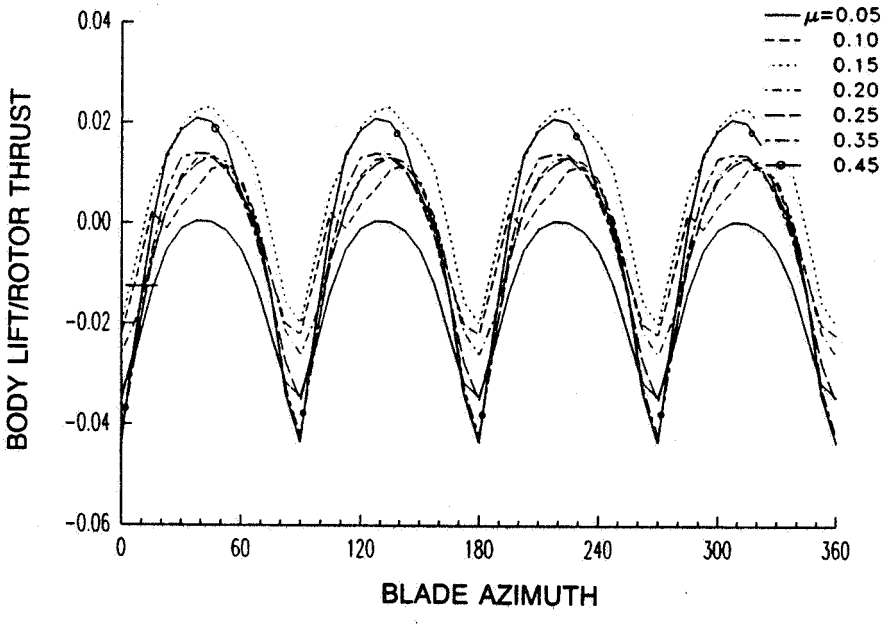

Figure 33. Fuselage lift at several advance ratios.

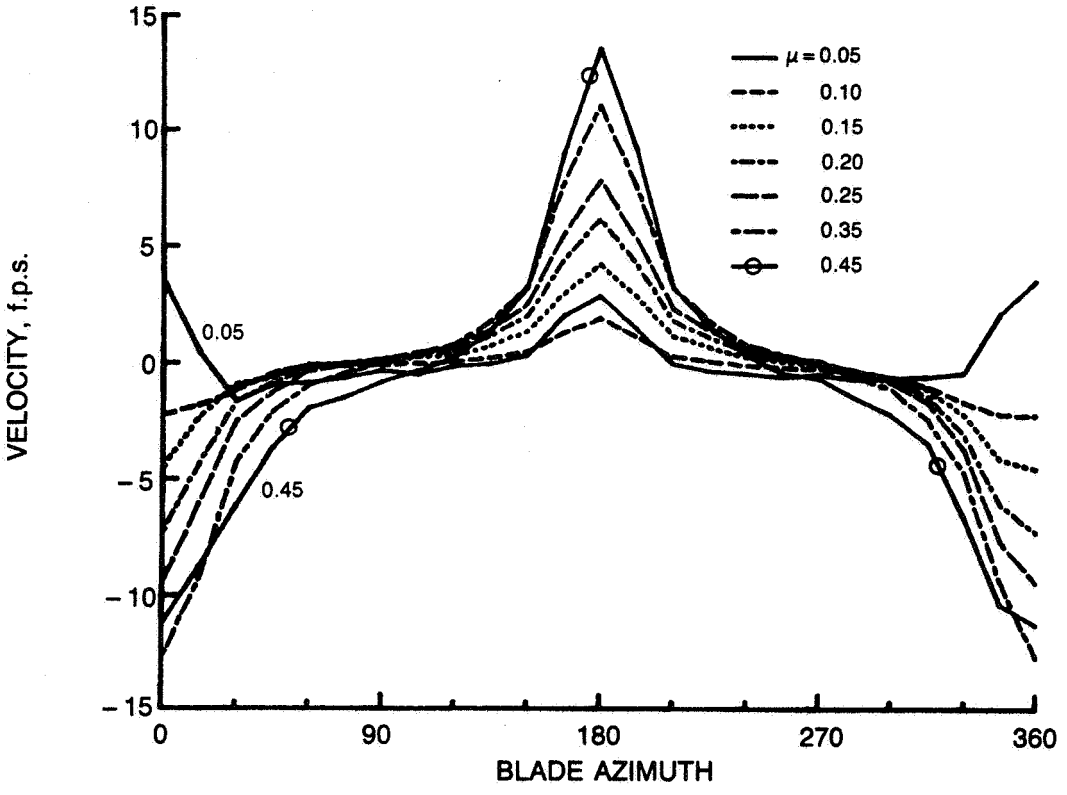

Figure 34. Fuselage-induced axial velocity at r/R = 0.75.

87-11-47-40

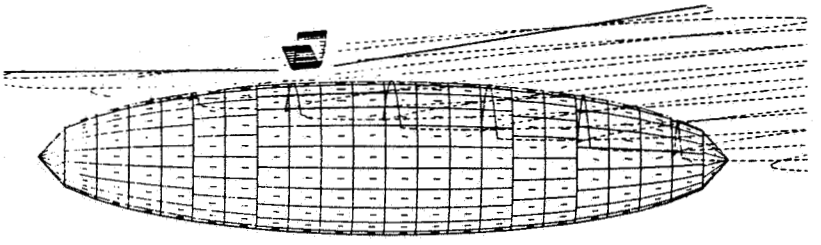

a) SIDE VIEW — 0.02 RADII OFFSET

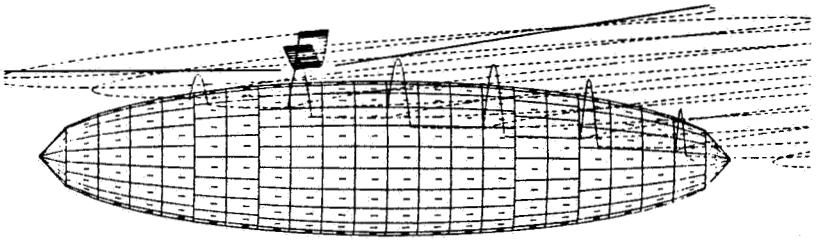

b) SIDEVIEW — 0.30 RADII OFFSET

Figure 35. Effect of filament offset distance.

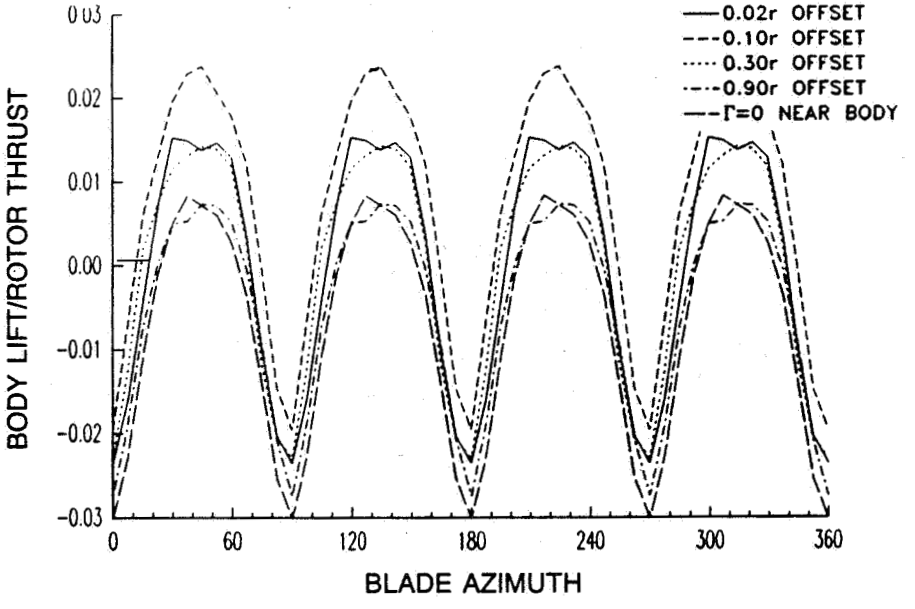

c) BODY LIFT COMPARISON AT $\mu = 0.15$, $C_T = 0.0079$

Figure 35. Effect of filament offset distance. (concluded)

87-11-47-42

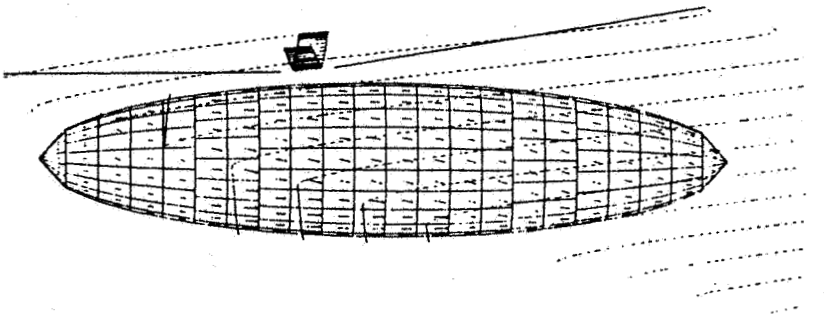

a) SPLIT AT 0°

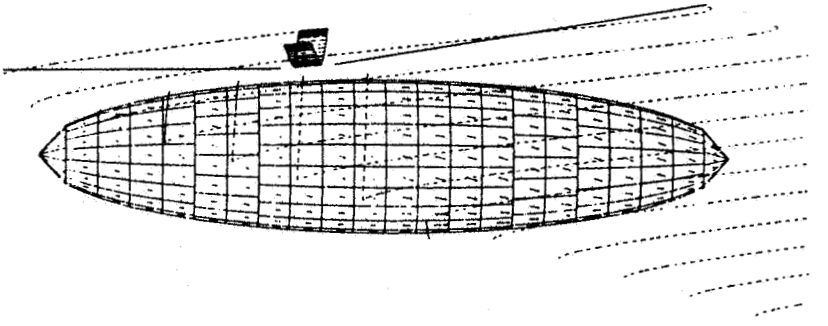

b) SPLIT AT −45°

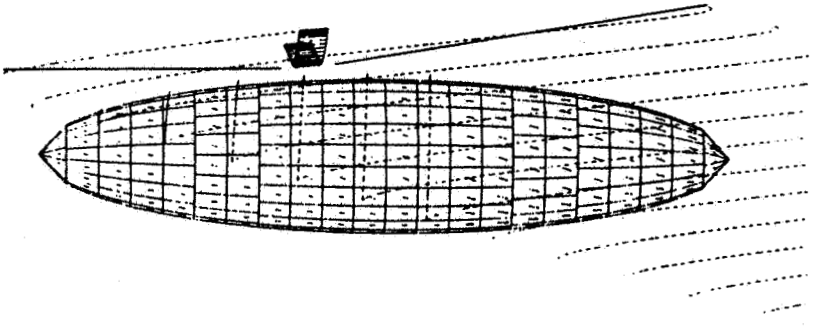

c) ALL FILAMENTS SHIFTED UP

Figure 36. Front view of a fuselage and wake filaments, showing effect of varying split angle.

87-11-47-43

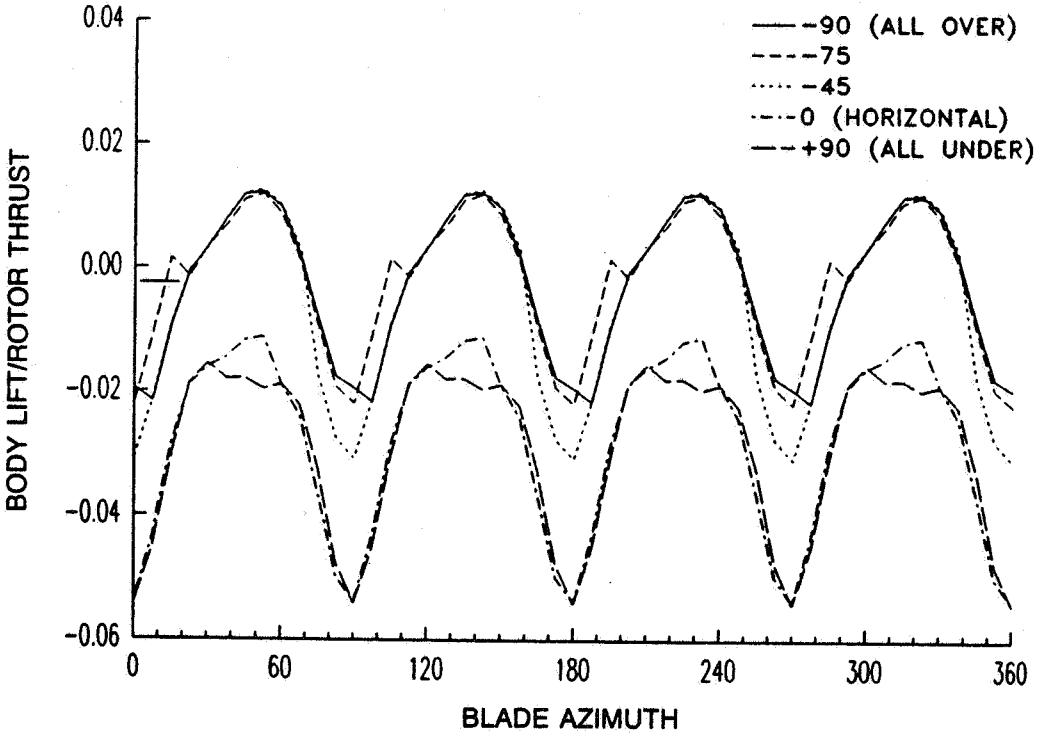

Figure 37. Effect of wake filament split angle, $\mu = 0.10$, $C_T = 0.0079$.

87-11-47-44

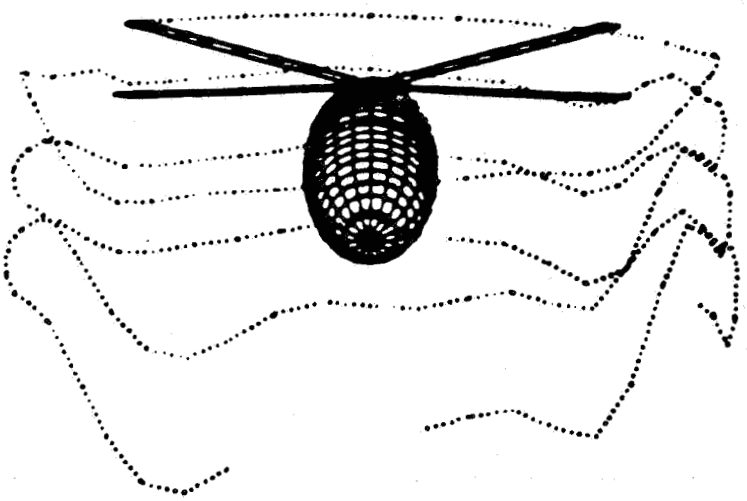

Figure 38. Generalized wake tip filament at $\mu = 0.10$.

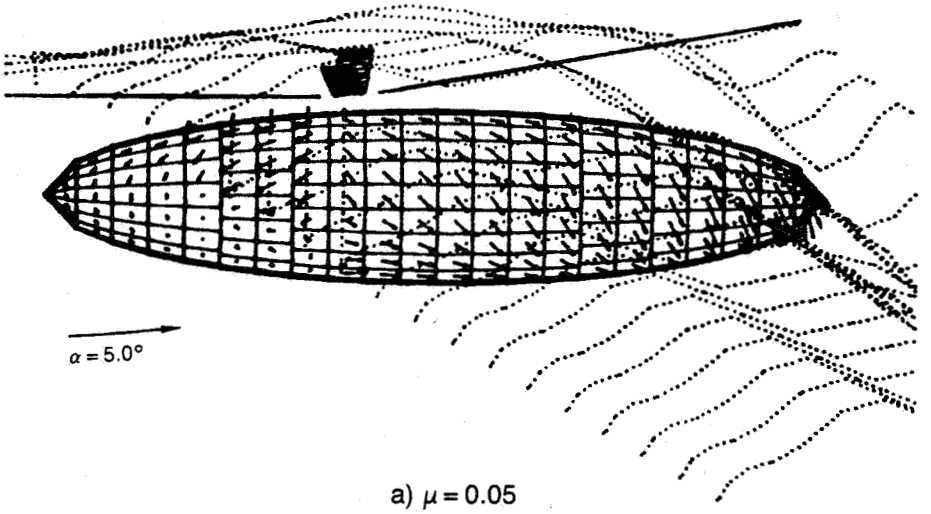

a) $\mu = 0.05$

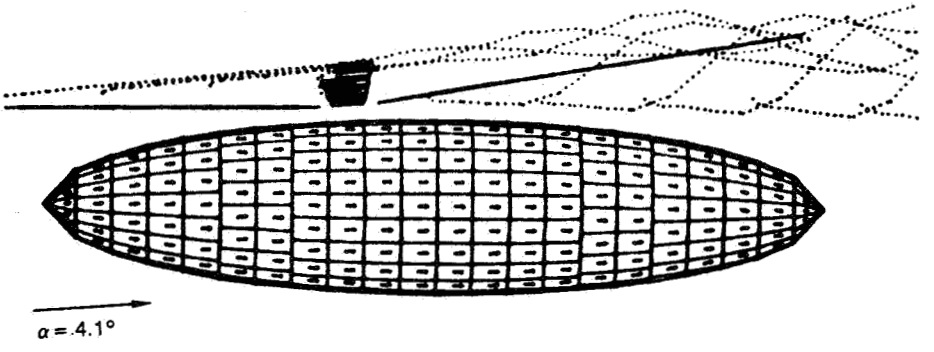

b) $\mu = 0.15$

Figure 39. Side view of fuselage, generalized wake tip filaments, and surface velocity vectors.

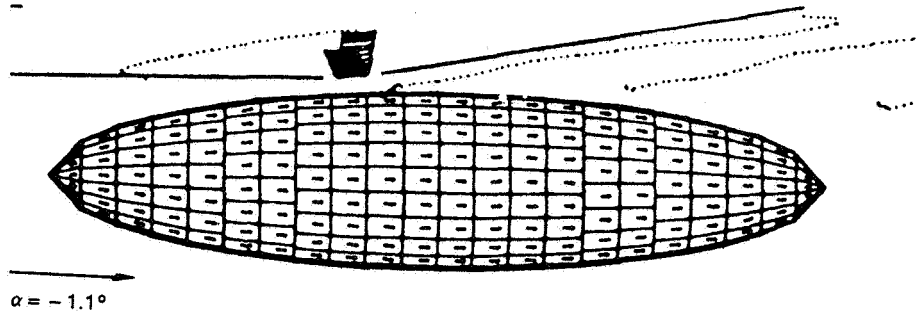

c) $\mu = 0.35$

Figure 39. Side view of fuselage, generalized wake tip filaments, and surface velocity vectors. (concluded)

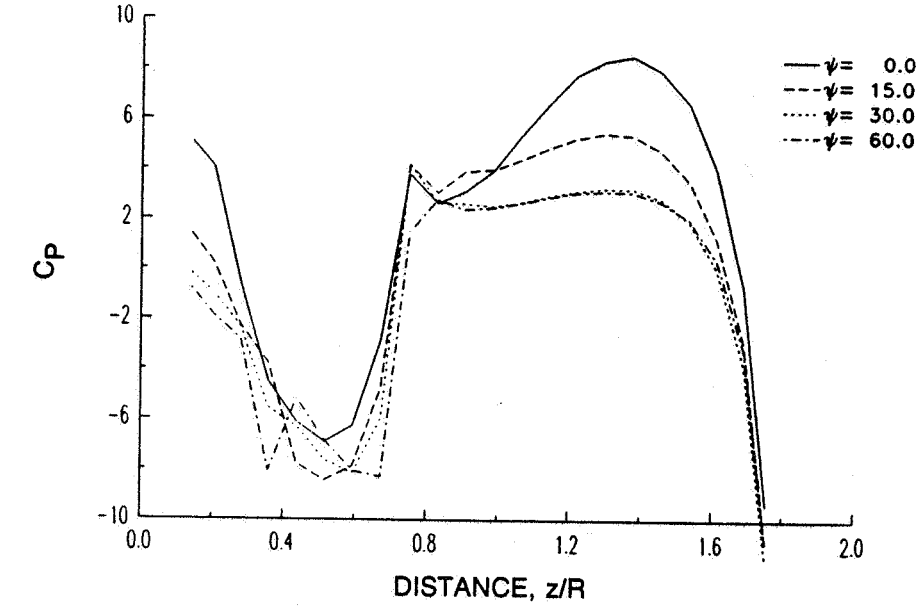

a) $\mu = 0.05$

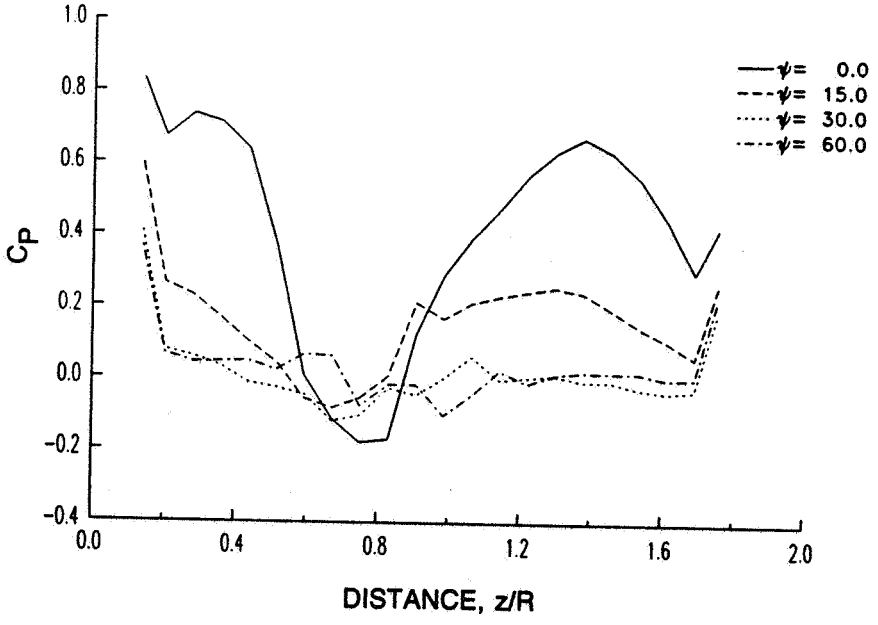

b) $\mu = 0.15$

Figure 40. Pressure along the top of the fuselage, with generalized wake model.

87-11-47-49

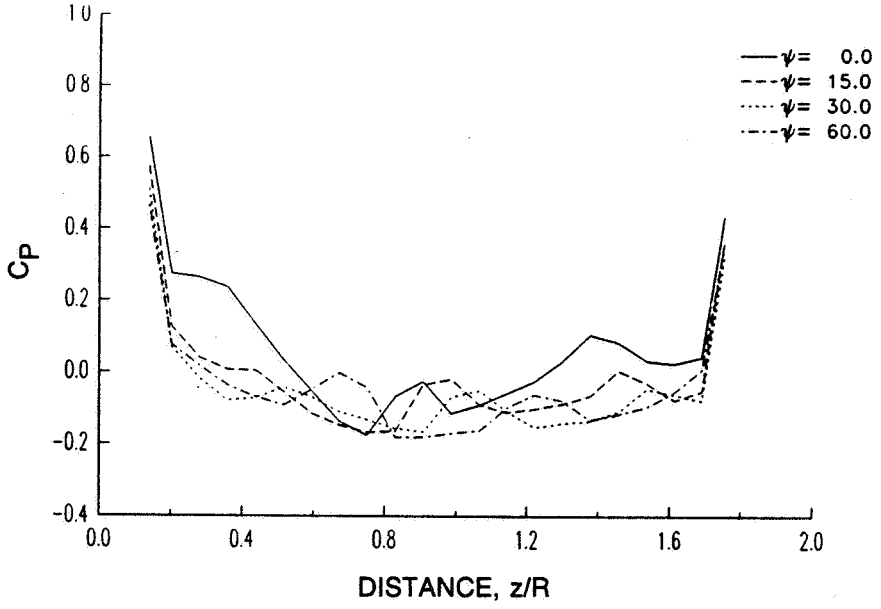

c) $\mu = 0.35$

Figure 40. Pressure along the top of the fuselage, with generalized wake model. (concluded)

87-11-47-50

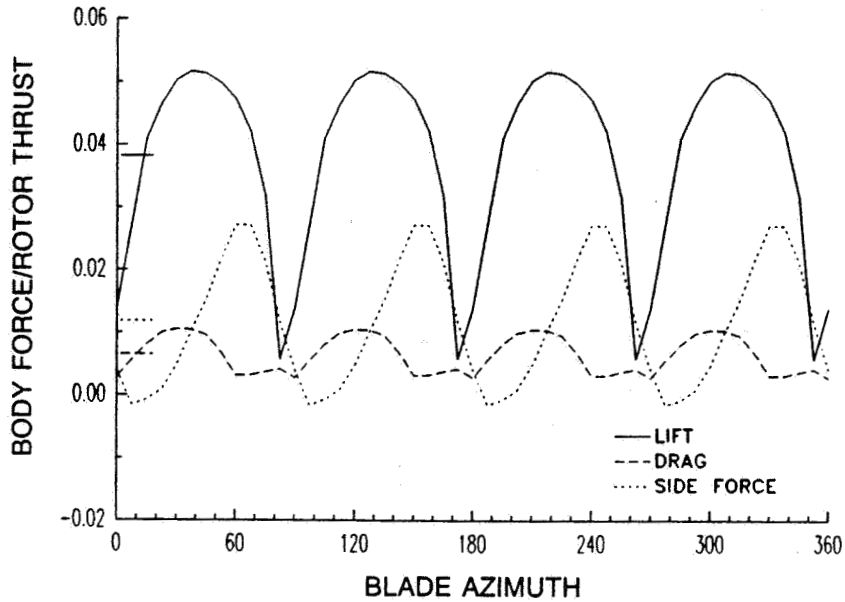

a) $\mu = 0.05$, $C_T = 0.0079$

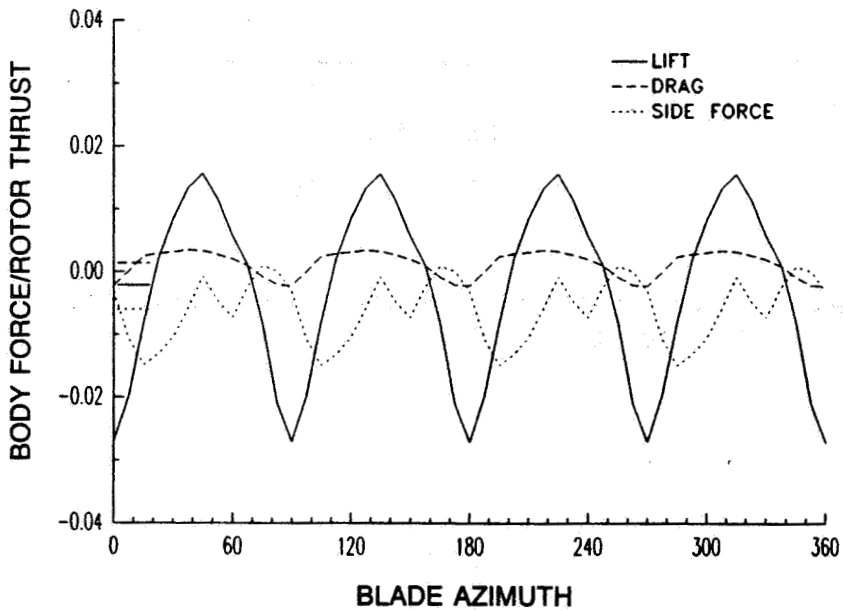

b) $\mu = 0.15$, $C_T = 0.0078$

Figure 41. Fuselage airloads, with generalized wake model.

87-11-47-51

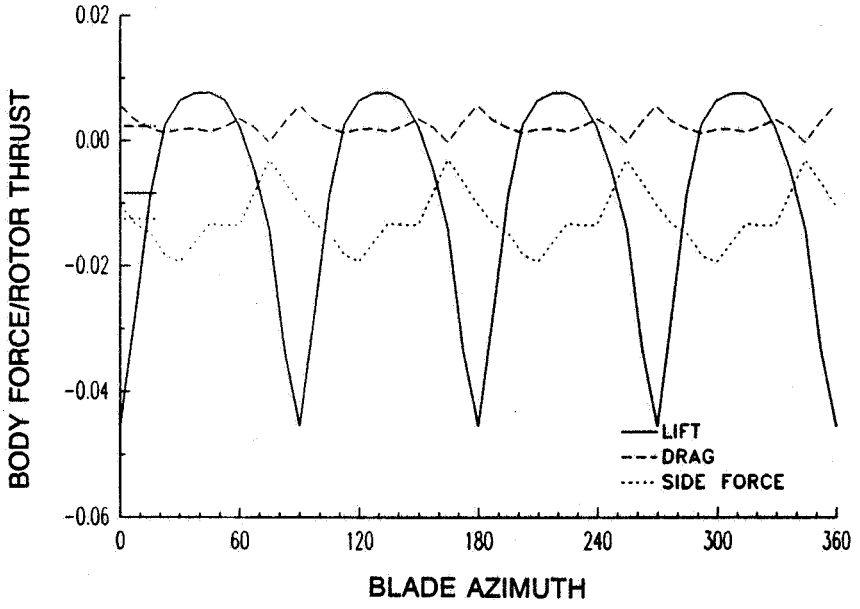

c) $\mu = 0.35$, $C_T = 0.0078$

Figure 41. Fuselage airloads, with generalized wake model. (concluded)

87-11-47-52

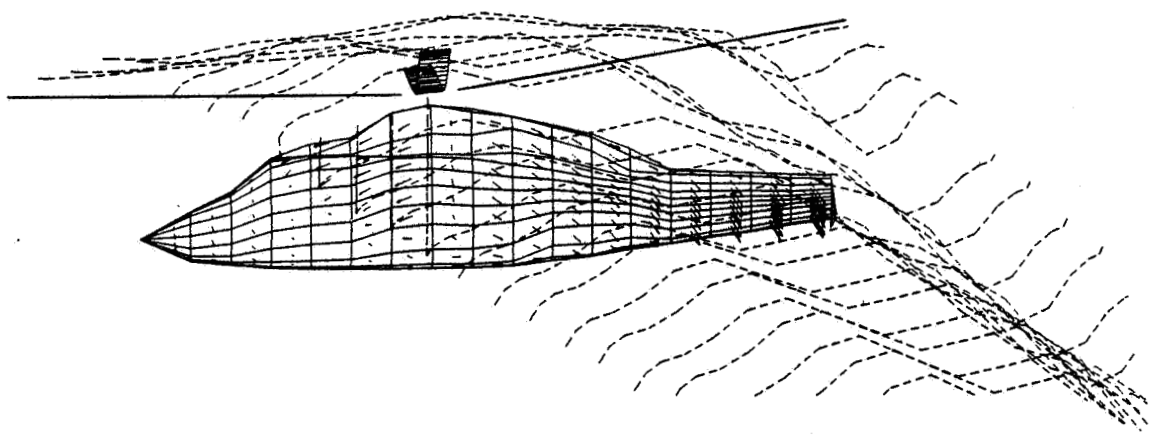

Figure 42. Helicopter fuselage and tip vortices at $\mu = 0.05$.

87-11-47-53

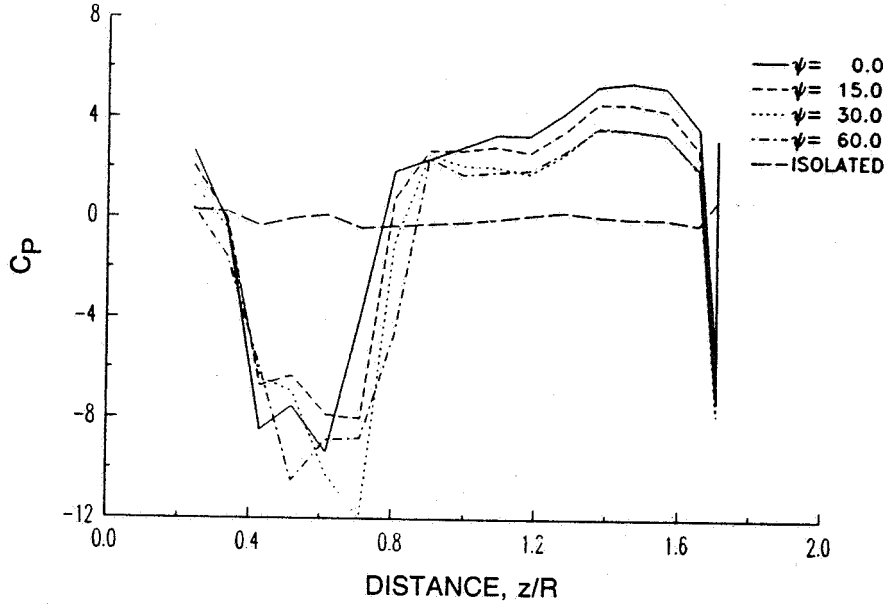

a) $\mu = 0.05$

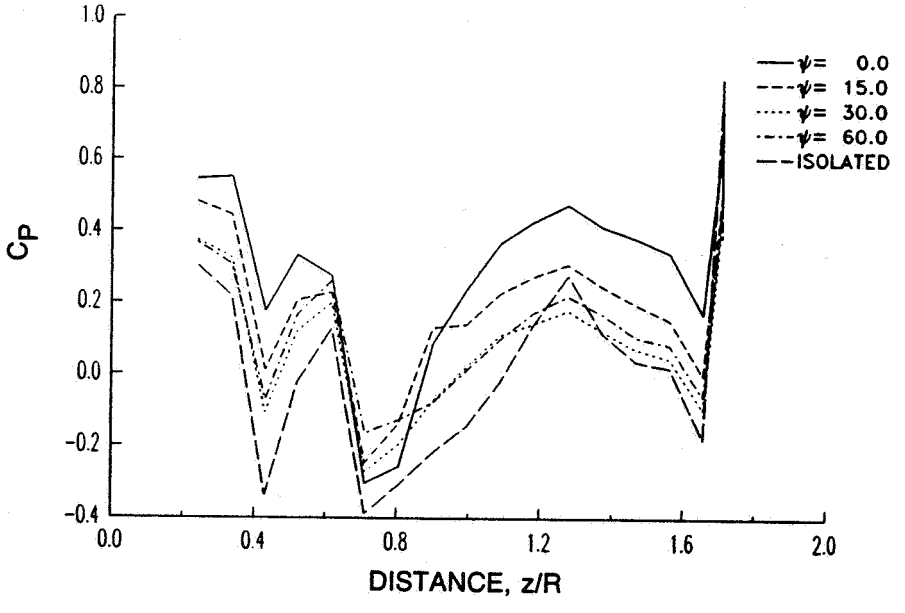

b) $\mu = 0.15$

Figure 43. Pressure along the top of helicopter fuselage, with generalized wake model.

87-11-47-54

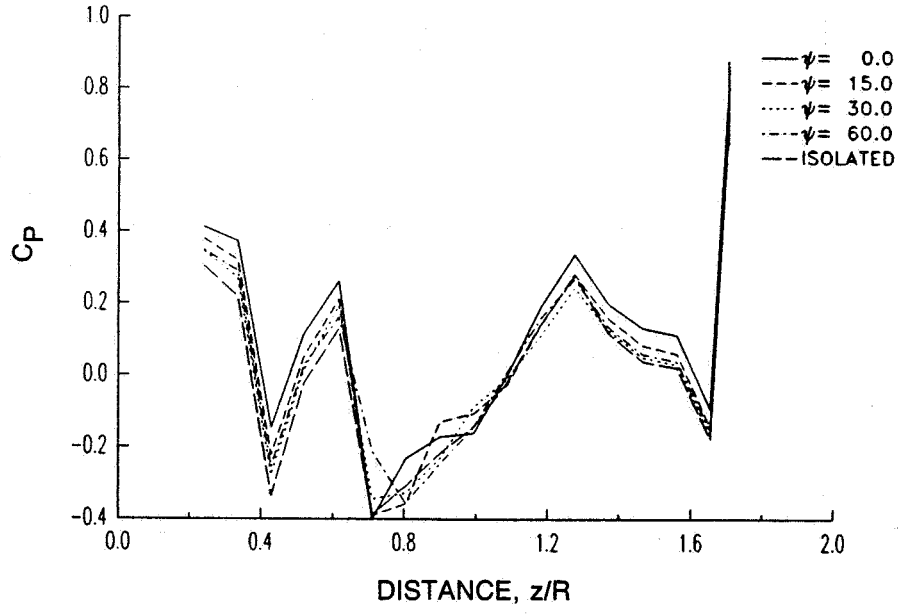

c) $\mu = 0.350$

Figure 43. Pressure along the top of helicopter fuselage, with generalized wake model. (concluded)

C-2

87-11-47-55

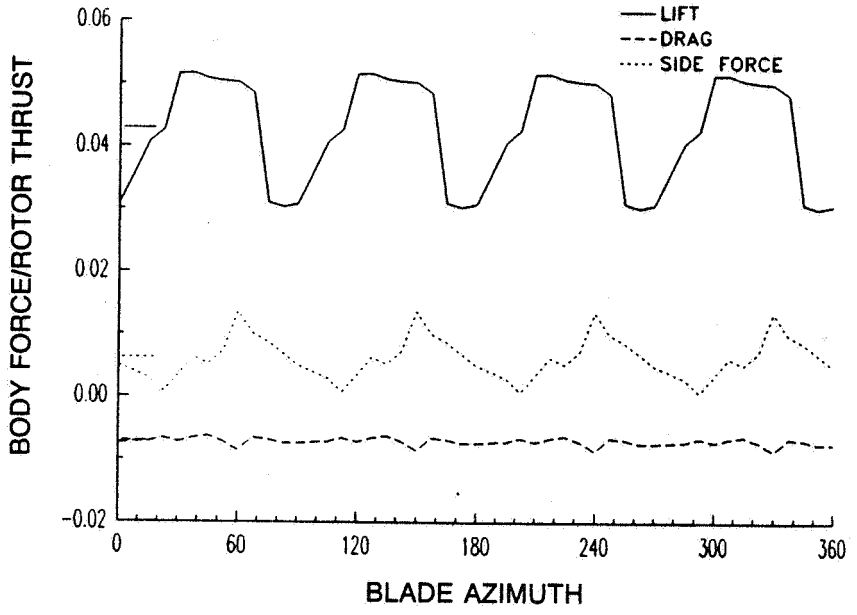

a) $\mu = 0.05$, $C_T = 0.0079$

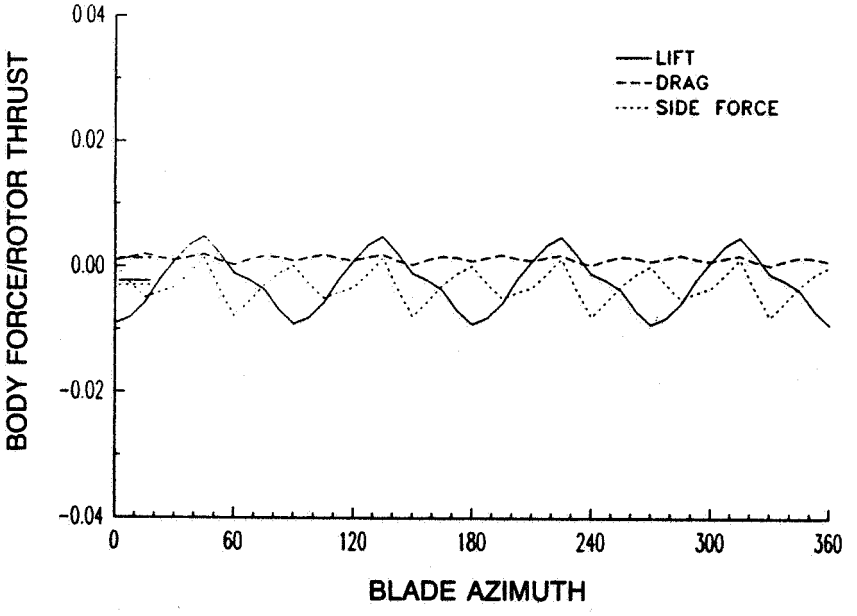

b) $\mu = 0.15$, $C_T = 0.0078$

Figure 44. Airloads on helicopter fuselage, with generalized wake model.

87-11-47-56

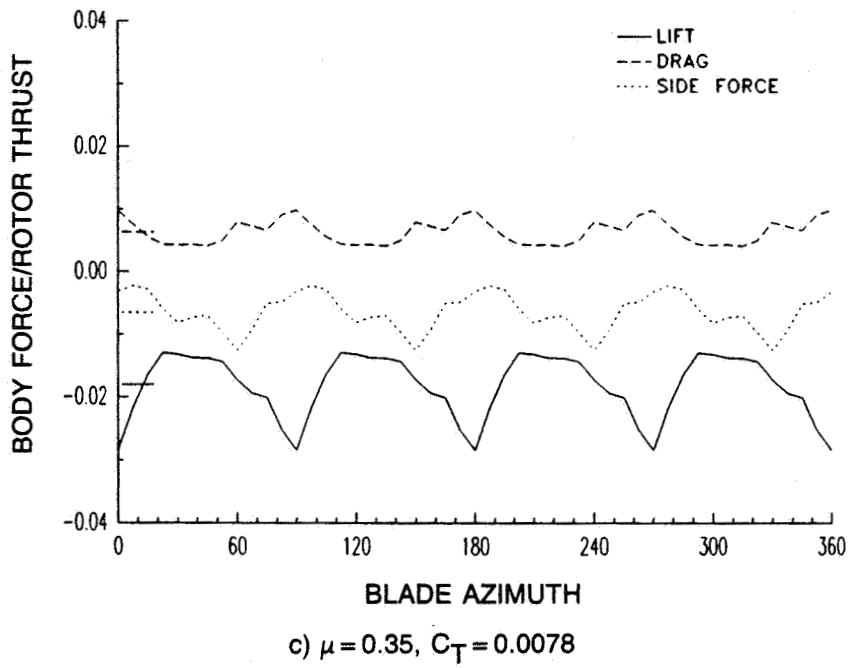

c) $\mu = 0.35$, $C_T = 0.0078$

Figure 44. Airloads on helicopter fuselage, with generalized wake model. (concluded)

87-11-47-57

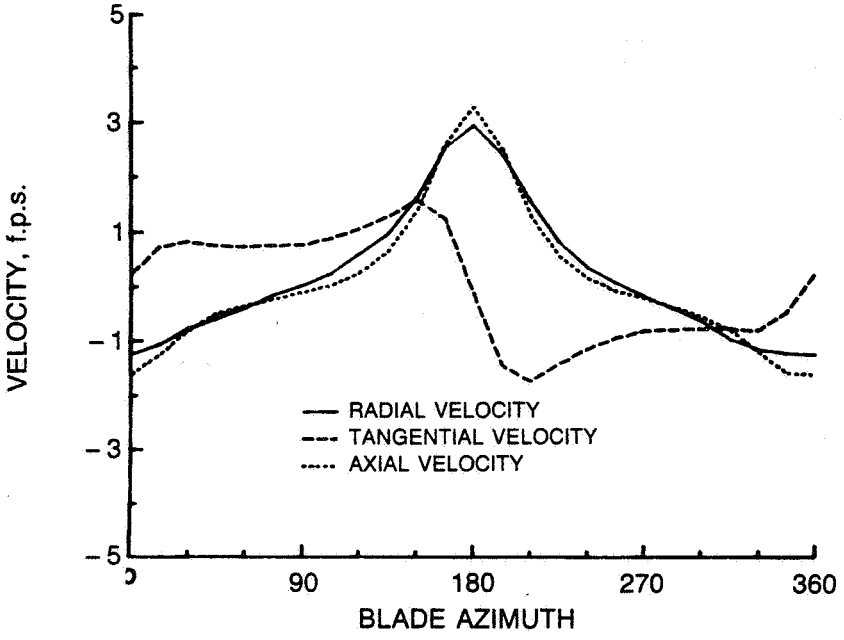

a) HELICOPTER FUSELAGE

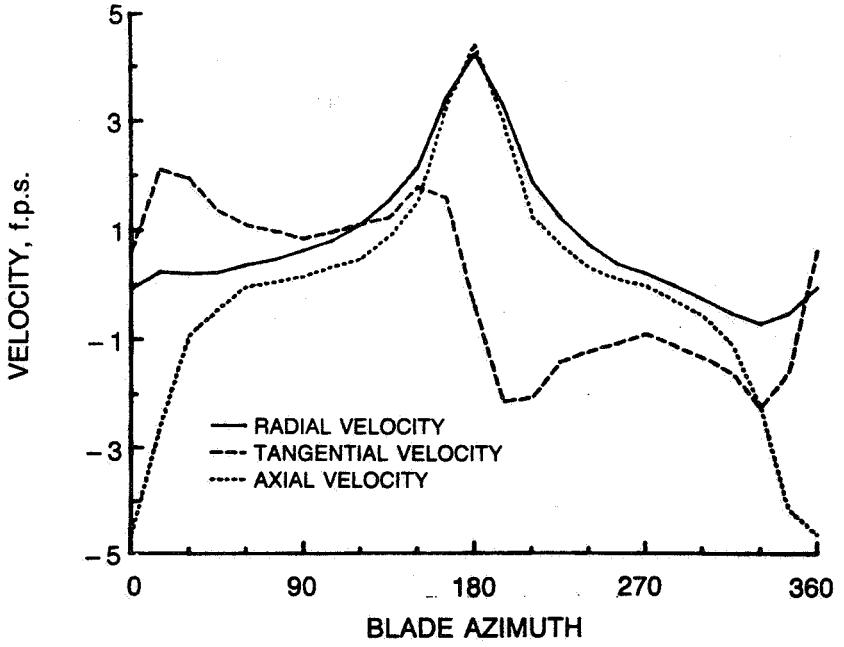

b) ELLIPSOIDAL FUSELAGE

Figure 45. Fuselage-induced velocities at the rotor, $\mu = 0.15$, $C_T = 0.0078$, r/R = 0.75.

87-11-47-58

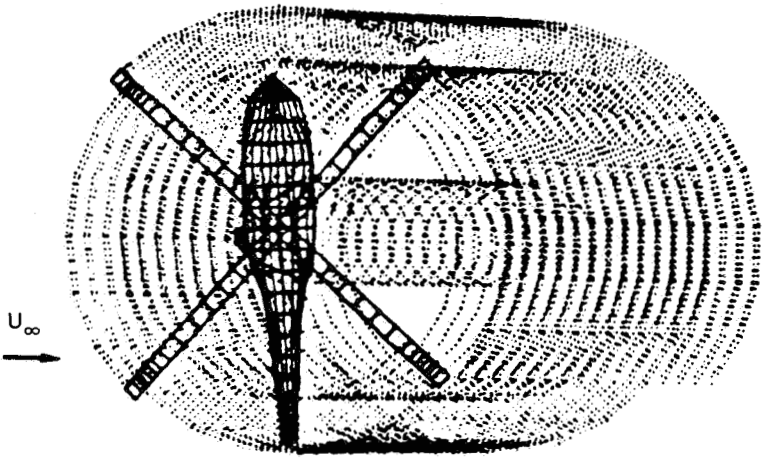

a) TOP VIEW OF AIRCRAFT AND WAKE

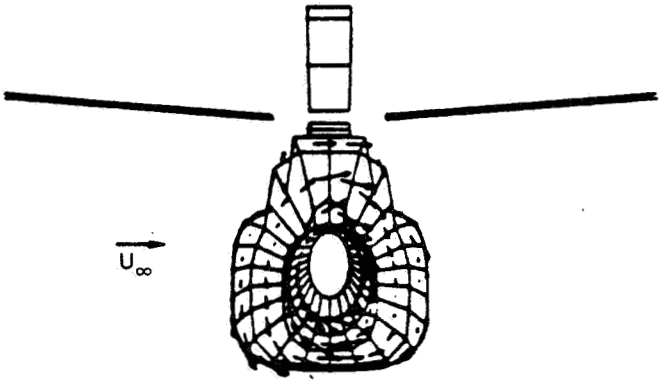

b) REAR VIEW OF AIRCRAFT AND SURFACE VELOCITIES

Figure 46. Computation at 90° yaw.

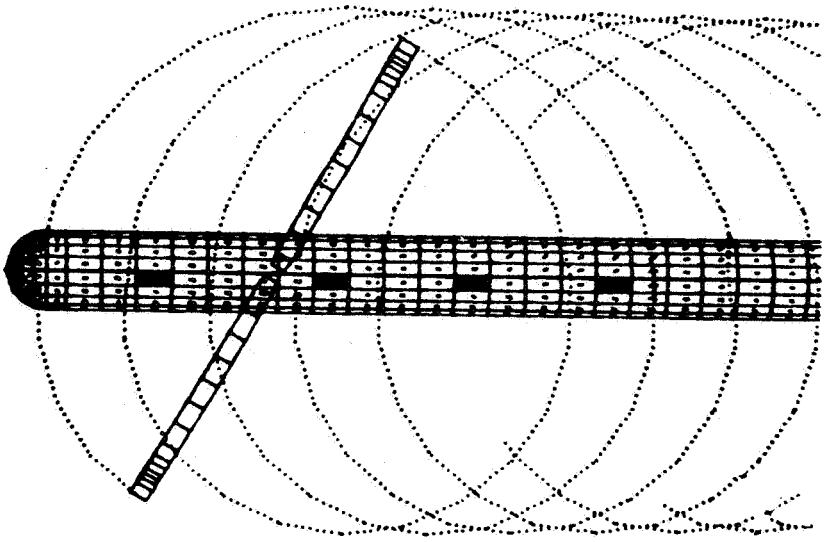

a) TOP VIEW

■ = MICROPHONE POSITIONS

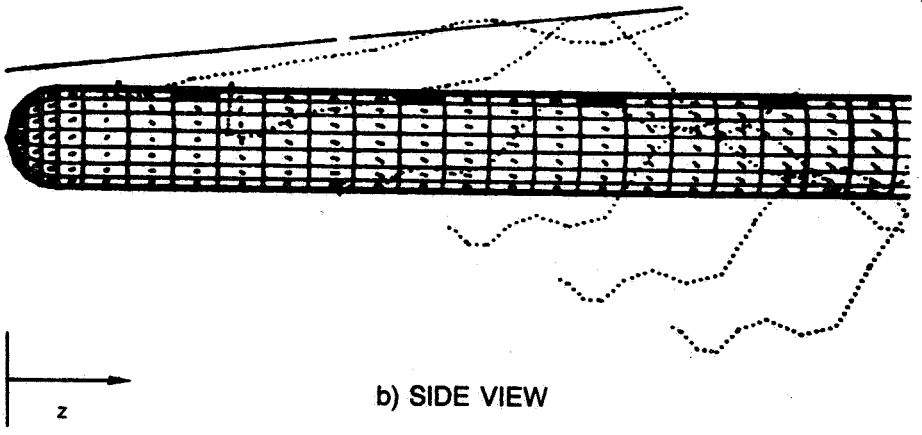

b) SIDE VIEW

Figure 47. Cylinder, rotor, and wake model used to simulate experiment of ref. 25, $\mu = 0.10$.

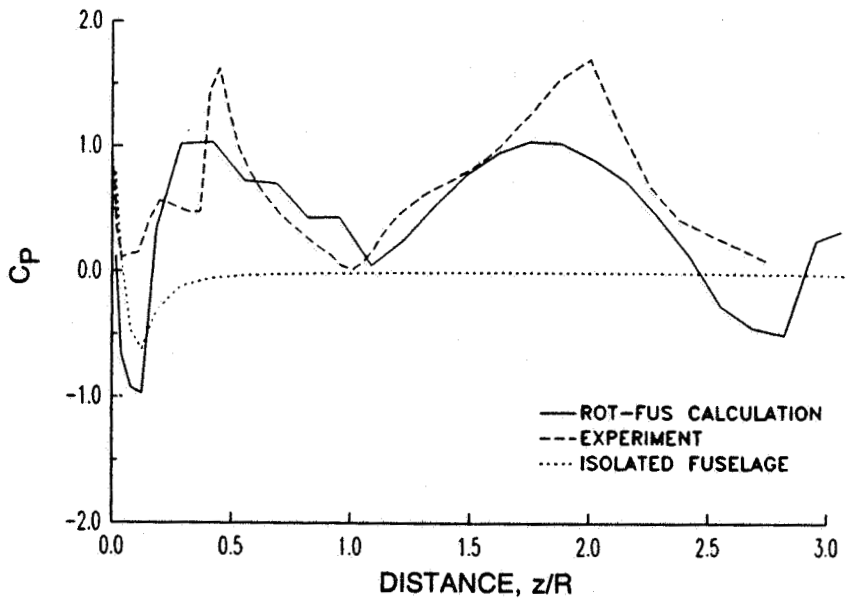

Figure 48. Mean surface pressures along the top of the cylinder, $\mu = 0.10$.

87-11-47-61

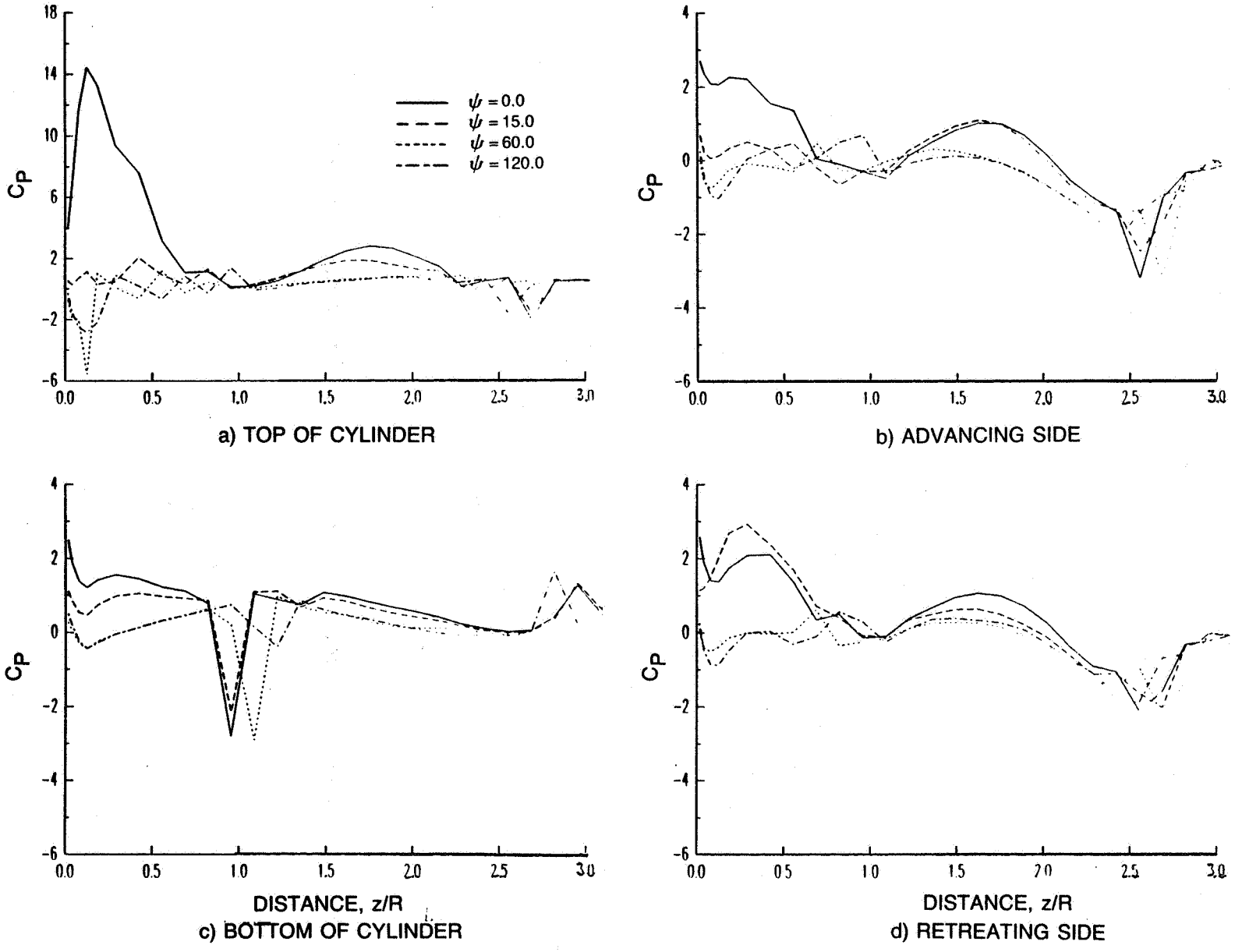

Figure 49. Calculated instanteous surface pressures on the cylinder, $\mu = 0.10$.

87-11-47-64

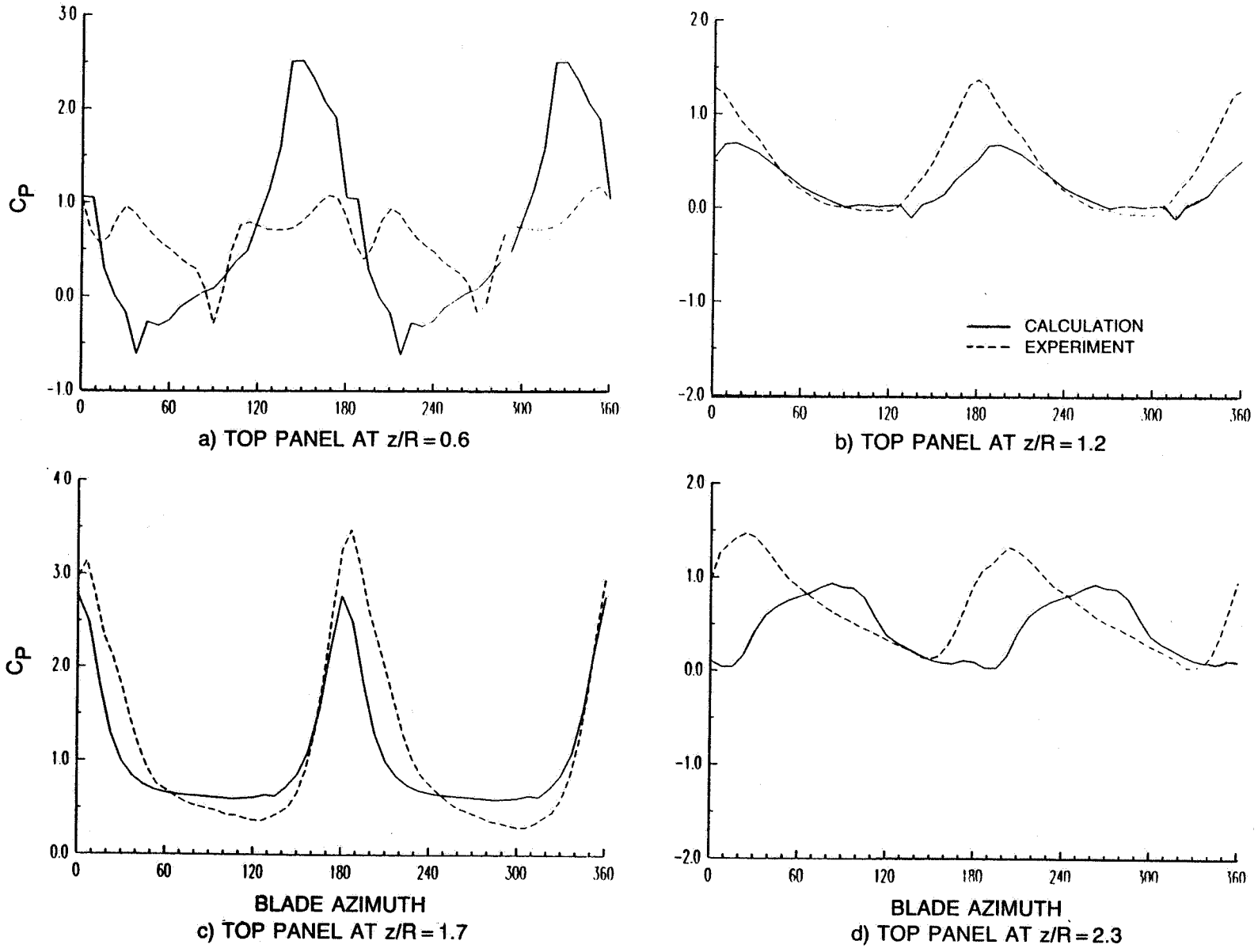

Figure 50. Unsteady surface pressures at four locations on the top of the cylinder, $\mu = 0.10$.

87-11-47-66

APPENDIX A - A COUPLED MAIN/TAIL ROTOR INTERACTION STUDY

List Of Symbols

CL_T	lift coefficient of tail rotor under the influence of the main rotor
CL_{Tiso}	lift coefficient of isolated tail rotor
H	vertical distance above main rotor tip path plane (m)
L	longitudinal distance from the edge of the main rotor disk (m)
R_M	main rotor radius (m)
R_T	tail rotor radius (m)
x,y,z	tip path plane coordinate system of rotor 1 (m)
x_h, y_h, z_h	translation of the hub of rotor 2 relative to the hub of rotor 1 in the tip path plane coordinate system of rotor 1 as used by F389SR (m)
x_T, y_T, z_T	tip path plane coordinate system of rotor 2 (m)
Θ_x	rotation of the tip path plane coordinate system of rotor 2 as used by F389SR about the x-axis of rotor 1 (deg)
Θ_z	rotation of the tip path plane coordinate system of rotor 2 about the z-axis of rotor 1 after it has been rotated about the x-axis of rotor 1 (deg)
ω_1, ω_2	rotational velocities of rotor 1 and rotor 2 respectively (rad/sec)
ϕ_T	azimuthal starting position of rotor 2 in rotor 2's tip path plane coordinate system relative to the zero azimuthal position, positive in the direction of rotation of rotor 2 (deg)
μ	rotor advance ratio; flight speed/tip speed
χ	wake skew angle relative to tip path plane (deg)

Introduction

The rotorcraft operates in an interactional aerodynamic environment which strongly affects the rotorcraft system performance. Major sources of aerodynamic interaction are the main and tail rotors, the fuselage, stores, and the empennage assembly. These interactions are a much more challenging aerodynamic prediction problem than the isolated component predictions (ref. A-1). The main/tail rotor interaction problem is a subset of the complete interaction problem. The ability to predict the effect of the main rotor interactions on the tail rotor performance and the similar effect of the tail rotor on the main rotor performance is critical to the design of advanced rotorcraft systems.

Fortunately, analyses which treat the isolated rotor/tail/fuselage components have been developed to a level of sophistication adequate for the prediction of simple component interactions. An example of first level coupling of these types of codes to address some aspects of the dynamic and aerodynamic problems in terms of rotor/airframe vibrations is described in reference A-2. The coupled analysis (SIMVIB) in this reference consists of several component codes which treat the main rotor wake influence (ref. A-3), the fuselage airframe influence (refs. A-4 and A-5), and the blade dynamics. The rotor wake and fuselage codes have recently been coupled into an unsteady main rotor/fuselage interaction analysis for the prediction of the effects of the main rotor wake on the fuselage body and the unsteady body effect on the main rotor (ref. A-6). As a logical extension of this coupling process, the rotor wake analysis was modified to treat a coupled main/tail rotor interaction problem using the same level of coupling methodology. This treatment is described in the following sections along with preliminary applications to hover and forward flight conditions to demonstrate the predictive capabilities of the method.

Technical Approach

Basic Analysis Descriptions.-The Prescribed Wake Rotor Inflow Analysis, F389SR, (ref. A-3) is a Prandtl lifting-line/wake vortex lattice method which uses a prescribed wake geometry calculated internally in the code or obtained from an external source as input to the analysis. It can be run in two different modes of operation; to calculate the blade and wake circulation and induced velocity at the rotor blades or to calculate the induced velocity at arbitrary field points about the rotor for a specified wake circulation. The analysis assumes steady flight, periodic blade controls and motions, and neglects the shed wake circulation. The effect of the trailing wake circulation is included in the periodic linearized blade circulation solution, along with the ability to input additional sources of inflow at the rotor blades.

This inflow can be obtained from any source, but must be periodic over the rotor disk. Further details of the analysis and its capabilities are available in reference A-3. The application of this analysis to the main/tail rotor interaction problem on a first level basis requires no capabilities to be added to the existing code. The fundamental interaction prediction capability already exists by the appropriate coupling of the two different modes of operation noted above. However, there are some inherent limitations of the application of the analysis to the main/tail rotor problem due to the assumption of a periodic rotor solution and the prescribed wake models available. Specifically, the fact that the rotational speeds of the main and tail rotor are not necessarily integer multiples of each other restricts the solution process. Also the lack of a prescribed main/tail wake interaction model may not provide the correct wake influence under some conditions. As such, the following two assumptions for the interaction process of this study are made:

1) The wake geometries are assumed to be unaffected by their mutual influence.

2) When the rotational speeds of the two rotors are unequal, they are modified for field point calculation purposes to be set to have a ratio equal to the nearest integer multiple.

Because of the large number of input data required to describe the field point coordinates of the blades of a rotor operating within a region of interaction of another rotor, the F389SR analysis was modified to incorporate the feature of internally calculating the field points of another rotor. In the field point mode, the user specifies the hub position relative to the influencing hub, harmonics of flapping motion and flapping hinge, azimuthal phase angle, number of blades, blade radius, inflow stations, and rotor tip speed. From this information, the analysis will internally calculate the positions of the influenced rotor blades relative to the influencing rotor for the field point calculation process. The geometry of a main rotor and tail rotor configuration is shown in figure A-1 which uses the above information to define the relative positions. The analysis was also modified to output the induced velocity, in harmonic form, at these field points at the appropriate time when the blade of the influenced rotor is at the field point location. If the influenced rotor blade is rotating faster than the influencing rotor, then the induced velocities represent an averaging over the integer multiple of the period of the influenced rotor. This process filters out sub-harmonic induced influence. If the influenced rotor blade is rotating slower than the influencing rotor, then the induced velocities represent a time period equal to the integer multiple of the period of the influencing rotor. The output of the resulting induced velocity field is in the form of harmonic coefficients consistent with the input requirements of the original code for the input of external inflows noted above. These features allow the user to minimize the input of data for the main/tail rotor coupling described in the next section.

Coupling Procedure.-The coupling of the main rotor and tail rotor is performed by using the existing features of the code with the modifications noted above to minimize the amount of input data the the user must provide. All coupling is done using externally defined data files and the appropriate system commands (job control language, JCL). The sequence of program execution is described below along with the key data that must be stored as input for subsequent executions for the code. The following abbreviations are used, MR for main rotor, TR for tail rotor, GC for geometric influence coefficients.

1) Calculate Isolated MR Circulation Solution
   Save MR Circulation Solution GC
   Save MR Circulation Solution

2) Calculate Induced Velocity Of MR on TR Field Points
   Read MR Circulation Solution
   Save MR on TR Field Point GC
   Save Harmonics of MR Induced Velocity At TR

3) Calculate Isolated TR Circulation Solution
   Save TR Circulation Solution GC

4) Calculate TR Circulation with MR Influence
   Read Harmonics of MR Induced Velocity At TR
   Read TR Circulation Solution GC
   Save TR Circulation Solution

5) Calculate Induced Velocity Of TR on MR Field Points
   Read TR Circulation Solution
   Save TR on MR Field Point GC
   Save Harmonics of TR Induced Velocity At MR

6) Calculate MR Circulation with TR Influence
   Read Harmonics of TR Induced Velocity At MR
   Read MR Circulation Solution GC
   Save MR Circulation Solution

7) Calculate Induced Velocity Of MR on TR Field Points
   Read MR Circulation Solution
   Read MR on TR Field Point GC
   Save Harmonics of MR Induced Velocity At TR

8) Calculate TR Circulation with MR Influence
   Read Harmonics of MR Induced Velocity At TR
   Read TR Circulation Solution GC
   Save TR Circulation Solution

9) Repeat Steps 5 to 8 until convergence is obtained

This process requires that the user is familiar with the input locations in the F389SR code which turn on (or off) the appropriate options needed to save or use the information calculated during previous steps of the process. References A-3 includes a users manual for the original F389SR code and reference A-7 includes an addendum to reference A-3 for the use of the latest version of F389SR.

Preliminary Application

In order to determine if the coupled main/tail rotor analysis is capable of predicting the mutual interference of the two rotors on each other, some preliminary applications were performed in both hover and forward flight. These initial applications were not intended to validate the methodology, but were performed as a demonstration of the method.

Rotor Geometries.-The rotor geometries were both two bladed, constant chord blade designs. The main rotor blade had a radius of 36.11 feet, a chord of 2.167 feet, and a twist rate of -10.0 degrees with a collective of 10.0 degrees. The tail rotor blade had a radius of 6 feet, a chord of 1.167 feet, and the same twist rate and collective pitch as the main rotor. No blade pitching or flapping motions were used. Thus conclusions drawn from these preliminary applications should be interpreted with some degree of caution in terms of the representation of actual rotorcraft operating geometries.

Interference Measure.-The F389SR analysis does not predict rotor performance, however it does calculate a rotor lift coefficient based on the bound circulation. This calculation was originally intended as an informal check to compare with other prediction codes and does not account for the true orientation of the blade or the inflow angle. This rotor lift coefficient normalized by the isolated rotor lift coefficient was used in this study as the measure of the influence of the interacting rotors.

Hover Application.-The first set of cases run were focused on a single hover condition with using various tail rotor hub positions relative to the main rotor. The tail rotor was positioned at a right angle to the main rotor blade for all but the last case where it was set at 70.0 degrees. The tail rotor hub position was varied in both the vertical and longitudinal position relative to the main rotor. For the initial seven cases, the main and tail rotors were run using a azimuth increments of 15 degrees. The main rotor used nine inflow stations and the tail rotor used four. For the second set of hover conditions (cases 8-11), the tail rotor used nine inflow stations. The rotor inflow stations used are shown in Table A-I. The horizontal and vertical positions are shown graphically in figure A-2 for the hover cases. These positions are listed in Table A-II along with the normalized rotor lift coefficient. These results are displayed graphically in figure A-3 as a function of longitudinal position from the edge of the main rotor disk. The key features to note from these predictions are that the interference decays as the rotors are separated. The use of a finer inflow station distribution changes the normalized values slightly; however, the absolute value of the lift changed by about 15 percent. The canting of the tail rotor had a measurable effect on the interference along with changing the vertical position. These results are not unreasonable. The effect of the main rotor on the tail rotor performance in hover is documented in a recent report (ref.

A-8) and show similar levels of change in terms of performance, although the results reported in that reference also include the effect of the fuselage.

The effect of the tail rotor on the main rotor was found to be insignificant for every hover condition studied. This result is not unexpected because the current model neglects wake distortion and it is believed the the major effect of the tail rotor on the main rotor is caused by the ingestion of the tail rotor wake into the wake of the main rotor, in the vicinity of the main rotor disk.

Forward Flight.-The analysis was also run for four forward flight conditions representing a variation of advance ratio. The tail position was held fixed for these conditions and the results are tabulated in Table A-III. The nine inflow stations noted above were used for both rotors and the same collective pitch was used. The rotor shaft angle was held fixed at 0.0 degrees for all conditions. Again, conclusions drawn from these preliminary applications should be interpreted with some degree of caution in terms of the representation of actual rotorcraft operating geometries and conditions.

The results are shown in graphical form in figure A-4, plotted as a function of rotor advance ratio. The corresponding hover prediction is included. In figure A-5, the main rotor wake boundary is depicted relative to the tail rotor disk. The results indicate that the main rotor wake influence increases the tail rotor lift with increasing advance ratio. It is obvious from figure A-5, that as the advance ratio increases, the tail rotor disk is increasingly immersed in more of the main rotor wake. Again, no significant effect of the tail rotor presence on the main rotor lift was predicted.

Discussion And Recommendations

The use of the Prescribed Wake Rotor Inflow Analysis (F389SR) has been shown to demonstrate that the influence of the main rotor wake on the tail rotor can be predicted. The degree of correlation with test data is uncertain due to the preliminary nature of this study. In hover, the effect of the main rotor on the tail rotor is of the correct level of change, based on some test data which includes fuselage influence. It was also determined that the predicted influence of the tail rotor on the main rotor lift using the current coupled analysis is insignificant and that this is believed to be due to the assumption of non-interacting wake geometries.

The results of this preliminary study indicate that the method has the potential to predict the main/tail rotor interaction and that the wake modeling must be improved for the accurate tail rotor effect on the main rotor in hover. Two courses of action are recommended; (1) the coupled main/tail rotor analysis be applied to rotor designs for which main/tail rotor inter-

action data exists without the presence of a fuselage for correlation purposes and to determine the sensitivity of the method to the number of inflow stations and the wake azimuth (time step) increment and (2), develop main/tail rotor wake interaction models, either (or both) based on experimentally obtained geometries or by prediction methods such as free wake methods.

References

A-1. Sheridan, P.F., and R.P. Smith, Interactional Aerodynamics - A New Challenge to Helicopter Technology, Journal Of the American Helicopter Society, Volume 25, No. 1 January 1980.

A-2. Sopher, R., R.E. Studwell, S. Cassarino, and S.B.R. Kottapalli,Coupled Rotor/Airframe Vibration Analysis, NASA CR-3582, Nov. 1982.

A-3. Egolf, T. A., and A. J. Landgrebe, A Prescribed Wake Rotor Inflow and Flow Field Prediction Analysis - User's Manual and Technical Approach, NASA CR-165894, June 1982.

A-4. Sheehy, T. W., A Simplified Approach to Generalized Helicopter Configuration Modeling and the Predictions of Fuselage Surface Pressures. Paper presented at the National Symposium on Helicopter Aerodynamic Efficiency, American Helicopter Society - Northeast Region, March 1975.

A-5. Sheehy T. W., A Method For Predicting Helicopter Hub Drag., USAAMRDL-TR-75-45, 1975.

A-6. Egolf, T. A., and P.F. Lorber, An Unsteady Rotor/Fuselage Interaction Method, Proceedings of the National Specialists' Meeting on Aerodynamics and Aeroacoustics, Arlington Texas, Feb. 25-27, 1987.

A-7. Lorber, P. F.: Program User's Manual for an Unsteady Helicopter Rotor-Fuselage Aerodynamic Analysis. NASA CR-181701, 1988.

A-8. Balch ,D. T., Experimental Study Of Main Rotor/Tail Rotor/Airframe Interaction In Hover, Presented at the 39th Annual Forum of the American Helicopter Society, St. Louis, Missouri, May, 1983.

Table A-I - Rotor Inflow Stations

Station Number	Main Rotor	Tail Rotor	
1	.329	.350	.329
2	.410	.600	.410
3	.525	.800	.525
4	.650	.900	.650
5	.750		.750
6	.850		.850
7	.925		.925
8	.965		.965
9	.990		.990

Table A-II - Tail Rotor Results in Hover

Case Number	Vertical Position (ft)	Longitudinal Position (ft)	Vertical Tail Angle (deg)	Normalized Lift Coef.
1	0.0	42.2	90.0	.907
2	0.0	42.5	90.0	.911
3	0.0	44.5	90.0	.927
4	0.0	46.5	90.0	.939
5	0.0	48.5	90.0	.948
6	-6.0	42.2	90.0	.933
7	+6.0	42.2	90.0	.923
8	+6.0	42.2	90.0	.928
9	0.0	42.2	90.0	.913
10	0.0	48.5	90.0	.952
11	0.0	42.2	70.0	.921

Table A-III - Tail Rotor Results in Forward Flight

Case Number	Advance Ratio	Vertical Position (ft)	Longitudinal Position (ft)	Vertical Tail Angle (deg)	Wake Skew Angle (deg)	Normalized Lift Coef.
12	0.06	0.0	48.5	90.0	43.5	1.000
13	0.12	0.0	48.5	90.0	25.4	1.049
14	0.24	0.0	48.5	90.0	13.4	1.049
15	0.36	0.0	48.5	90.0	9.0	1.059

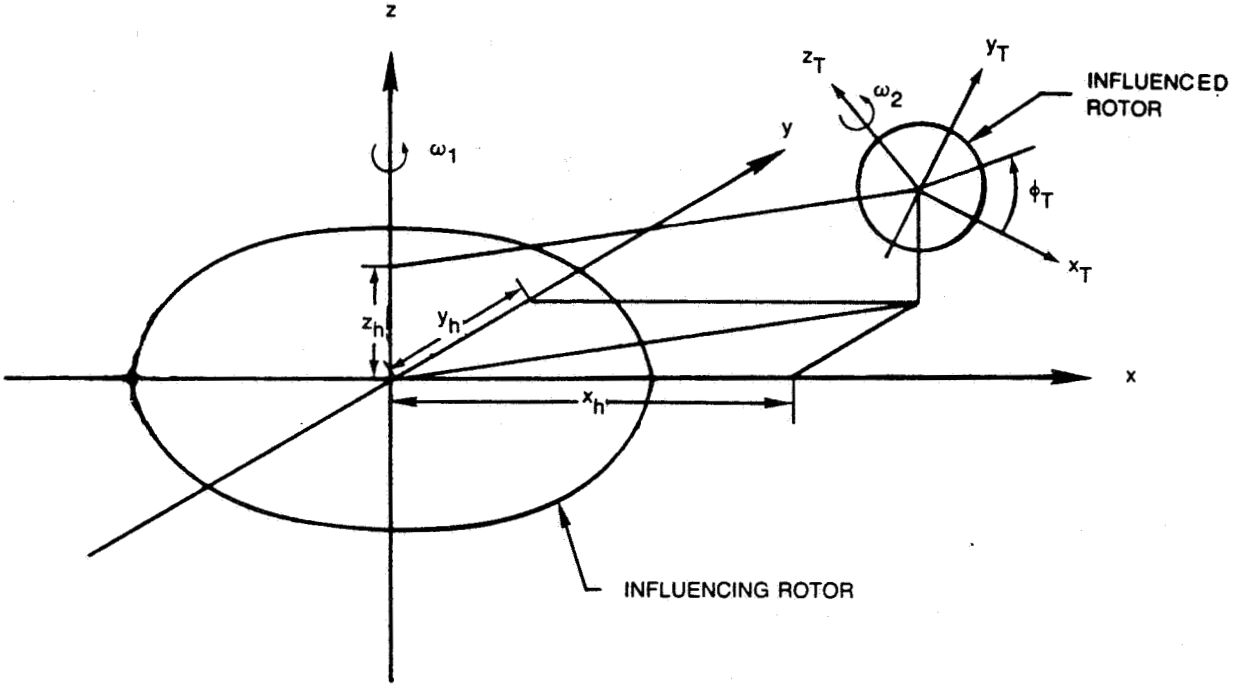

θ_x ROTATION OF x_T ABOUT x AXIS

θ_z ROTATION OF $x_T(\theta_x)$ ABOUT z AXIS

x_h TRANSLATION OF x_T (θ_x, θ_z) IN x

Figure A-1. Relative Geometry of Main Rotor-Tail Rotor Configuration

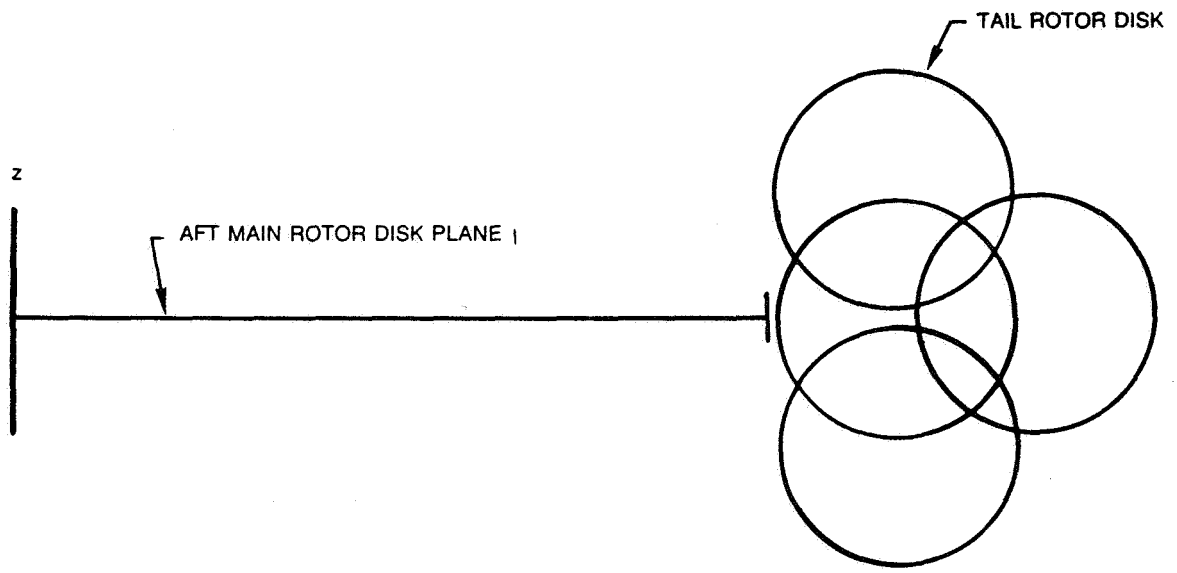

Figure A-2. Relative Position of Tail Rotor Disk to Main Rotor Disk

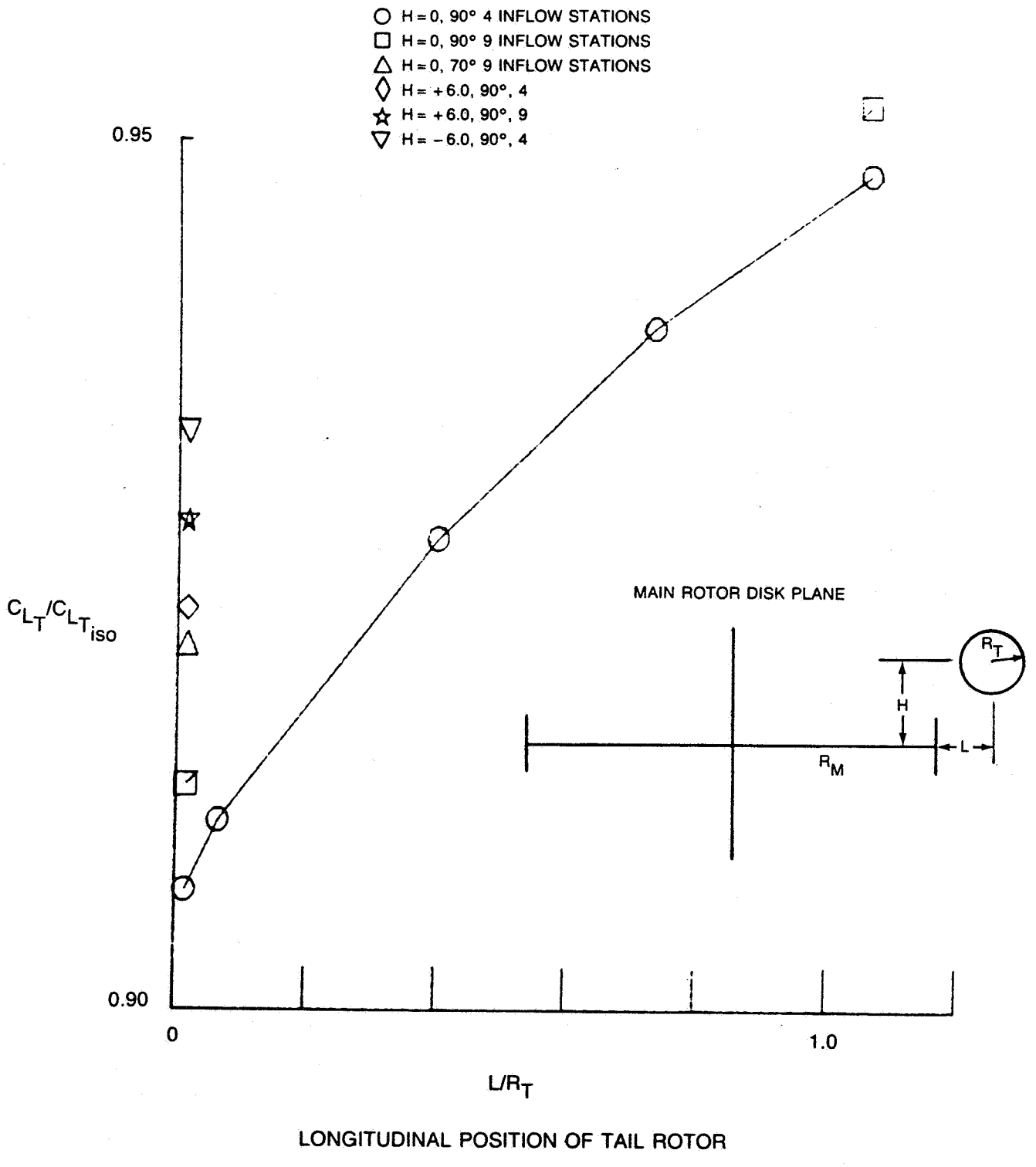

Figure A-3. Effect of Main Rotor on Tail Rotor Lift In Hover

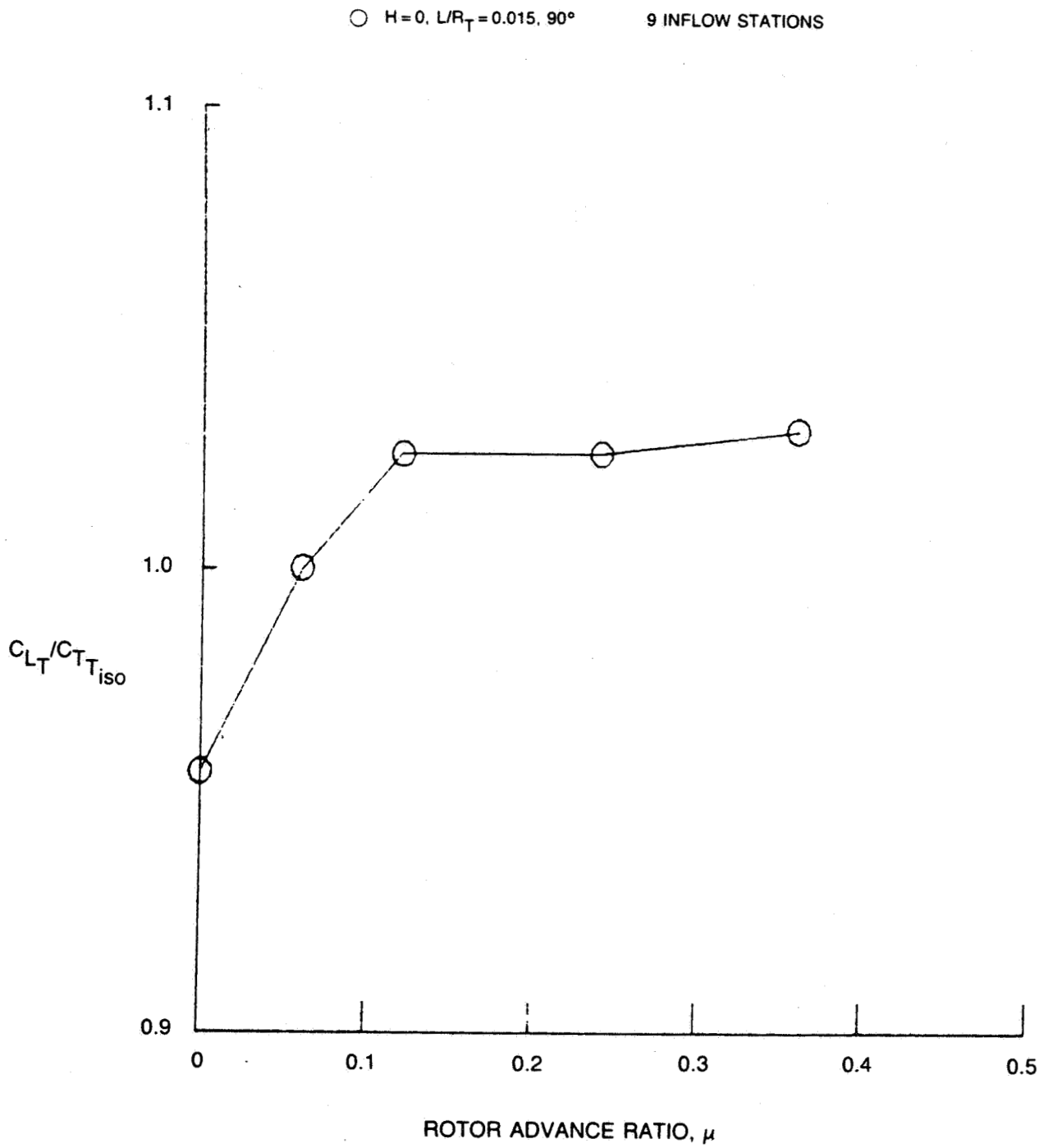

Figure A-4. Effect of Main Rotor on Tail Rotor Lifting in Forward Flight

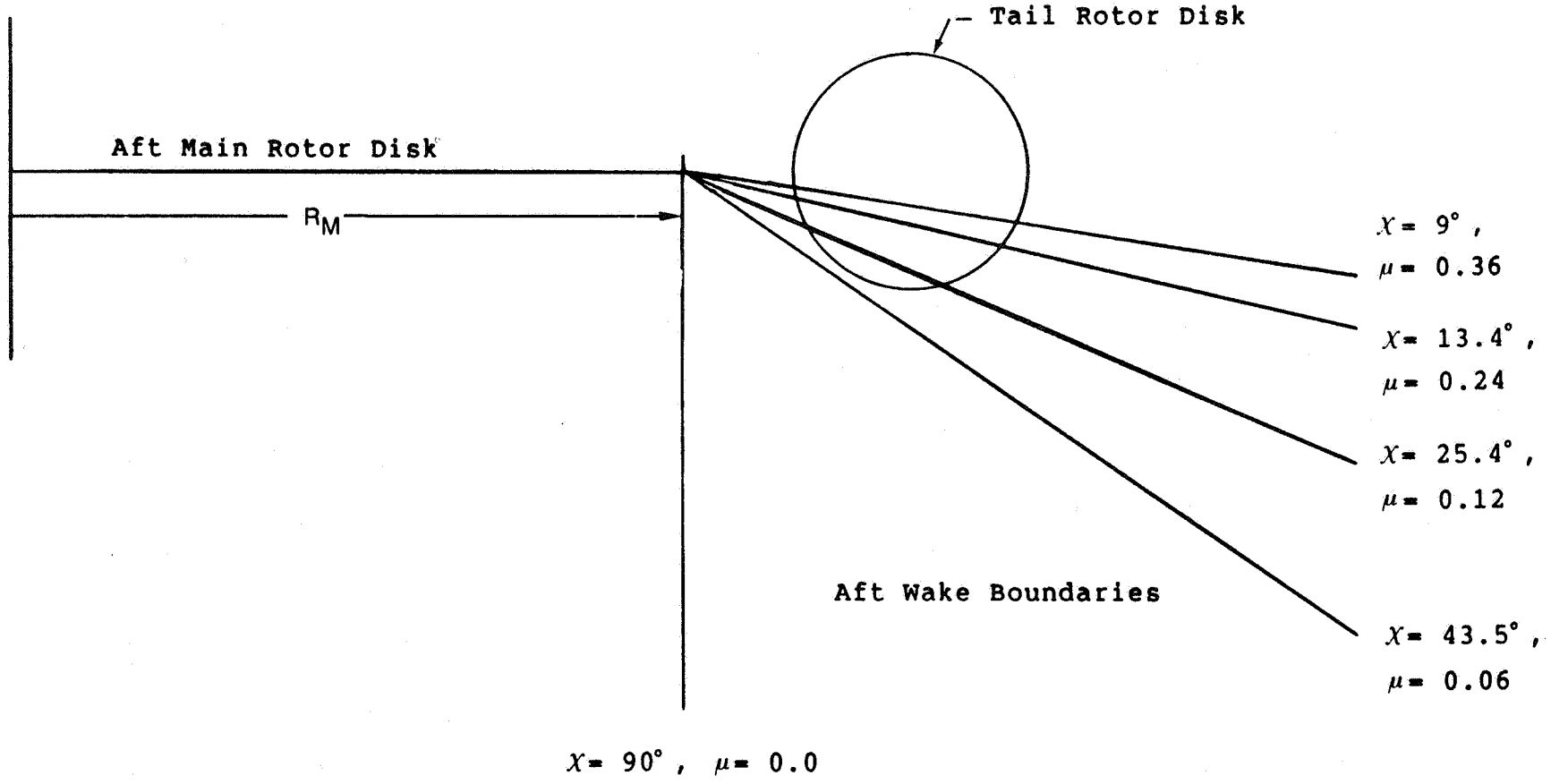

Figure A-5. Tail Rotor Disk-Main Rotor Wake Boundary

APPENDIX B

TWO-DIMENSIONAL MODELLING OF VORTEX-INDUCED UNSTEADY PRESSURES

This appendix will present several analytical model problems that illustrate various aspects of the unsteady interaction between a vortex and a surface, in order to demonstrate the importance of various terms that are present in the calculation of rotor-fuselage interactions. Two-dimensional, incompressible potential flow aerodynamics are used for the analysis.

Fundamentals

The first series of problems are concerned with a constant strength vortex that moves parallel to a flat plate, as shown in this sketch:

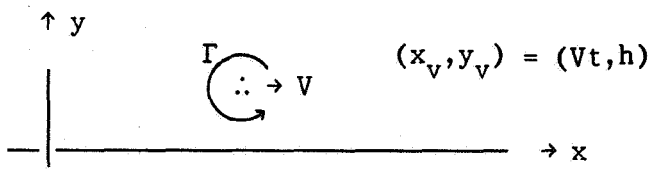

The velocity potential associated with the vortex is given by:

$$\phi(x,y) = \frac{\Gamma}{2\pi} \tan^{-1}\left(\frac{y-y_v}{x-x_v} \right)$$

The cartesian velocity components are:

$$v_x = \frac{\partial \phi}{\partial x} = \frac{\Gamma}{2\pi} \frac{-(y-h)}{(x-Vt)^2 + (y-h)^2}$$

$$v_y = \frac{\partial \phi}{\partial y} = \frac{\Gamma}{2\pi} \frac{(x-Vt)}{(x-Vt)^2 + (y-h)^2}$$

The time derivative of the potential is:

$$\frac{\partial \phi}{\partial t} = \frac{\Gamma}{2\pi} \frac{V\,(y-h)}{(x-Vt)^2 + (y-h)^2}$$

The unsteady Bernoulli equation for the pressure coefficient is:

$$C_p(x,y,t) = \frac{P - P_\infty}{0.5\rho U_\infty^2} = 1 - \frac{U^2}{U_\infty^2} - \frac{2}{U_\infty^2} \frac{\partial \phi}{\partial t}$$

Wake - Fuselage Interaction

A simple model for a helicopter wake tip vortex that is convected past a section of a fuselage includes a vortex, a flat plate, and an image vortex to satisfy the surface boundary condition:

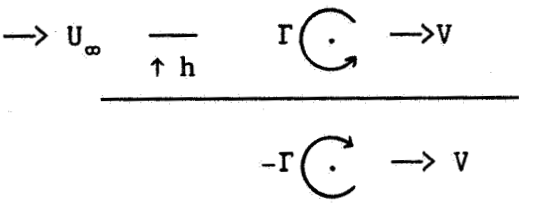

The combined velocity potential is therefore:

$$\phi(x,y,t) = U_\infty x + \frac{\Gamma}{2\pi}\tan^{-1}\left(\frac{y-h}{x-Vt}\right) - \frac{\Gamma}{2\pi}\tan^{-1}\left(\frac{y+h}{x-Vt}\right)$$

At the surface (y=0) the pressure coefficient is:

$$C_p(x,0,t) = 1 - \frac{1}{U_\infty^2}\left(U_\infty + \frac{\Gamma}{2\pi}\frac{2}{(x-Vt)^2+h^2}\right)^2 - \frac{2}{U_\infty^2}\left(-\frac{\Gamma}{2\pi}\frac{2hV}{(x-Vt)^2+h^2}\right)$$

The peak pressure (at x=Vt) is:

$$C_P{}^{peak} = \frac{2\Gamma}{\pi U_\infty h}\left(\frac{V}{U_\infty} - 1\right) - \left(\frac{\Gamma}{\pi U_\infty h}\right)^2$$

For the tip vortex - fuselage interactions used in this report, typical values of the constants are:

U_∞ = 100 ft/sec (μ=0.15)
Γ = 400 ft^2/sec
h = 1 ft
V = U_∞

Using these values the peak C_p is about -4.2 if the effect of the $\partial\phi/\partial t$ term is ignored, and about -1.6 if all terms are included. This implies that the $\partial\phi/\partial t$ term is quite important, and that it acts to reduce the intensity of the wake-fuselage interaction.

Blade - Fuselage Interaction

The blade-fuselage interaction may be modelled in a similar fashion, with the freestream velocity vector now perpendicular to the vortex motion velocity vector (in the sketch, the freestream points up out of the page). The velocity potential is therefore:

$$\phi(x,y,z,t) = U_\infty z + \frac{\Gamma}{2\pi}\tan^{-1}\left(\frac{y-h}{x-Vt}\right) - \frac{\Gamma}{2\pi}\tan^{-1}\left(\frac{y+h}{x-Vt}\right)$$

The surface pressure coefficient is:

$$C_p(x,0,t) = 1 - \frac{1}{U_\infty^2}\left[U_\infty^2 + \left(\frac{\Gamma}{2\pi}\right)^2\left(\frac{2h}{(x-Vt)^2+h^2}\right)^2\right] - \frac{2}{U_\infty^2}\left(-\frac{\Gamma}{2\pi}\frac{2hV}{(x-Vt)^2+h^2}\right)$$

The peak value (at x=Vt) is:

$$C_p^{peak} = -\left(\frac{\Gamma}{\pi U_\infty h}\right)^2 + \frac{2\Gamma}{\pi U_\infty h}\frac{V}{U_\infty}$$

If V is set equal to a typical tip speed (700 ft/sec), and with the other parameters defined as above, the steady terms contribute a C_p of -1.6, while the $\partial\phi/\partial t$ term contributes a C_p of +17.8. While three-dimensional effects are likely to reduce these values, this model problem has clearly demonstrated both the importance of the $\partial\phi/\partial t$ term in calculating close blade-fuselage interactions, and the dominance of the blade-fuselage interaction, when the geometry is such that the blade tip passes close to the surface.

Time-Dependent Vortex Strength

Since the bound circulation of the rotor blade varies with azimuth, the effect of this variation on the $\partial\phi/\partial t$ must be examined. The velocity potential associated with the vortex may be expressed as:

$$\phi(x,y,t) = \frac{\Gamma(t)}{2\pi}\tan^{-1}\left(\frac{y-h}{x-Vt}\right)$$

$$\frac{\partial\phi}{\partial t} = \frac{\Gamma}{2\pi}\left(\frac{V\,(y-h)}{(x-Vt)^2 + (y-h)^2}\right) + \frac{1}{2\pi}\frac{d\Gamma}{dt}\tan^{-1}\left(\frac{y-h}{x-Vt}\right)$$

For the typical helicopter case at $\mu = 0.15$, as defined above, $d\Gamma/dt$ is approximately 1300 ft^2/sec/sec at the position of maximum interaction near the

fuselage nose (ψ=0), so that the increment that would be added to the surface pressure coefficient is:

$$\Delta C_p(x=Vt,y=0) = -\frac{1}{\pi U_\infty^2}\frac{d\Gamma}{dt}\tan^{-1}\left(\frac{-h}{x-Vt}\right)$$

$$\Delta C_p(x=Vt,y=0) \approx -\frac{1}{\pi(115\ ft/sec)^2}(1300\ ft^2/sec^2)(\pi/2)$$

$$\approx 0.05$$

The contribution of this term is obviously much smaller that the contributions of the constant vortex strength $\partial\phi/\partial t$ term or the steady-state term. Therefore it is neglected in the current analysis.

Time - Dependent Source Strength

The final example will study the remaining contribution to $\partial\phi/\partial t$ for the rotor-fuselage interaction: the unsteady variation in the strength of the source panels that represent the fuselage. (The source strength must be time-variant to maintain the flow tangency condition on the surface, given the unsteady velocities induced by the rotor and wake). The model used in this Appendix will be a simple point source. In a uniform flow, a point source represents a semi-infinite half-body:

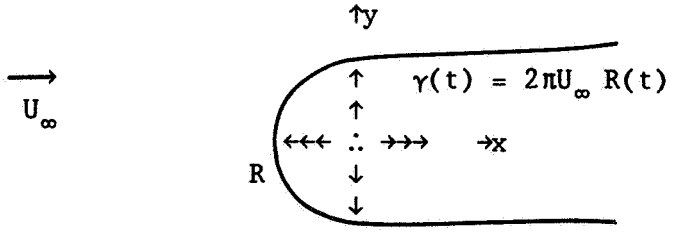

The velocity potential is:

$$\phi(x,y,t) = U_\infty x + \frac{U_\infty R(t)}{2}\ln(x^2 + y^2)$$

The velocity components and the time derivative are:

$$V_x = \frac{\partial \phi}{\partial x} = U_\infty + \frac{R(t)U_\infty x}{x^2 + y^2}$$

$$V_y = \frac{\partial \phi}{\partial y} = \frac{R(t)U_\infty y}{x^2 + y^2}$$

$$\frac{\partial \phi}{\partial t} = \frac{dR}{dt}\,\frac{U_\infty}{2}\,\ln (x^2 + y^2)$$

The surface velocity is:

$$V_x^2 + V_y^2 = U_\infty^2 + U_\infty^2\, R\, \frac{2x + R}{x^2 + y^2}$$

The surface pressure coefficient evaluated directly above the source point is:

$$C_p(0,\pi R/2) = 1 - (1 + (2/\pi)^2) - \frac{dR}{dt}\,\frac{2}{U_\infty}\,\ln (\pi R/2)$$

For the ellipsoid used in this report, a typical value of R is 4 ft, and with a maximum change in source strength of 5% over a rotor half-period of 0.125 sec, the pressure coefficient becomes:

$$C_p(0,\pi R/2) \simeq 1 - (1.4) - (.2\text{ft}/.125\text{sec})\ 2/(115\text{ft/sec})\ \ln(6.3)$$

$$\simeq - (0.4) - (0.05)$$

For this example the contribution of $\partial\phi/\partial t$ is relatively small in comparison with the steady source contribution, and quite small in comparison with the steady and unsteady pressures induced by the wake and rotor. Therefore the neglect of the unsteady source tyerms in the current analysis appears reasonable.

NASA National Aeronautics and Space Administration

Report Documentation Page

1. Report No.	2. Government Accession No.	3. Recipient's Catalog No.
NASA CR-4178		

4. Title and Subtitle
An Unsteady Helicopter Rotor-Fuselage Interaction Analysis

5. Report Date
September 1988

6. Performing Organization Code

7. Author(s)
Peter F. Lorber and T. Alan Egolf

8. Performing Organization Report No.
R88-956977-15

10. Work Unit No.
505-61-51

9. Performing Organization Name and Address
United Technologies Research Center
400 Main St
East Hartford, CT 06108

11. Contract or Grant No.
NAS1-17469

13. Type of Report and Period Covered
Contractor Report

12. Sponsoring Agency Name and Address
National Aeronautics and Space Administration
Langley Research Center
Hampton, VA 23665-5225

14. Sponsoring Agency Code

15. Supplementary Notes
Langley Technical Monitor: John C. Wilson
Final Report

16. Abstract

A computational method has been developed to treat unsteady aerodynamic interactions between a helicopter rotor, wake, and fuselage and between the main and tail rotors. An existing lifting line-prescribed wake rotor analysis and a source panel fuselage analysis were coupled and modified to predict unsteady fuselage surface pressures and airloads. A prescribed displacement technique is used to position the rotor wake about the fuselage. Either a rigid blade or an aeroelastic blade analysis may be used to establish rotor operating conditions. Sensitivity studies were performed to determine the influence of the wake and fuselage geometry on the computation. Results are presented that describe the induced velocities, pressures, and airloads on the fuselage and on the rotor. The ability to treat arbitrary geometries is demonstrated using a simulated helicopter fuselage. Initial computations were made to simulate an experimental study performed at the Georgia Institute of Technology. The computational results are compared with fuselage surface pressure measurements at several locations. No experimental data was available to validate the primary product of the analysis: the vibratory airloads on the entire fuselage. A main rotor-tail rotor interaction analysis is also described, along with some preliminary hover and forward flight results.

17. Key Words (Suggested by Author(s))	18. Distribution Statement
Helicopter Aerodynamics Unsteady Flow Interactional Aerodynamics Computational Aerodynamics	Unclassified - Unlimited Subject Category 01

19. Security Classif. (of this report)	20. Security Classif. (of this page)	21. No. of pages	22. Price
Unclassified	Unclassified	128	A07

NASA-Langley, 1988
For sale by the National Technical Information Service, Springfield, Virginia 22161-2171